Rosenthal, Y., Holbourn, A.E., Kulhanek, D.K., and the Expedition 363 Scientists
Proceedings of the International Ocean Discovery Program Volume 363
publications.iodp.org

https://doi.org/10.14379/iodp.proc.363.101.2018

Expedition 363 summary[1]

Y. Rosenthal, A.E. Holbourn, D.K. Kulhanek, I.W. Aiello, T.L. Babila, G. Bayon, L. Beaufort, S.C. Bova, J.-H. Chun, H. Dang, A.J. Drury, T. Dunkley Jones, P.P.B. Eichler, A.G.S. Fernando, K. Gibson, R.G. Hatfield, D.L. Johnson, Y. Kumagai, T. Li, B.K. Linsley, N. Meinicke, G.S. Mountain, B.N. Opdyke, P.N. Pearson, C.R. Poole, A.C. Ravelo, T. Sagawa, A. Schmitt, J.B. Wurtzel, J. Xu, M. Yamamoto, and Y.G. Zhang[2]

Keywords: International Ocean Discovery Program, IODP, *JOIDES Resolution*, Expedition 363, Site U1482, Site U1483, Site U1484, Site U1485, Site U1486, Site U1487, Site U1488, Site U1489, Site U1490, Western Pacific Warm Pool, Indo-Pacific Warm Pool, Intertropical Convergence Zone, Indonesian Throughflow, Timor Sea, Australian monsoon, equatorial Pacific, eastern Indian Ocean, Northwest Australian margin, Papua New Guinea, Sepik River, Manus Basin, Eauripik Rise, Neogene, Miocene, Pliocene, Pleistocene, millennial-scale climate variability, orbital-scale climate variability, carbonate accumulation, high-resolution interstitial water samples, Antarctic Intermediate Water, North Pacific Intermediate Water, Upper Circumpolar Water, Leeuwin Current, West Australian Current, early diagenesis, soft-sediment deformation, exceptional foraminifer and nannofossil preservation, biosilica, hydroclimate, Admiralty Islands volcanism, Last Glacial Maximum ocean density structure, middle-upper Miocene magnetostratigraphy, stratigraphic intercalibration and cyclostratigraphy

Contents

Abstract

International Ocean Discovery Program Expedition 363 sought to document the regional expression and driving mechanisms of climate variability (e.g., temperature, precipitation, and productivity) in the Indo-Pacific Warm Pool (IPWP) as it relates to the evolution of Neogene climate on millennial, orbital, and geological timescales. To achieve our objectives, we selected sites with a wide geographical distribution and variable oceanographic and depositional settings. Nine sites were cored during Expedition 363, recovering a total of 6956 m of sediment in 875–3421 m water depth with an average recovery of 101.3% during 39.6 days of on-site operations. Two moderate sedimentation rate (~3–10 cm/ky) sites are located off northwestern Australia at the southwestern maximum extent of the IPWP and span the late Miocene to present. Seven of the nine sites are situated at the heart of the Western Pacific Warm Pool (WPWP), including two sites on the northern margin of Papua New Guinea with very high sedimentation rates (>60 cm/ky) spanning the past ~450 ky, two sites in the Manus Basin (north of Papua New Guinea) with moderate sedimentation rates (~4–14 cm/ky) recovering upper Pliocene to present sequences, and three sites with low sedimentation rates (~1–3 cm/ky) on the southern and northern Eauripik Rise spanning the early Miocene to present. The wide spatial distribution of the cores, variable accumulation rates, exceptional biostratigraphic and paleomagnetic age constraints, and mostly excellent or very good foraminifer preservation will allow us to trace the evolution of the IPWP through the Neogene at different temporal resolutions, meeting the primary objectives of Expedition 363. Specifically, the high–sedimentation rate cores off Papua New Guinea will allow us to better constrain mechanisms influencing millennial-scale variability in the WPWP, their links to high-latitude climate variability, and implications for temperature and precipitation in this region under variable mean-state climate conditions. Furthermore, the high accumulation rates offer the opportunity to study climate variability during previous warm periods at a resolution similar to that of existing studies of the Holocene. With excellent recovery, Expedition 363 sites are suitable for detailed paleoceanographic reconstructions at orbital and suborbital resolution from the middle Miocene to Pleistocene and thus will be used to refine the astronomical tuning, biostratigraphy, magnetostratigraphy, and isotope stratigraphy of hitherto poorly constrained intervals within the Neogene timescale (e.g., the late Miocene) and to reconstruct the history of the Asian-Australian monsoon and the Indonesian Throughflow on orbital and tectonic timescales. Results

[1] Rosenthal, Y., Holbourn, A.E., Kulhanek, D.K., Aiello, I.W., Babila, T.L., Bayon, G., Beaufort, L., Bova, S.C., Chun, J.-H., Dang, H., Drury, A.J., Dunkley Jones, T., Eichler, P.P.B., Fernando, A.G.S., Gibson, K., Hatfield, R.G., Johnson, D.L., Kumagai, Y., Li, T., Linsley, B.K., Meinicke, N., Mountain, G.S., Opdyke, B.N., Pearson, P.N., Poole, C.R., Ravelo, A.C., Sagawa, T., Schmitt, A., Wurtzel, J.B., Xu, J., Yamamoto, M., and Zhang, Y.G., 2018. Expedition 363 summary. *In* Rosenthal, Y., Holbourn, A.E., Kulhanek, D.K., and the Expedition 363 Scientists, *Western Pacific Warm Pool*. Proceedings of the International Ocean Discovery Program, 363: College Station, TX (International Ocean Discovery Program). https://doi.org/10.14379/iodp.proc.363.101.2018

[2] **Expedition 363 Scientists' addresses.**

MS 363-101: Published 8 June 2018

from high-resolution interstitial water sampling at selected sites will be used to reconstruct density profiles of the western equatorial Pacific deep water during the Last Glacial Maximum. Additional geochemical analyses of interstitial water samples in this tectonically active region will be used to investigate volcanogenic mineral and carbonate weathering and their possible implications for the evolution of Neogene climate.

Introduction

The Western Pacific Warm Pool (WPWP), often defined by the 28°C isotherm, is the warmest part of the Indo-Pacific Warm Pool (IPWP), which spans the western waters of the equatorial Pacific and eastern Indian Ocean (Figure **F1**). The region is a major source of heat and moisture to the atmosphere and a location of deep atmospheric convection and heavy rainfall. Small perturbations in the sea-surface temperature (SST) of the WPWP influence the location and strength of convection in the rising limbs of the Hadley and Walker cells, affecting planetary-scale atmospheric circulation, atmospheric heating, and tropical hydrology (Neale and Slingo, 2003; Wang and Mehta, 2008). These perturbations may also influence heat uptake and storage in the WPWP thermocline, as well as transport to the Indian Ocean through the Indonesian Throughflow (ITF). These processes also constitute important feedbacks in the climate system due to their influence on the dynamic ocean-atmosphere coupling in the equatorial Pacific, thereby exerting a strong influence on global temperatures and atmospheric pCO_2 (Oppo and Rosenthal, 2010). Detailed paleoceanographic records, such as those recovered during Expedition 363, offer the opportunity to study the behavior of the WPWP under different mean-state background conditions and its effects on both regional and global climate.

Seasonal to interannual climate variations in the WPWP are dominated by fluctuations in precipitation associated with the seasonal march of the monsoons, migration of the Intertropical Convergence Zone (ITCZ), and interannual changes associated with variability of the El Niño Southern Oscillation (ENSO) (e.g., Ropelewski and Halpert, 1987; Halpert and Ropelewski, 1992; Rasmusson and Arkin, 1993) (Figure **F2**). At present, departures from expected weather patterns associated with the monsoon and ENSO systems impact the lives of many people in the tropics and many regions around the world. For example, El Niño events are associated with a nearly global fingerprint of temperature and precipitation anomalies (Ropelewski and Halpert, 1987; Rasmusson and Arkin, 1993; Cane and Clement, 1999). However, considerable uncertainty exists regarding the response of the tropical Pacific climate, primarily precipitation, to rising greenhouse gas concentrations because of our limited understanding of the past variability of the WPWP and conflicting results from data compared to models. For example, models simulating the response of the equatorial Pacific Ocean to greenhouse gas forcing disagree about whether the zonal temperature gradient will increase or decrease and what the implications will be for the Walker circulation and the hydrologic cycle in the tropics (Forster et al., 2007). These simulations typically use an ENSO analogy to predict future climate; in a similar way to interannual ENSO variability, long-term changes in the mean climate state of the equatorial Pacific are often evaluated primarily as changes in the east–west SST gradient. However, other simulations of global warming effects suggest that the tropical Pacific does not become more El Niño- or La Niña-like in response to increased greenhouse gases (DiNezio et al., 2009). Instead, these simulations suggest a different equilibrium state, whereby shoaling and increased tilt of the equatorial Pacific thermocline is associated with weakening of the trade winds without a concomitant change in the zonal SST pattern, which argues against using ENSO as an analog for long-term changes in tropical conditions (DiNezio et al., 2010). In turn, changes in the structure of the thermocline can have a major effect on the ocean heat content, and thus global climate, and also on the character of ENSO variability, which has been documented for the Last Glacial Maximum (LGM) (Ford et al., 2015). Changes in thermocline temperature/structure have also been suggested as a possible mechanism responsible for the slowdown in surface warming from ~2000 to 2014 (e.g., England et al., 2014).

A primary goal of this expedition was to assess the regional expression of climate variability (e.g., precipitation, temperature, pCO_2, and biological productivity) within the WPWP in the context

Figure F1. Mean annual sea-surface temperature within the IPWP with locations of sites cored during Expedition 363 (yellow circles). Black arrows mark the path of the Indonesian Throughflow. Red arrow = Leeuwin Current. Blue arrow = South Equatorial Current. Data source: ODV World Ocean Atlas (**https://odv.awi.de/en/data/ocean/world-ocean-atlas-2013**).

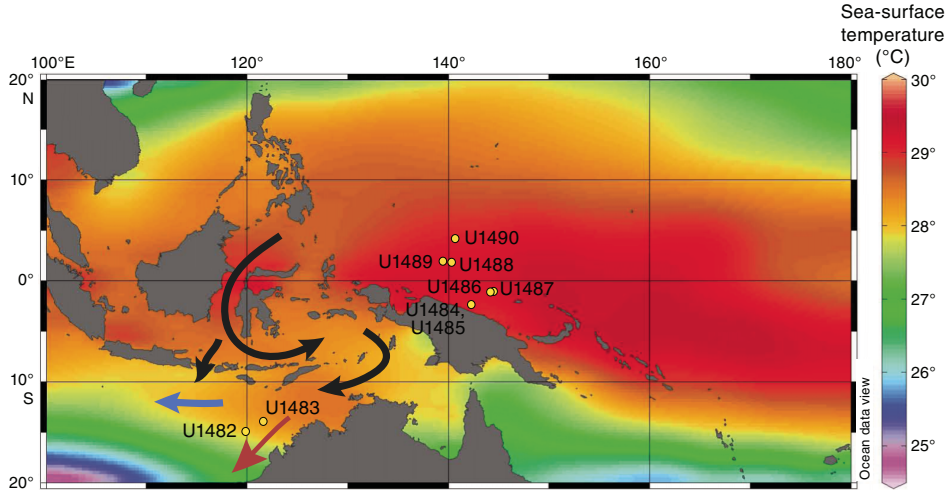

of changes in global background climate state from the middle Miocene to late Pleistocene. Drill sites were chosen to provide broad spatial coverage to capture the most salient features of the WPWP (Figures F1, F3) at different temporal resolutions through this time interval (Figure F4). Situated in variable water depths, sediments at these sites intersect different water masses, including the North Pacific Intermediate Water (NPIW), Antarctic Intermediate Water (AAIW), Upper Circumpolar Deepwater (UCDW), and Lower Circumpolar Deepwater (LCDW) (Figure F5) and thus will allow reconstruction of intermediate and deep-water properties at relatively high resolution through time.

Figure F2. (A) Winter and (B) summer precipitation for 1979–2009 and (C) winter and (D) summer precipitation anomalies during the 1997–1978 El Niño event. DJF = December, January, February; JJA = June, July, August. Data source: IRI Climate Data, Lamont Doherty Earth Observatory, Columbia University (**http://iridl.ldeo.columbia.edu/maproom/Global/Precipitation/index.html**).

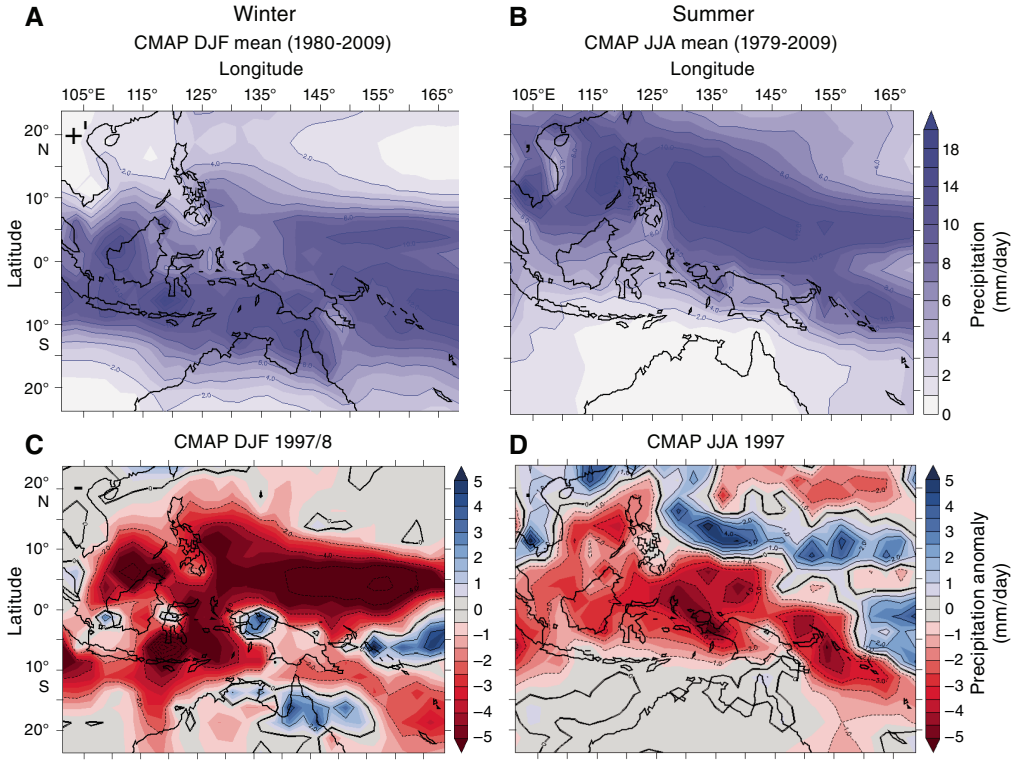

Figure F3. Bathymetric map showing locations of the three main areas cored during Expedition 363: northwest Australian shelf (yellow box), Papua New Guinea/Manus Basin (red box), and the Eauripik Rise (green box). Yellow circles = Expedition 363 sites, purple circles = previously cored DSDP sites, green circles = previously cored ODP sites. Bathymetric data from Amante and Eakins (2009).

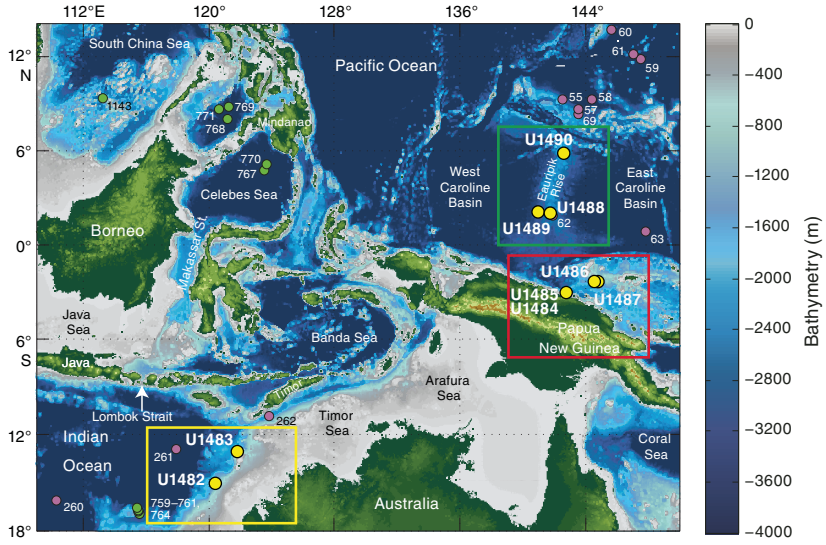

Figure F4. Coring and logging operations summary and temporal resolution of Expedition 363 drill sites.

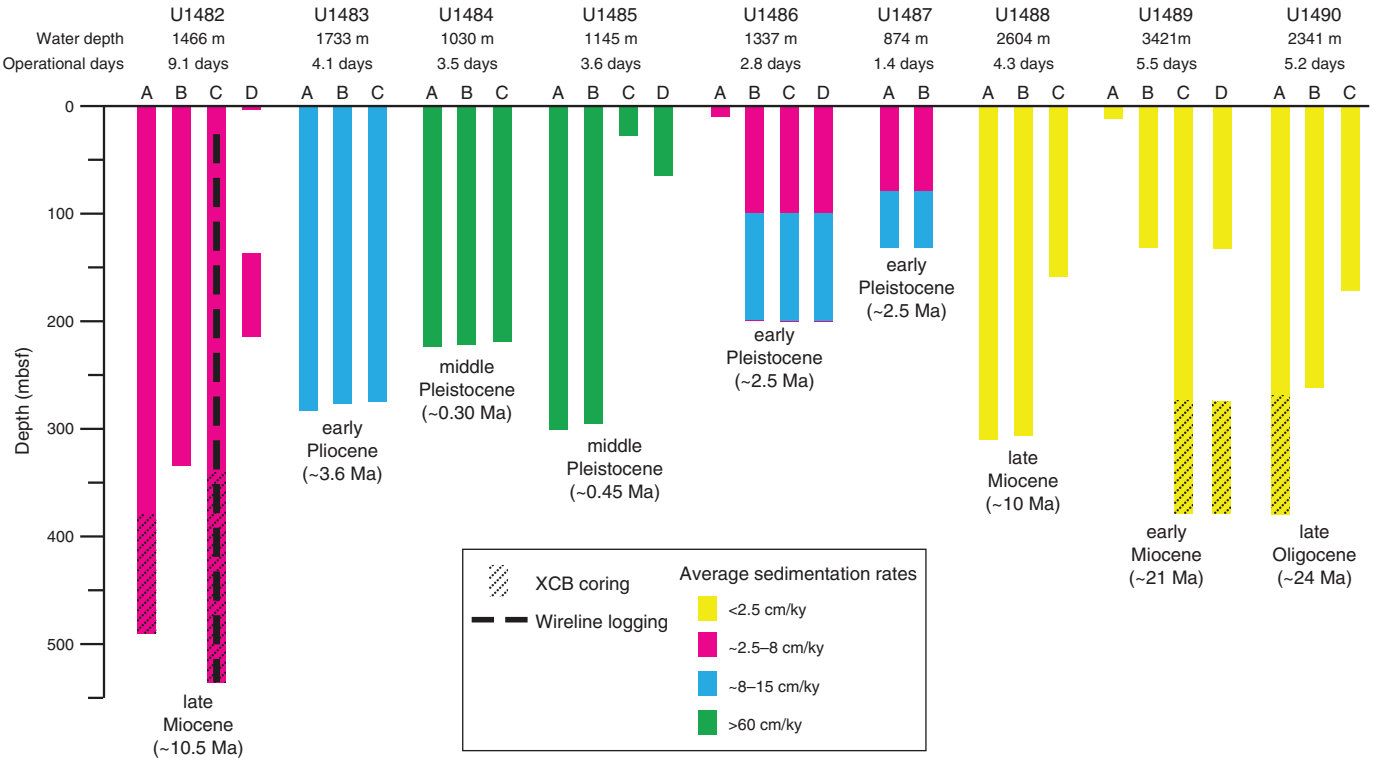

Figure F5. Hydrographic profiles from (A) the southern Eauripik Rise and (B) northeast Papua New Guinea. NPSTW = North Pacific Subtropical Water, SPSTW = South Pacific Subtropical Water, NPIW = North Pacific Intermediate Water, AAIW = Antarctic Intermediate Water, UCDW = Upper Circumpolar Deep Water, LCDW = Lower Circumpolar Deep Water. From Y. Rosenthal (unpubl. data).

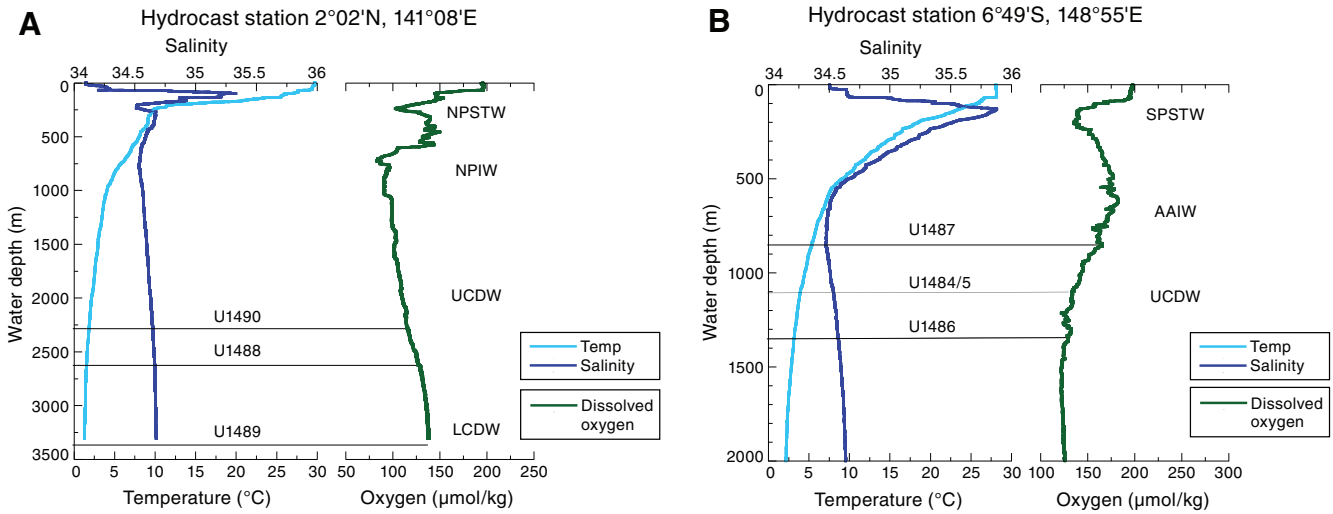

Oceanographic settings

As the warmest ocean water on the planet, the IPWP and in particular the WPWP east of Indonesia, where mean annual SSTs are typically >29°C (Figure F1), are known to influence the dynamics of ENSO and the Asian-Australian monsoon. Throughout the IPWP, warm water fuels atmospheric convection and heavy rainfall, resulting in a net freshwater flux into the ocean of 4–18 mm/day (Figure F2). The biggest seasonal changes in surface hydrography are expressed in salinity, with freshening caused by changes in precipitation due to the seasonal march of the ITCZ and the Asian-Australian monsoon. On interannual timescales, ENSO exerts the strongest influence on regional precipitation and, consequently, surface salinity. The spatial extent of the warm pool changes seasonally as the core of the WPWP follows the ITCZ migration. As a result, the size of the WPWP is smaller (larger) and SST is cooler north (south) of the Equator during boreal winter (summer).

The western equatorial Pacific is also a crossroad for thermocline and intermediate waters that originate in the extratropics of both hemispheres (Fine et al., 1994). Due to a complex network of passages and basins, the Indonesian maritime continent on the western edge of the WPWP exerts the strongest control on the

Figure F6. Climatic impact of the Indonesian Throughflow (ITF). The ITF flows from the WPWP through the Indonesian seaways and exits to the Indian Ocean primarily through the Timor Sea. From there, part of the ITF flows southward. joining the Leeuwin Current and bringing heat and moisture to Western Australia. However, most of the ITF enters the westward flowing South Equatorial Current (SEC) across the Indian Ocean, where it joins the southward-flowing Agulhas Current. With major contribution from ITF water, some of the Agulhas Current flows around the Cape of Africa into the Atlantic Ocean as part of the global thermohaline circulation. At present, the ITF receives water from the North Pacific Ocean and to a lesser extent from the South Pacific Ocean through the New Guinea Coastal Current (NGCC), although the relative contributions of these end-members vary seasonally and interannually. On longer timescales, the contribution likely depends on changes in climate conditions and tectonic adjustments of the Indonesian Gateway (e.g., Cane and Molnar, 2001). NECC = North Equatorial Countercurrent, EC = Equatorial Current. Comparing records from Expedition 363 drill sites at the heart of the WPWP and southwestern edge of the IPWP (marked by yellow circles) will allow us to assess changes in the ITF on different temporal scales. Figure modified from Oppo and Rosenthal (2010).

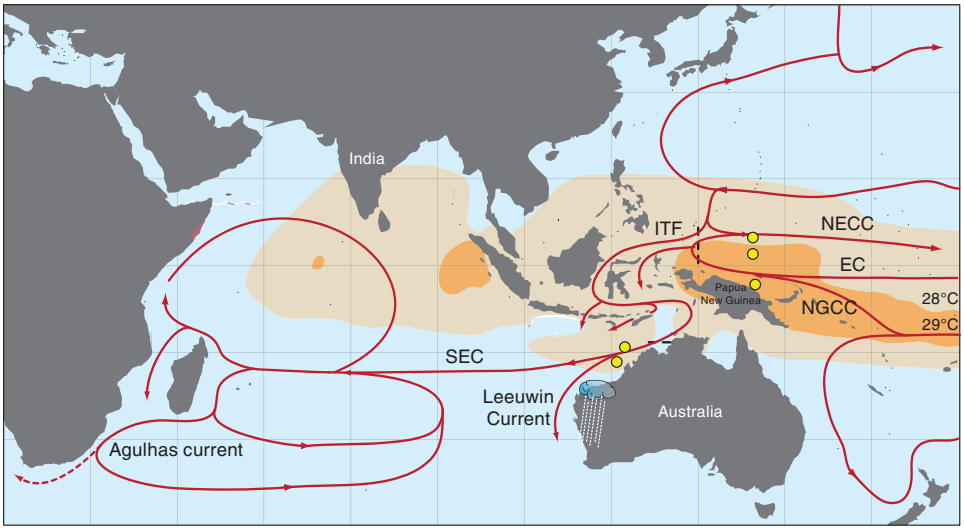

communication between the Pacific and Indian Oceans. As part of the global circulation, the ITF is the only equatorial interocean connection transferring heat and freshwater from the Pacific to the Indian Ocean, thus modifying the heat and salt budget of the Indian Ocean. These changes affect the Atlantic Ocean via the Agulhas Current and thus ultimately may have far-reaching effects on ocean meridional circulation and climate (Figure **F6**). The ITF is driven by the average difference in sea level between the Pacific and Indian Oceans (~16 cm). Most of the ITF transport occurs in the upper 750 m of the water column, with the maximum volume transport occurring between 150 and 400 m (Fieux et al., 1994; Ffield et al., 2000; Gordon et al., 2003; Susanto and Gordon, 2005). On average, the ITF transports a large amount of water (10–15 Sv, where 1 Sv = 1,000,000 m^3/s) and heat (~0.5 PW, where 1 PW = 10^{15} W) from the WPWP north of the Equator to 12°S in the Indian Ocean. Approximately 80% of the total ITF moves through the Makassar Strait (Figure **F3**) (Gordon, 2005). Of this, 25% flows directly south through the Lombok Strait and 75% takes a more circuitous route flowing eastward into the Banda Sea and then westward into the Indian Ocean via the Timor Sea (Fieux et al., 1994; Gordon and Fine, 1996; Gordon and Susanto, 1999) (Figures **F1**, **F3**). In the subsurface of the WPWP, the upper thermocline represents a mixture of North Pacific and South Pacific subtropical waters (NPSTW and SPSTW, respectively). At present, the NPSTW is the largest source to the ITF with a smaller contribution of denser SPSTW through the New Guinea Coastal Current (NGCC), which is the branch of the westward, cross-equatorial flowing Pacific South Equatorial Current (SEC), and constitutes the main southern Pacific contribution to the ITF thermocline (Gordon and Fine, 1996; Hautala et al., 1996; Johnson and McPhaden, 1999). The lower thermocline and deeper (>500 m) receives contributions from the low-salinity, low-oxygen NPIW (salinity 34.45; density 26.5–26.8 σ_θ) advected through the Mindanao Current and the New Guinea Coastal Undercurrent (NGCU), which transport oxygen-rich AAIW (salinity ~34.55; density 27.2–27.3 σ_θ). The deepest sites (>3000 m below sea level [mbsl]) are bathed by LCDW. The relative contributions of these water masses at each of our drilling sites vary depending on their location and age at time of deposition.

Motivation for drilling the IPWP

Studies of climate variability in the IPWP have relied primarily on the low–sedimentation rate (~2–3 cm/ky during the Pleistocene) Ocean Drilling Program (ODP) Hole 806B from the Ontong Java Plateau (Kroenke, Berger, Janecek, et al., 1991), which serves as a warm end-member to monitor broad-scale zonal and meridional gradients through the Neogene. However, higher resolution sites were unavailable from this region, preventing direct comparison with suborbital variability recorded at high-latitude sites. Over the past decade, new coring efforts have demonstrated the possibility of obtaining records from key locations in the WPWP with comparable resolution to records from high-latitude oceans, cave deposits, and ice cores (e.g., Stott et al., 2002; Zuraida et al., 2009). Although substantial progress has been made in understanding IPWP climate variability by studying long piston cores, the newly cored Expedition 363 sites address fundamental questions across a broader spatial distribution and with enhanced temporal resolution. Expedition 363 cored sites of variable accumulation rates from the following three sectors of the IPWP:

1. The southwestern sector of the IPWP (yellow box in Figure **F3**): cores at Sites U1482 and U1483, located seaward of the continental slope of northwest Australia at the southwestern edge of the IPWP and along the exit of the ITF to the Indian Ocean, recovered upper Miocene to recent sediment.

2. The central sector of the WPWP (red box in Figure **F3**): high–accumulation rate Sites U1484 and U1485 on the northern margin of Papua New Guinea close to the Sepik/Ramu River mouths and Sites U1486 and U1487 in the Manus Basin span the late Pliocene to recent.
3. The northern sector of the WPWP (green box in Figure **F3**): Sites U1488 and U1489 at the southern end of the Eauripik Rise and Site U1490 at its northern end recovered low–sedimentation rate sequences spanning the late Oligocene/early Miocene to recent.

These sites will allow us to address the research themes discussed below.

Investigating millennial-scale climate variability in the IPWP

The origin of millennial-scale climate variability and its spatial and temporal extent are significantly less well understood than mechanisms responsible for orbital climate variability. Most hypotheses attribute millennial-scale changes during the last glacial interval to either instabilities in the Northern Hemisphere ice sheets (e.g., MacAyeal, 1993) or a response to variations in Atlantic Meridional Overturning Circulation (e.g., Rahmstorf, 2002) driven by meltwater inputs to the North Atlantic (e.g., Clark et al., 2001, 2004). Much of the evidence for millennial-scale climate variability comes from the North Atlantic Ocean and from regions directly affected by climate variability in that region. These records suggest a strong link between millennial-scale variability and ice sheet instability, primarily during glacial periods (McManus et al., 1999). In low-latitude and tropical regions, millennial-scale variability is mainly expressed as changes in precipitation. Paleoprecipitation records suggest a southward shift in the ITCZ position apparently synchronous with North Atlantic cold events including the Younger Dryas, Heinrich Event 1, and marine isotope Stage (MIS) 3 stadials (Stott et al., 2002, 2004; Oppo et al., 2003; Dannenmann et al., 2003; Gibbons et al., 2014). These results are consistent with models that suggest climate conditions at high latitudes influence the position of the ITCZ (Broccoli et al., 2006; Chiang and Bitz, 2005). The global extent and apparent synchroneity of millennial-scale variability have been attributed to fast transmission of climate signals through the atmosphere in response to North Atlantic climate change (Schmittner et al., 2003; Gibbons et al., 2014). However, other studies suggest that changes in orbital insolation can induce changes in the mean state of tropical climate that in turn affect tropical dynamics (e.g., monsoon and ENSO variability) operating on millennial or shorter timescales (Clement et al., 2001; Koutavas et al., 2002, 2006; Stott et al., 2002). Accordingly, changes in the distribution of the tropical Pacific SST may have large impacts on global temperatures (Clement et al., 2001; Brown et al., 2015) and low- to mid-latitude heat and moisture transport, which can amplify small radiative perturbations (Tachikawa et al., 2013).

As a major source of heat and moisture, the IPWP may have played an important role in millennial-scale variability through changes in its spatial extent and/or its SST and consequently on the air-sea heat and moisture exchange. Obtaining long records from the IPWP with comparable resolution to the Greenland ice cores, Chinese speleothems, and high-resolution sediment cores from other regions will provide insight into the mechanisms driving centennial- to millennial-scale climate variability in the context of changes in background climate states.

Reconstructing orbital-scale climate variability through the Neogene

Significant glacial–interglacial variability characterizes SST reconstructions from the WPWP with the glacial–interglacial temperature amplitude increasing from ~2°C in the Pliocene to 3°C in the Pleistocene (de Garidel-Thoron et al., 2005; Medina-Elizalde and Lea, 2005, 2010). These changes are also associated with changes in surface-water $\delta^{18}O_{seawater}$, suggesting concomitant hydroclimate changes. Because the tropical Pacific is located far from the polar ice sheets, studies have suggested that the glacial–interglacial variability of tropical Pacific SST is mostly driven by changes in atmospheric pCO_2 (e.g., Lea, 2004; Hansen et al., 2008) and to a lesser extent by changes in local insolation (e.g., Tachikawa et al., 2013). In addition, there may also be strong extratropical controls of WPWP temperatures due to ocean dynamical processes. For example, the presence of significant obliquity variability in SST records from the WPWP throughout the past ~2 My attests to strong linkages with high-latitude climate variability (de Garidel-Thoron et al., 2005) likely transported through the thermocline. The causes and extent of past precipitation changes in the WPWP are not well constrained in terms of the relative importance of changes in boundary conditions in the equatorial Pacific compared to the high latitudes, their relationship to equatorial dynamics and the position of the ITCZ, and their associated climate system feedbacks (Figure **F2**).

Lithologic proxy records of precipitation from the western equatorial Pacific suggest that precession-driven interhemispheric changes in local insolation exert the strongest control on equatorial Pacific hydroclimate, primarily associated with the migration of the ITCZ (Kissel et al., 2010; Tachikawa et al., 2011) and possibly modulated by ENSO-type processes (Dang et al., 2015). Notably, these precipitation records show no glacial–interglacial cyclicity and no clear causal linkage to the climate of the North Atlantic (e.g., Kissel et al., 2010; Tachikawa et al., 2011; Carolin et al., 2013). However, recent studies suggest that southward displacement of the ITCZ during deglaciations may have played an important role in the inception of glacial terminations through its influence on the position of the southwesterly winds as the wind systems are linked. A southward shift of the southern westerly jet may have led to increased upwelling of CO_2-rich deep water around Antarctica, which in turn enhanced the deglaciation (Denton et al., 2010; Anderson et al., 2009). Modeling studies, supported by new records, confirm the idea of "interhemispheric teleconnection," whereby warming (cooling) of the Northern Hemisphere causes both the ITCZ and the Southern Hemispheric mid-latitude jet to shift northward (southward) (Lee et al., 2011; Ayliffe et al., 2013; Ceppi et al., 2013). Investigating these interconnections and their evolution throughout the Neogene under different background climate states is one of the overarching goals of this expedition.

On million-year timescales, the relationships between different equilibrium states of the tropical Pacific and changes in the Equator-to-pole temperature gradient have likely affected ocean circulation and thus global climate evolution from the middle Miocene through the late Pleistocene. Specifically, long-term Cenozoic cooling was interrupted by periods of relative global warmth during the Middle Miocene Climate Optimum (MMCO; ~17–15 Ma) and the early Pliocene warm period (4.5–3 Ma) (Zachos et al., 2001). The period since the MMCO interval is of special interest due to a perceived decoupling between global SSTs and variations in atmospheric pCO_2 (e.g., LaRiviere et al., 2012). The early Pliocene warm

period is also of particular interest because global surface temperatures were ~2°–3°C higher than at present (Dowsett et al., 2009), which is comparable with projections for the twenty-first century, whereas atmospheric pCO_2 was arguably similar to today's levels (~400–450 ppmv) (Kürschner et al., 1996; Pagani et al., 2010; Fedorov et al., 2013). Studies suggest that this period was characterized by a reduced Pacific zonal temperature gradient due to substantial warming of eastern equatorial Pacific SST (e.g., Wara et al., 2005). However, the spatial extent and magnitude of SST change in the WPWP and their implications for tropical precipitation are debated (Brierley et al., 2009; Fedorov et al., 2010; Zhang et al., 2014; Ravelo et al., 2014), and new records from this expedition will contribute to this discussion.

The MMCO was also characterized by a warm and humid climate (Mosbrugger et al., 2005; Bruch et al., 2007), with some evidence for even weaker meridional temperature gradients than in the Pliocene (Flower and Kennett, 1994; Bruch et al., 2007; Holbourn et al., 2010), although there are very few data available, particularly from the WPWP, to help constrain global temperature gradients. After the MMCO, the climate cooled gradually through the late Miocene in many regions but was still warmer than today. It is currently debated whether the WPWP temperature was, on average, similar to today through the late Miocene (Nathan and Leckie, 2009) or significantly warmer (Zhang et al., 2014). The climate mechanisms that explain past warmth during the MMCO, the late Miocene, and the early Pliocene are not fully understood, but greenhouse gas forcing and ocean circulation are considered to be important factors. Recent data suggest that pCO_2 was higher than today during the MMCO (Kürschner et al., 2008; Retallack, 2009; Zhang et al., 2013; Greenop et al., 2014) and in the early Pliocene warm period (Pagani et al., 2010; Seki et al., 2010). However, reconstructions suggest pCO_2 was relatively low in the late Miocene, similar to levels during the Pleistocene, even though the climate was relatively warm and Northern Hemisphere ice sheets were only starting to develop. At face value, this scenario indicates that more than one climate state (i.e., late Miocene warmth and late Pleistocene glaciation) is possible for a given pCO_2 forcing. Thus, factors other than pCO_2, such as the influence of tectonic opening or closure of oceanic gateways on ocean circulation (Cane and Molnar, 2001; Steph et al., 2010) or different modes of deepwater production and circulation (Woodard et al., 2014), may have played a critical role in determining global climate. In particular, tectonic changes affecting the transport of water from the western Pacific to the Indian Ocean is one mechanism proposed to explain changes in global climate (Cane and Molnar, 2001).

Reconstructing changes in the ITF through the Neogene

Hydrographic measurements indicate that nearly all of the ITF water in the Makassar Strait derives from the relatively cool NPSTW and NPIW (Gordon and Fine, 1996; Gordon and Susanto, 1999). At present, the contribution of denser SPSTW from the NGCC to the ITF is limited because of the proximity of West Papua to the Equator (Gordon and Fine, 1996; Hautala et al., 1996; Johnson and McPhaden, 1999; Cane and Molnar, 2001). On longer timescales, the strongest controls on the properties and strength of the ITF are likely sea level changes leading to the exposure and flooding of the Sunda shelf (Xu et al., 2008; Linsley et al., 2010) and tectonic closure of the Indonesian seaways, which likely influenced regional and global climate (Cane and Molnar, 2001; Kuhnt et al., 2004). Based on preliminary results from IODP Expedition 356, for example, it has been suggested that long-term changes in the ITF exerted a strong control on the climate of northwest Australia (Christensen et al., 2017). By reconstructing the thermocline structure at Expedition 363 sites located in the heart of the WPWP and off northwest Australia, near the exit of the ITF into the Indian Ocean, we can distinguish changes in ITF transport due to tectonic versus global climate changes from the late Neogene to present. New high–sedimentation rate cores enable us not only to study long-term changes in ITF transport (e.g., Karas et al., 2009, 2011) but also to assess the long-term variability of the ITF at orbital and suborbital timescales.

Assessing the vertical density structure of the IPWP during the LGM

The spatial pattern of temperature and salinity in the ocean represents the distribution of different water masses and is used to infer deep-ocean circulation. It would be ideal to use the same approach to reconstruct ocean circulation in the past, but we are currently limited by the availability of proxies with sufficient accuracy to reconstruct temperature and salinity variability in the past. Specifically, benthic foraminiferal $\delta^{18}O$ records cannot unequivocally be interpreted in terms of changes in ice volume, temperature, and salinity because these factors all affect the isotopic composition of the foraminifer tests. For the LGM, we can resolve this uncertainty by using the approach developed for reconstructing the chlorinity (as a measure of salinity) and $\delta^{18}O$ of seawater from interstitial water profiles of deep-ocean sediment (Adkins et al., 2002; Schrag and DePaolo, 1993; Schrag et al., 1996).

The LGM left the ocean on average ~3.5% enriched in salt and ~1.0‰ enriched in $\delta^{18}O$ from the growth of land-based ice sheets. However, these enrichments vary locally, depending on past changes in circulation and water mass properties. Using high-precision [Cl^-] and $\delta^{18}O$ measurements of the interstitial water profiles downhole to ~150 m below seafloor (mbsf) and applying a 1-D advection/diffusion equation, the amplitude of the seawater salinity and $\delta^{18}O$ change can be estimated, and when combined with foraminifer $\delta^{18}O_{calcite}$, these data can be used to estimate the temperature and density of the LGM ocean. Previous studies show that most of the LGM deep ocean was near freezing, whereas deep ocean salinity varied more than that of the modern ocean (Adkins et al., 2002). Specifically, the available interstitial water data suggest that the LGM density gradient along the Atlantic Ocean was very different from today, with the saltiest water forming around Antarctica during the LGM as opposed to around Greenland in the modern ocean (Adkins et al., 2002). The overall picture is one of a salinity-stratified ocean with different water mass geometries. Enhanced vertical stratification at the LGM would have had significant implications for the carbon budget of the ocean and pCO_2 of the atmosphere at that time (Broecker and Barker, 2007). However, most of the presently available data come from the Atlantic Ocean, and to date there is only one record from the southern Pacific Ocean (ODP Site 1123; Adkins et al., 2002). New interstitial water profiles collected during Expedition 363 span a water depth of ~1000–3800 mbsl and will allow us to reconstruct the stratification of the equatorial Pacific Ocean at the LGM.

Using interstitial water profiles to reconstruct diagenetic processes and their implications for seawater composition

The study of uranium (U) and sulfur (S) interstitial water chemistry will be important for evaluating diagenetic processes at the

sites targeted by Expedition 363, with significant implications for our understanding of the proxy data generated with expedition samples and of the Earth system as a whole. The $^{234}U/^{238}U$ ratios of interstitial water have been demonstrated to be a sensitive indicator of the amount of silicate dissolution and calcite recrystallization in deep-marine sediment over submillion-year timescales (Maher et al., 2004). Furthermore, the $^{234}U/^{238}U$ ratio of the globally integrated U flux from interstitial water to seawater is poorly known. $^{234}U/^{238}U$ measurements on interstitial water collected from the range of depositional environments sampled by Expedition 363 will provide an important indicator of the diagenetic alteration of carbonates and will place constraints on the global composition of the uranium outflux from marine sediments. Such data will be important for evaluating the robustness of carbonate-based environmental proxies generated by Expedition 363 postcruise research. These data will also provide insight regarding the influence of marine diagenesis on the global $^{234}U/^{238}U$ budget. A better understanding of this budget should allow for improvement of the U-series dating calibration used in many records of Pleistocene oceanographic changes (e.g., Hines et al., 2015) and better constrain the amount of chemical weathering on glacial–interglacial timescales (e.g., Chen et al., 2016).

The diagenesis of S and associated isotopic mass balance models of the ocean play an important role in our understanding of the progressive oxygenation of Earth's surface on geological timescales and of the relative burial fluxes of oxidized and reduced S species in modern marine sediment. Although ample studies (e.g., Jørgensen, 1977; Lyons et al., 2004) have documented S diagenesis through measurements of the S isotopic composition of pyrite and aqueous S species in shallow-shelf sediment, our knowledge of the S isotopic composition of pyrite buried in deep-sea sediment under generally oxic water columns is incomplete. Expedition 363 presents an excellent opportunity to study S diagenesis through aqueous and solid phase $\delta^{34}S$ measurements in relatively deep ocean sites across a range of water depths (875–3421 mbsl), sedimentation rates, and terrigenous sediment fluxes, all of which may potentially influence S diagenetic processes. High sedimentation rates through the Pleistocene at several sites (e.g., Sites U1484 and U1485) should also allow exploration of the potential for these influences to impact sulfur diagenesis and thus pyrite $\delta^{34}S$ on glacial–interglacial timescales. Additional measurements of interstitial water samples, including boron (B), lithium (Li), magnesium (Mg), calcium (Ca), silica (Si), and strontium (Sr) elemental concentrations and their isotopic ratios, will be used to study processes related to $CaCO_3$ diagenesis and in situ weathering of silicate minerals in the sediment and the implications for changes in seawater composition during the Neogene.

Specific scientific objectives

Operations during Expedition 363 worked toward the following scientific objectives:

- Determine the spatial extent of sea-surface and thermocline temperature variability in the IPWP under different climate background states in relation to changes in radiative forcing (CO_2 and insolation) to better constrain climate sensitivity throughout the Neogene;
- Reconstruct the evolution of the Asian-Australian monsoon system and IPWP precipitation since the middle Miocene;
- Reconstruct variations in surface, thermocline, intermediate and deepwater temperatures, heat content, and carbonate (CO_3^{2-}) chemistry over orbital timescales;
- Document the spatial and temporal extent of millennial-scale climate variability in the IPWP as expressed in the hydrologic cycle and sea surface and thermocline temperatures;
- Assess the evolution of millennial- and orbital-scale climate variability through the Neogene including an evaluation of a possible relationship between global ice volume and the magnitude of climate variability in the IPWP;
- Reconstruct ITF variability on millennial to orbital timescales in relation to climatic and tectonic changes since the middle Miocene;
- Reconstruct the vertical density structure of the IPWP during the LGM; and
- Assess the effects of carbonate and silicate rock diagenesis on interstitial water chemistry and its implications for Neogene changes in seawater composition.

Site summaries

Site U1482

Background and objectives

Site U1482 (proposed Site WP-12D) is located on the northwest Australian margin at 15°3.32′S, 120°26.10′E in 1466 m water depth (Figure **F7**). The site is situated at Shotpoint 440 on seismic Line HBR2000A-3032, ~581 m northwest of the crosspoint of seismic Lines HBR2000A-3032 and BR98-84. The top of the first prominent reflector, originally interpreted as the middle Miocene sequence boundary (Mi-3; 13.8 Ma), is 0.55 s two-way traveltime (TWT) below the seafloor, equivalent to ~500 mbsf (Rosenthal et al., 2016). Site U1482 is on the Scott Plateau, which corresponds to a subsided platform area that forms the northwestern flank of the northeast-trending Browse Basin (Keep et al., 2007; Hall, 2012). This region, which is adjacent to some of the oldest ocean crust still in the world's oceans (Argo Abyssal Plain), has remained a stable passive margin since the breakup of Gondwanaland and the separation of northwest Australia from the Tethyan landmass (Gradstein, 1992). As a result of the northward movement of the Australian plate, continuous Neogene deformation along the normal faults that bound the Scott Plateau has led to the amplification of relief between the Browse Basin and the Scott Plateau and may have resulted in some of the downslope transport seen in the seismic profiles (Keep et al., 2007) and sediment deformation in the cores recovered at this site.

The Mesozoic section beneath the Scott Plateau is strongly influenced by breakup-related tectonics that form the acoustic basement through much of the Scott Plateau area (Stagg and Exon, 1981). The postbreakup sedimentary succession forms an ~2000 m thick, relatively uniform blanket over the Scott Plateau and the northeastern margin of the Browse Basin. The extended Miocene to recent sedimentary succession recovered at Site U1482 provides an ideal archive to reconstruct the climate and circulation history at the southwestern edge of the IPWP at a higher resolution than is possible at nearby deep-sea ODP sites (e.g., Site 761 on the Wombat Plateau; Holbourn et al., 2004) (Figure **F3**).

The location of Site U1482 within the prominent hydrographic front separating tropical and subtropical water masses makes it suitable to monitor changes in the southern extent of tropical warm water related to circulation and/or global climate trends. The site is situated close to the oceanographic front between relatively cool, nutrient-rich water carried northward in the Eastern Indian Ocean by the West Australian Current and warm, oligotrophic Leeuwin Current waters, which results in a steep north–south SST gradient (Figure **F1**). This strategic location will allow reconstruction of the

Figure F7. Northwest Australian margin (yellow box in Figure F3) showing the location of Sites U1482 and U1483 (yellow circles) on the Scott Plateau. Also indicated are the three main exit passages of the ITF into the eastern Indian Ocean: Lombok Strait (sill depth = 350 m), Ombai Strait (sill depth = 3250 m), and Timor Strait (sill depth = 1890 m). Contour interval = 500 m. Bathymetric data from Amante and Eakins (2009).

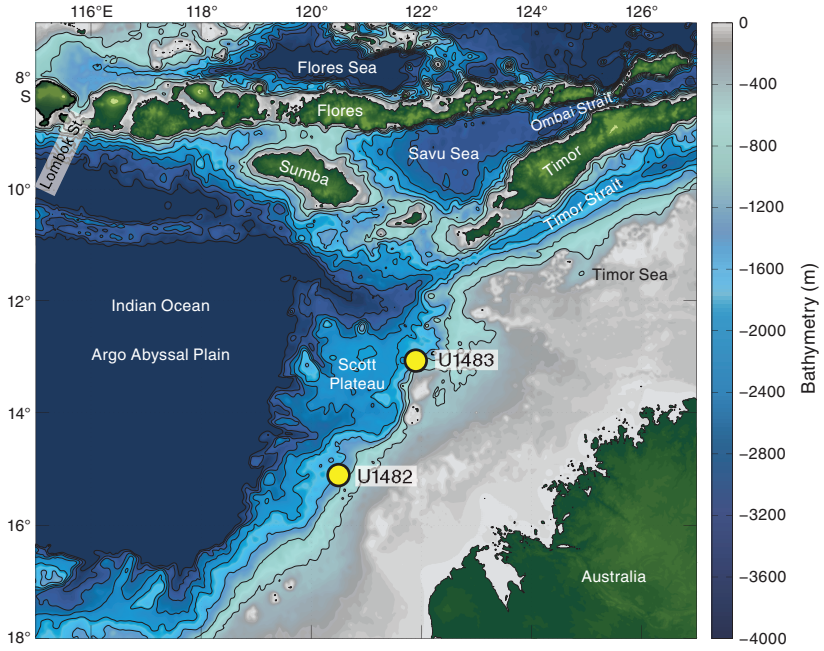

southwestern extent of the IPWP and monitoring of the ITF outflow into the Indian Ocean since the early late Miocene.

The extended sediment archive recovered at Site U1482 will enable reconstruction of climate variability on orbital timescales over the past ~10 My, which will complement high-resolution records from the Pacific, Atlantic, and Southern Oceans and will be crucial for constraining regional and global circulation modes and Miocene ice volume variations. The new Pliocene record from Site U1482 is also ideally suited to test the hypothesis of a major restriction of warm water throughflow originating from the South Pacific Ocean between 3 and 5 Ma due to the northward movement of Papua New Guinea, which may have been a key factor in the aridification of East Africa and hominid evolution (Cane and Molnar, 2001).

Operations

After a 1514 nmi transit from Singapore, the vessel stabilized over Site U1482 at 1524 h (all times are local; UTC + 8 h) on 16 October 2016. We cored four holes at Site U1482 (Table **T1**). The original operations plan called for three holes, the first to APC refusal, followed by two APC holes with XCB coring to 490 mbsf (our approved depth of penetration for the site). The plan was modified to core to total depth (490 mbsf) in the first hole to determine the operations plan for the remaining holes.

We reached APC refusal at ~345 mbsf in Hole U1482A, which was cored using nonmagnetic hardware and the Icefield MI-5 core orientation tool. The advanced piston corer temperature tool (APCT-3) was deployed on Cores 4H (31.4 mbsf), 7H (59.9 mbsf), 10H (88.4 mbsf), and 13H (116.9 mbsf). We opted to deepen the hole with the half-length APC (HLAPC) system, which reached 380 mbsf before refusal. We then switched to the XCB system to core to the total approved depth of 490 mbsf. Hole U1482B was APC cored to 343.6 mbsf and then HLAPC cored to 366.6 mbsf. This hole included five intervals drilled without coring to avoid core gap alignment for stratigraphic correlation. Because the age of the sediment at the bottom of Hole U1482A was several million years younger than anticipated, we requested and received permission to core deeper at the site. Hole U1482C was APC cored to 335.4 mbsf and then XCB cored to 534.1 mbsf. We opted to terminate drilling at that depth due to deteriorating calcareous microfossil preservation deeper than 500 mbsf and the increasing length of time required to cut cores.

After conditioning the hole for logging, we conducted two downhole logging runs using the triple combination (triple combo) and Formation MicroScanner (FMS)-sonic tool strings in Hole U1482C. The triple combo tool string reached the bottom of the hole at 533.4 m wireline depth below seafloor. The FMS-sonic tool string encountered a slurry of fine-grained fill and reached only 517 m WSF. Two upward passes were conducted with the FMS-sonic tool string. Following logging, we opted to core Hole U1482D to target three core gaps in the stratigraphic section. We took one core at the seafloor to establish the seafloor depth before drilling ahead to 137.0 mbsf. We then took eight APC cores to 213.0 mbsf, successfully covering the targeted core gaps. We then terminated the hole, ending operations at Site U1482 at 1800 h on 25 October. Total time spent at Site U1482 was 218.5 h (9.1 days).

A total of 163 cores were collected at this site. The APC coring system was deployed 115 times, collecting 1128.0 m of sediment over 1077.3 m of penetration (104.7%). The HLAPC coring system was deployed 13 times, recovering 57.01 m of sediment over 55.3 m of penetration (103.1%). The XCB coring system was deployed 35 times, collecting 305.32 m of sediment over 304 m of penetration (100.4%). Total recovery for Site U1482 was 1490.33 m of sediment over 1436.6 m of coring (103.7%).

Principal results

The sediment cored at Site U1482 is assigned to a single lithologic unit composed of ~535 m of upper Miocene to Pleistocene nannofossil ooze/chalk with varying amounts of clay and foraminifers (Figure **F8**). Lithologic Unit I is divided into four subunits. Subunit IA is an ~120 m thick sequence of Pleistocene light greenish

Table T1. Expedition 363 hole summary. DSF = drilling depth below seafloor. APC = advanced piston corer, HLAPC = half-length APC, XCB = extended core barrel. **Download table in CSV format.**

Hole	Latitude	Longitude	Water depth (m)	Penetration DSF (m)	Cored interval (m)	Recovered length (m)	Recovery (%)	Drilled interval (m)	Drilled interval (*N*)	Total cores (*N*)	APC cores (*N*)	HLAPC cores (*N*)	XCB cores (*N*)
U1482A	15°3.3227′S	120°26.1049′E	1467.70	490.0	490.0	505.88	103.24	0.0	0	58	37	8	13
U1482B	15°3.3142′S	120°26.0988′E	1464.49	366.6	349.1	365.82	104.79	17.5	5	40	35	5	0
U1482C	15°3.3298′S	120°26.1135′E	1465.19	534.1	517.1	535.86	103.63	17.0	4	56	34	0	22
U1482D	15°3.3305′S	120°26.0920′E	1466.13	213.0	80.4	82.77	102.95	132.6	1	9	9	0	0
U1483A	13°05.2382′S	121°48.2424′E	1732.93	293.3	293.3	308.58	105.21	0.0	0	31	31	0	0
U1483B	13°05.2371′S	121°48.2538′E	1734.01	287.0	287.0	301.62	105.09	0.0	0	31	31	0	0
U1483C	13°05.2479′S	121°48.2537′E	1731.19	284.8	281.8	292.42	103.77	3.0	1	30	30	0	0
U1484A	03°07.9228′S	142°46.9699′E	1030.93	223.2	223.2	220.60	98.84	0.0	0	27	21	6	0
U1484B	03°07.9223′S	142°46.9809′E	1030.48	222.9	220.9	220.51	99.82	2.0	1	30	17	13	0
U1484C	03°07.9335′S	142°46.9822′E	1030.77	221.4	219.4	225.46	102.76	2.0	1	31	17	14	0
U1485A	03°06.1585′S	142°47.5750′E	1144.75	300.8	300.8	312.36	103.84	0.0	0	44	20	24	0
U1485B	03°06.1584′S	142°47.5854′E	1145.34	297.7	295.7	291.18	98.47	2.0	1	46	20	26	0
U1485C	03°06.1574′S	142°47.5991′E	1145.83	27.5	27.5	29.35	106.73	0.0	0	3	3	0	0
U1485D	03°06.1574′S	142°47.5867′E	1144.43	63.9	62.9	68.22	108.46	1.0	1	7	7	0	0
U1486A	02°22.3375′S	144°36.0796′E	1330.33	9.5	9.5	9.95	104.74	0.0	0	1	1	0	0
U1486B	02°22.3368′S	144°36.0794′E	1333.83	211.2	211.2	215.49	102.03	0.0	0	23	23	0	0
U1486C	02°22.3478′S	144°36.0798′E	1334.50	201.3	197.3	172.70	87.53	4.0	2	21	21	0	0
U1486D	02°22.3484′S	144°36.0690′E	1334.10	186.5	162.7	166.53	102.35	23.8	1	18	18	0	0
U1487A	02°19.9979′S	144°49.1627′E	873.93	144.2	144.2	146.43	101.55	0.0	0	16	16	0	0
U1487B	02°19.9975′S	144°49.1746′E	873.63	144.3	144.3	148.73	103.07	0.0	0	18	14	4	0
U1488A	02°02.5891′N	141°45.2864′E	2603.40	314.5	314.5	327.20	104.04	0.0	0	35	32	3	0
U1488B	02°02.5901′N	141°45.2966′E	2604.40	304.9	304.9	315.77	103.57	0.0	0	33	33	0	0
U1488C	02°02.5793′N	141°45.2974′E	2604.00	159.3	159.3	153.60	96.42	0.0	0	17	17	0	0
U1489A	02°07.1976′N	141°01.6654′E	3419.80	9.5	9.5	9.53	100.32	0.0	0	1	1	0	0
U1489B	02°07.1984′N	141°01.6757′E	3419.50	129.2	129.2	120.66	93.39	0.0	0	14	14	0	0
U1489C	02°07.1772′N	141°01.6746′E	3423.68	385.6	385.6	376.35	97.60	0.0	0	42	29	2	11
U1489D	02°07.1761′N	141°01.6651′E	3421.55	385.6	238.8	229.24	96.00	146.8	1	26	14	0	12
U1490A	05°48.9492′N	142°39.2599′E	2341.03	382.8	382.8	367.35	95.96	0.0	0	44	27	4	13
U1490B	05°48.9507′N	142°39.2698′E	2339.72	262.9	258.9	267.60	103.36	4.0	2	31	24	7	0
U1490C	05°48.9385′N	142°39.2690′E	2341.27	170.0	164.0	168.24	102.59	6.0	2	18	18	0	0
			Totals:	7227.5	6865.8	6956.00		361.7	23	801	614	116	71

Hole	Latitude	Longitude	Date started (2016)	Time started UTC (h)	Date finished (2016)	Time finished UTC (h)	Time on hole (days)
U1482A	15°3.3227′S	120°26.1049′E	16 Oct	0730	19 Oct	0810	3.03
U1482B	15°3.3142′S	120°26.0988′E	19 Oct	0810	20 Oct	1600	1.33
U1482C	15°3.3298′S	120°26.1135′E	20 Oct	1600	24 Oct	1500	3.96
U1482D	15°3.3305′S	120°26.0920′E	24 Oct	1500	25 Oct	1000	0.79
U1483A	13°05.2382′S	121°48.2424′E	25 Oct	2230	27 Oct	1650	1.76
U1483B	13°05.2371′S	121°48.2538′E	27 Oct	1650	28 Oct	1810	1.06
U1483C	13°05.2479′S	121°48.2537′E	28 Oct	1810	30 Oct	0000	1.24
U1484A	03°07.9228′S	142°46.9699′E	6 Nov	1245	7 Nov	1755	1.22
U1484B	03°07.9223′S	142°46.9809′E	7 Nov	1755	8 Nov	2250	1.20
U1484C	03°07.9335′S	142°46.9822′E	8 Nov	2250	9 Nov	2345	1.04
U1485A	03°06.1585′S	142°47.5750′E	9 Nov	2345	11 Nov	1210	1.52
U1485B	03°06.1584′S	142°47.5854′E	11 Nov	1210	12 Nov	2125	1.39
U1485C	03°06.1574′S	142°47.5991′E	12 Nov	2125	13 Nov	0255	0.23
U1485D	03°06.1574′S	142°47.5867′E	13 Nov	0255	13 Nov	1330	0.44
U1486A	02°22.3375′S	144°36.0796′E	13 Nov	2321	14 Nov	0600	0.28
U1486B	02°22.3368′S	144°36.0794′E	14 Nov	0600	15 Nov	0250	0.87
U1486C	02°22.3478′S	144°36.0798′E	15 Nov	0250	16 Nov	0010	0.89
U1486D	02°22.3484′S	144°36.0690′E	16 Nov	0010	17 Nov	0018	1.01
U1487A	02°19.9979′S	144°49.1627′E	17 Nov	0145	17 Nov	2040	0.79
U1487B	02°19.9975′S	144°49.1746′E	17 Nov	2040	18 Nov	1215	0.65
U1488A	02°02.5891′N	141°45.2864′E	19 Nov	1800	21 Nov	1520	1.89
U1488B	02°02.5901′N	141°45.2966′E	21 Nov	1520	23 Nov	0140	1.43
U1488C	02°02.5793′N	141°45.2974′E	23 Nov	0140	24 Nov	0030	0.95
U1489A	02°07.1976′N	141°01.6654′E	24 Nov	0442	24 Nov	1515	0.44
U1489B	02°07.1984′N	141°01.6757′E	24 Nov	1515	25 Nov	1355	0.94
U1489C	02°07.1772′N	141°01.6746′E	25 Nov	1355	27 Nov	1900	2.21
U1489D	02°07.1761′N	141°01.6651′E	27 Nov	1900	29 Nov	1612	1.88
U1490A	05°48.9492′N	142°39.2599′E	30 Nov	1400	2 Dec	1655	2.12
U1490B	05°48.9507′N	142°39.2698′E	2 Dec	1655	4 Dec	0040	1.32
U1490C	05°48.9385′N	142°39.2690′E	4 Dec	0040	5 Dec	1942	1.79

Figure F8. Site U1482 results summary. NGR = natural gamma radiation, cps = counts per second, MS = magnetic susceptibility, WRMSL = Whole-Round Multisensor Logger.

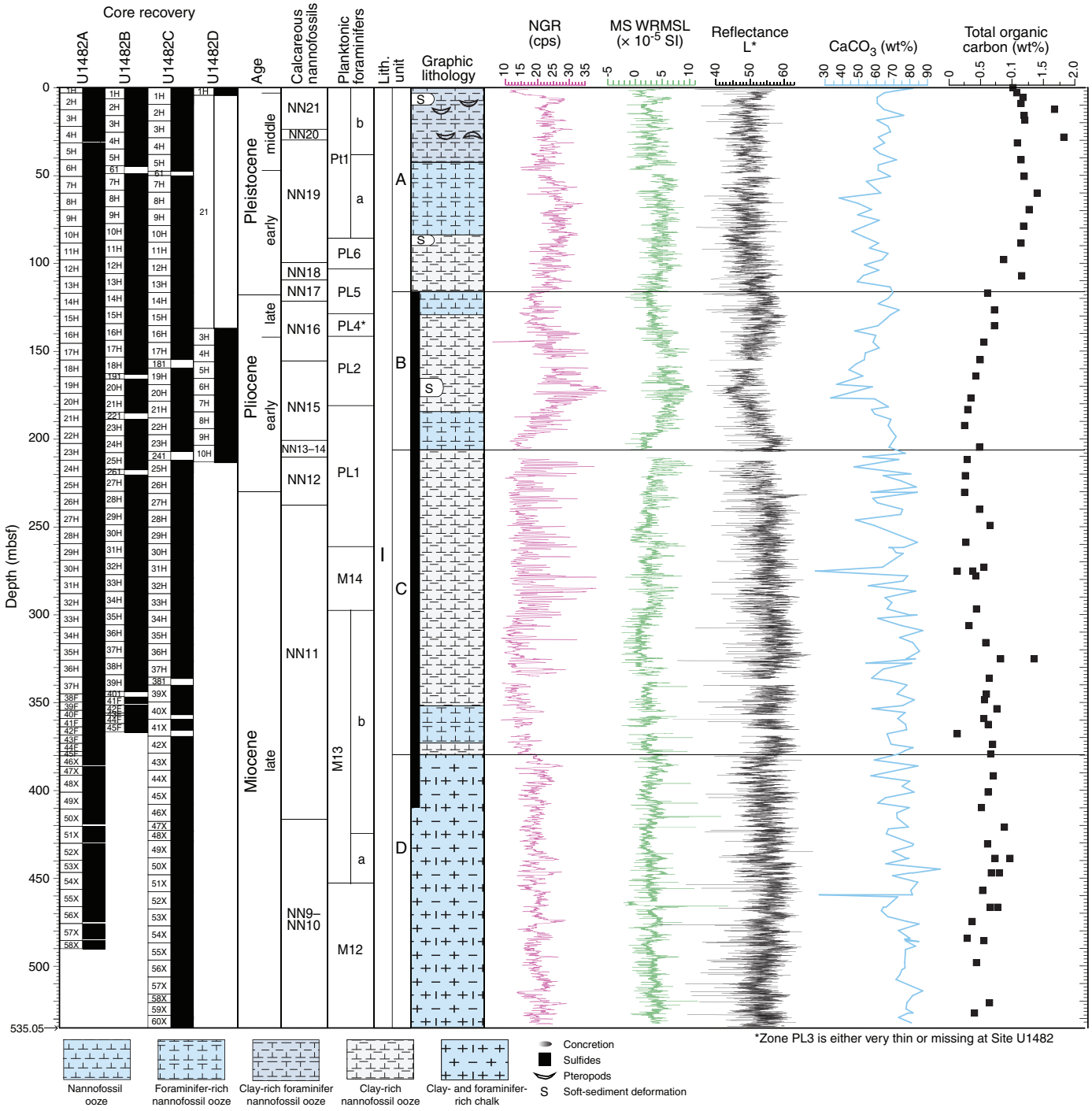

gray clay-rich nannofossil ooze. This subunit contains pteropods and is largely homogeneous with variable amounts of clay. In the lowermost 40 m of the subunit, dark–light bedding cycles become more evident. The boundary between Subunits IA and IB marks a sharp transition between darker clay-rich foraminifer-rich nannofossil ooze and dominantly lighter nannofossil ooze. Subunit IB (early Pliocene to earliest Pleistocene) is an ~90 m thick greenish gray nannofossil ooze, with clay content increasing toward the middle of the subunit and then decreasing again toward the base. The middle part of Subunit IB also contains an interval of significant soft-sediment deformation at ~170 mbsf. Sulfide specks and nodules are abundant, and foraminifer content increases toward the bottom of the subunit. The base of Subunit IB is the first downhole occurrence of well-defined light–dark cycles. Subunit IC (~160 m thick) consists of upper Miocene to lowermost Pliocene light greenish gray nannofossil ooze with varying abundances of foraminifers and clay. This subunit shows strong color cyclicity at a section scale, with cycles largely reflecting changes in carbonate content (~80 to

Figure F9. Age-depth plot for calcareous nannofossil and planktonic foraminifer (PF) biohorizons, Site U1482. Average sedimentation rates were ~5.9 cm/ky during the late Miocene, ~3.3 cm/ky in the early Pliocene, and ~7 cm/ky in the Pleistocene. Vertical error bars represent the interval between the two samples that defines the biohorizon (often obscured by the biohorizon symbol).

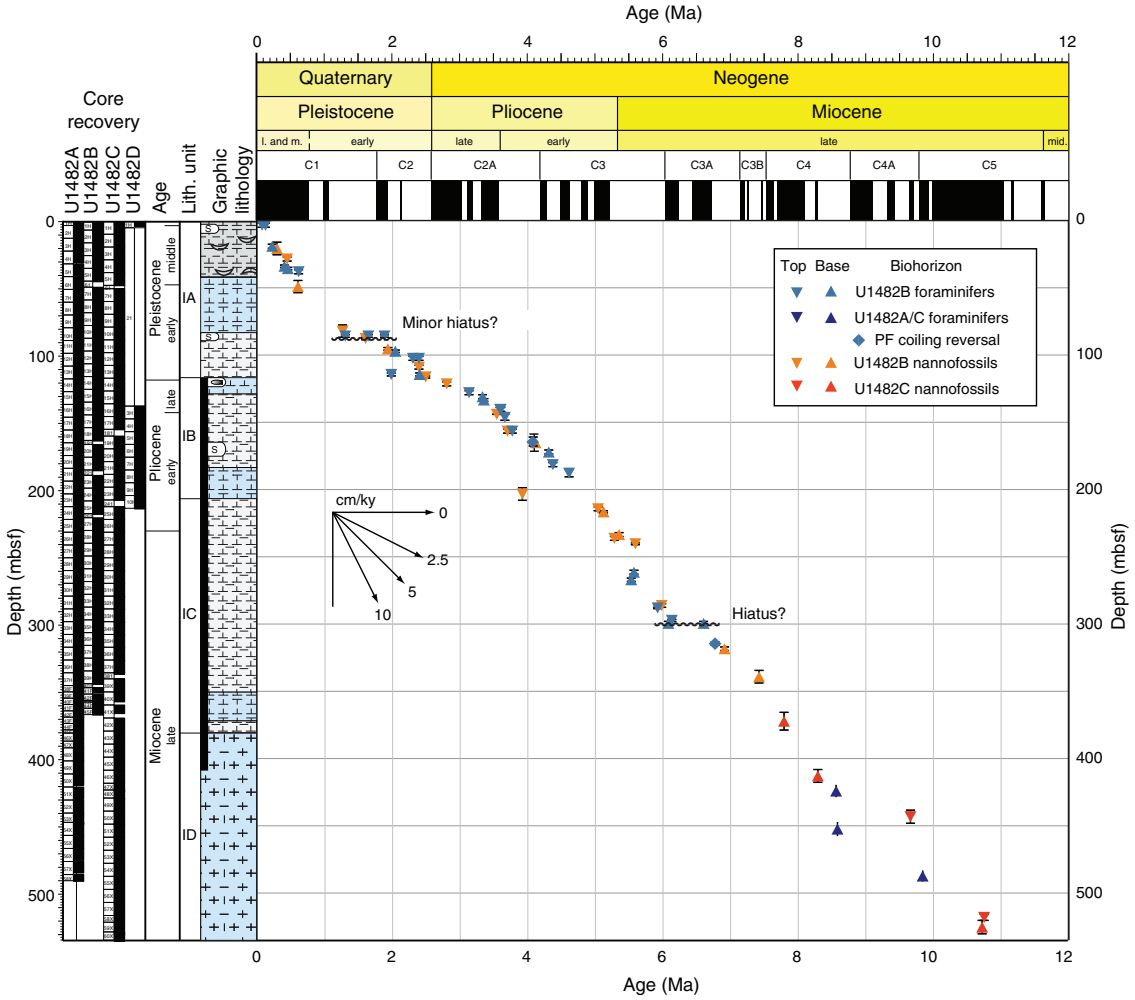

50 wt%). Sulfide patches are abundant throughout. The base of the subunit is defined by the transition from ooze to chalk, which corresponds to the switch from the HLAPC to XCB coring system in Hole U1482A. Subunit ID is composed of upper Miocene light greenish gray chalk with low abundances of clay. Color cycles are on the order of 1.5 to 2 m thick in this subunit. Dissolution of foraminifers has resulted in moldic porosity within the chalk. Foraminifers are also occasionally concentrated in discrete layers in Subunit ID.

Throughout the recovered succession at Site U1482, calcareous nannofossils and planktonic foraminifers are abundant and benthic foraminifers are present and generally show very good to excellent preservation. Planktonic/benthic ratios are typically 99:1. The age model for Site U1482 is based on calcareous nannofossil and planktonic foraminifer biostratigraphy (Figure F9). The base of the late Pleistocene is placed at ~3 mbsf, between biohorizon top *Globigerinoides ruber* (pink) (0.12 Ma) and biohorizon base *Emiliania huxleyi* (0.29 Ma). The base of the middle Pleistocene is placed between 47 and 80 mbsf, between the top of *Globorotalia tosaensis* (0.61 Ma) and the top of *Helicosphaera sellii* (1.26 Ma). There is strong evidence for sedimentary disturbance and reworking in the lower and middle Pleistocene with the potential for a missing section in the lower Pleistocene. The Pliocene/Pleistocene boundary is placed at 118 mbsf (Figure F9). A concentration of planktonic foraminifer biohorizons at 300 mbsf (~6.1–6.6 Ma) suggests a condensed interval or hiatus. This interval is less clear in the calcareous nannofossil biohorizons, although nannofossil age control is sparse at this level. Otherwise, sedimentation appears continuous throughout the upper Miocene and lower Pliocene interval (Figure F9). The age at the base of the recovered succession is constrained as <10.47 Ma by the absence of the planktonic foraminifer *Paragloborotalia mayeri* in the lowermost sample examined, although calcareous nannofossil assemblages suggest a slightly older age of ~10.75 Ma based on identification of the biohorizon top *Helicosphaera walbersdorfensis* (10.72 Ma) and the biohorizon base *Helicosphaera stalis* (10.75 Ma) at ~15 m above the base of Hole U1482C. Calcareous nannofossil and planktonic foraminifer biohorizons are in generally good agreement and indicate sedimentation rates of ~5.9 cm/ky during the late Miocene, decreasing to ~3.3 cm/ky in the early Pliocene. The Pleistocene was characterized by higher sedimentation rates of ~7 cm/ky (Figure F9).

Paleomagnetic investigations at Site U1482 measured natural remanent magnetization (NRM) of archive halves from Holes U1482A–U1482C before and after demagnetization in a peak alternating field (AF) of 15 mT, which effectively removed the vertical overprint induced by the drill string. Fifty 7 cm^3 discrete samples were taken to investigate paleomagnetic carriers and rock magnetic

properties. NRM_{15mT} intensity is higher (~10^{-4} A/m) in the upper 40–60 mbsf of each hole, decreases between 60 and 90 mbsf, and remains low (~10^{-5} A/m) below ~90 mbsf, where it approaches the measurement noise level of the magnetometer. Decreases in magnetic intensity downhole are accompanied by decreases in other ferrimagnetic concentration parameters (anhysteretic remanent magnetization [ARM] and isothermal remanent magnetization [IRM]), a halving of the NRM_{15mT}/NRM intensity, and a coarsening of magnetic grain size (lower ARM/saturation remanent magnetization [SIRM]). These changes are coeval with decreases in interstitial water sulfate (SO_4) and the appearance of pyrite in the sediment associated with the reduction of primary ferrimagnetic oxides and formation of secondary iron sulfides during early sediment diagenesis. In the upper 50–70 mbsf, inclinations plot around those expected for the site latitude, assuming a geocentric axial dipole (GAD) field. Azimuthally corrected declination using the Icefield MI-5 core orientation tool is largely consistent between successive cores but maintains an absolute offset of 150°–180° (i.e., corrected declination values for normal polarity cluster between 150° and 180° instead of 0°). Relatively weak magnetic susceptibility coupled with reduction of ferrimagnetic oxides results in a largely uninterpretable signal below the iron-reduction zone and restricts our geomagnetic interpretation to the upper 50–70 mbsf. Sediment in this zone appears to have been deposited during a period of normal polarity consistent with the Brunhes Chron (C1n).

The physical property data collected for Site U1482 include *P*-wave velocity, gamma ray attenuation (GRA) bulk density, magnetic susceptibility, natural gamma radiation (NGR), and thermal conductivity measurements on whole-round cores from Holes U1482A–U1482D and *P*-wave velocity, thermal conductivity, porosity, and bulk, dry, and grain density measurements on split cores or discrete samples. Despite the relatively homogeneous lithology dominated by nannofossil ooze at this site, physical property parameters display comparable broad-scale features and high-resolution cyclicity throughout the sequence, allowing for correlations among the holes (Figure **F8**). A linear downhole increase is apparent in the thermal conductivity (~1.0–1.5 W/[m·K]), GRA bulk density (~1.4–2.0 g/cm^3), and moisture and density (MAD) dry density (0.8–1.5 g/cm^3) and wet bulk density (1.4–2.0 g/cm^3) records. The decreasing trend in porosity from ~75% to 45% is due to increasing compaction with depth. A broad peak in GRA bulk density, NGR, and magnetic susceptibility centered at ~175 mbsf marks an interval of soft-sediment deformation observed in all holes (Figure **F8**). Downhole formation temperature measurements made with the APCT-3 on Cores 363-U1482A-4H, 7H, 10H, and 13H indicate a geothermal gradient of 48°C/km for the upper ~120 mbsf.

Tie points for stratigraphic correlation were established mainly with Whole-Round Multisensor Logger (WRMSL) magnetic susceptibility data, although some were based on WRMSL GRA bulk density and NGR data. Correlation was challenging due to intervals with very low amplitude variability in the WRMSL and NGR signals, the presence of intervals containing soft-sediment deformation, and variations in the size of core gaps that resulted from a large tidal range of 3–4 m during coring operations at Site U1482. The core composite depth below seafloor (CCSF) depth scale is anchored to the mudline Core 363-U1482B-1H, which is assigned the depth of 0 m CCSF. From this anchor, we worked downhole to establish a composite stratigraphy on a core-by-core basis. We developed a splice from 0–451.2 m CCSF and a composite depth scale to 614.6 m CCSF. The match between the holes is well constrained within the splice, except for intervals of soft-sediment deformation (0–17, 55–84, 104–111, and 207–210 m CCSF) and one core gap at 401 m CCSF. Below 451 m CCSF, we determined tentative correlations between some cores but did not construct a splice, which should be explored as part of postcruise research.

A total of 62 interstitial water samples were analyzed at Site U1482, including 57 whole-round samples and 1 mudline sample from Hole U1482A (from 0 to 489 mbsf) and 4 whole-round samples from Hole U1482C (from 490 to 533 mbsf), to achieve a complete interstitial water profile for the full stratigraphic succession at this site. The interstitial water chemistry at Site U1482 is strongly influenced by the remineralization of organic matter. Total organic carbon (TOC) content is >1.0 wt% in the uppermost ~90 mbsf (Figure **F8**), which is relatively high for an open marine setting. In the upper 120 mbsf, interstitial water profiles of alkalinity, manganese (Mn), SO_4, barium (Ba), Si, and methane reflect the progression from suboxic organic matter degradation to SO_4 reduction. At ~120 mbsf, near-complete consumption of SO_4 and a rapid increase in methane mark the transition to fermentation and anaerobic methane oxidation (AOM). This transition, known as the sulfate–methane transition zone (SMTZ), is also marked by a pronounced increase in dissolved Ba, reflecting both authigenic precipitation and dissolution of sedimentary barite ($BaSO_4$) in underlying sediment. Steady downhole increases in ammonium (NH_4) and bromide (Br) are also consistent with progressive remineralization of organic matter. Ca and Mg concentrations decrease in the upper 120 mbsf, possibly reflecting calcite precipitation. Phosphate (PO_4) decreases over the same depth interval, which may be due to precipitation of apatite, although overall [PO_4] is quite low (<10 μM) and no apatite was detected by XRD analysis. Below 120 mbsf, Mg continues to decrease, whereas Ca slightly increases. Although this increase suggests precipitation of dolomite, downhole trends in potassium (K), B, and Li indicate that ion exchange with clay minerals could contribute to the trends observed in the interstitial water profiles.

Hydrocarbon monitoring shows high methane concentration below the SMTZ, with an average of 6%. However, the ratio of methane to ethane and the gas wetness index suggest that most of the gas has a biogenic origin. Methane concentration decreases to ~3% between ~380 and 530 mbsf, reflecting progressive depletion of available organic matter for methanogenesis. Both ethane and propane profiles largely follow methane but also respond to the increased thermal maturity with depth as a result of the geothermal gradient.

The calcium carbonate ($CaCO_3$) content at Site U1482 fluctuates between 0 and 180 mbsf with an average of ~60 wt% (Figure **F8**). Below 180 mbsf, $CaCO_3$ content increases to ~80 wt%, consistent with the late Miocene to early Pliocene "biogenic bloom" that is most pronounced in the Indo-Pacific region (e.g., Farrell et al., 1995; Gupta and Thomas, 1999).

Two downhole logging tool strings were run in Hole U1482C, the triple combo (NGR, porosity, density, electrical resistivity, and magnetic susceptibility) and the FMS-sonic (NGR, sonic velocity, and electrical resistivity images). The triple combo tool string reached to the bottom of the hole at 533.4 m WSF, whereas the FMS-sonic tool string only reached 517 m WSF after encountering fill in the bottom of the hole. One of the four FMS pads performed poorly, but postacquisition processing corrected the problem. Caliper data show that the borehole was enlarged by ~2.5–10 cm in the upper 250 mbsf, which affected the quality of the density and porosity measurements and resulted in higher variability in those data. Deeper than 350 mbsf, corresponding to the depth where we switched to XCB coring, the borehole walls were remarkably

smooth. This interval corresponds to lithologic Subunit ID, which consists of chalk.

The composite gamma ray log shows an increase between 118 and 207 m wireline matched depth below seafloor (WMSF) (Subunit IB) that correlates with an increase in NGR measured on cores, indicating a higher proportion of clay over that interval. Shallow and deep resistivity measurements show a consistent offset downhole, indicating that there was little or no fluid invasion into the formation. *P*-wave velocity values increase steadily downhole to roughly 2000 m/s at the bottom of the hole. Discrete *z*-axis *P*-wave measurements on cores provide an estimate for the interval from the seafloor to the bottom of the drill pipe at 74.7 m DSF. Combining these data, we were able to establish a velocity profile to the bottom of the hole and derive reliable calculations of depths to key reflectors in the seismic data crossing Site U1482.

Site U1483

Background and objectives

Site U1483 (proposed Site WP-11B) is located on the northwest Australian margin at 13°5.24′S, 121°48.25′E in 1733 m water depth (Figure **F7**). The site is situated on seismic Line BR98-117, 1300 m northeast of the intersection with seismic Line BR98-168 and ~0.8 nmi southeast of the ~40 m long piston Core MD01-2378, which provides insights into late Pleistocene sedimentation and stratigraphy at this location (e.g., Holbourn et al., 2005; Kuhnt et al., 2015). The interpretation of Miocene seismic reflectors is based on comparison to the Australian Geological Survey Organisation regional seismic survey Line 119-04 (well control by Buffon 1 and Brewster 1A) and the BBHR Line 175/10 (well control by Argus 1). A major unconformity marks the top of the prograding sequence at 0.72 s TWT below seafloor and is interpreted as the middle Miocene sequence boundary corresponding to a major sea level drop associated with rapid expansion of the Antarctic Ice Sheet (Mi-3; 13.8 Ma) (Rosenthal et al., 2016).

Site U1483 is situated on the Scott Plateau at the northwestern margin of the northeast-trending Browse Basin (Figure **F7**), which underlies the Australian northwest margin between the onshore Kimberley Basin and the Scott Plateau (Symonds et al., 1994). This region, which is adjacent to some of the oldest ocean crust still in the world's oceans (Argo Abyssal Plain), formed after the breakup of Gondwanaland and the separation of northwest Australia from the Tethyan landmass (Gradstein, 1992). The Mesozoic section beneath the Scott Plateau is strongly influenced by breakup-related tectonism and forms the acoustic basement through much of the Scott Plateau area (Stagg and Exon, 1981). The postbreakup sedimentary succession forms an ~2000 m thick, relatively uniform blanket over the Scott Plateau and the northeastern margin of Browse Basin. Site U1483 is located south of the Sunda arc, where ongoing collision between Australia and the Eurasia/Pacific arc system has occurred since the Miocene (Keep et al., 2007; Hall, 2012). However, intense Neogene faulting is mainly observed in the southernmost parts of the Browse Basin (Barcoo Subbasin), whereas the northern parts are relatively devoid of intense Neogene deformation (Keep et al., 2007).

Site U1483 is located ~142 nmi northeast of Site U1482. Both sites are within the hydrographic transition that separates the warm tropical water of the IPWP and subtropical water masses. Jointly, the two sites are suitable to monitor changes in the southward extent of tropical warm water related to circulation and/or global climate trends. Both sites are close to the oceanographic front between relatively cool, nutrient-rich water carried northward in the Eastern Indian Ocean by the West Australian Current and warm, oligotrophic Leeuwin Current water, which results in a steep north–south SST gradient (Figure **F1**).

The sedimentation rate at Site U1483 is ~9 cm/ky (Holbourn et al., 2005), about twice the rate at Site U1482, which will allow for the reconstruction of late Pliocene to recent paleoceanography at higher resolution than at Site U1482. Combined, the two sites will allow for reconstruction of the southwestern extent of the IPWP since the early late Miocene. Furthermore, the sites are located along the route of the ITF as it exits into the Indian Ocean through the Timor Strait between northwest Australia and Java (Figure **F7**). The Timor Strait is one of the three main exits of the ITF to the eastern Indian Ocean (Gordon, 2005). Thus, Sites U1482 and U1483 are ideally located to monitor changes in the intensity and thermal structure of ITF water masses entering the Eastern Indian Ocean (e.g., Xu et al., 2008).

Operations

After a 142 nmi transit from Site U1482, the vessel stabilized over Site U1483 at 0630 h on 26 October 2016. We cored three holes at Site U1483 (Table **T1**). The original operations plan called for coring to APC refusal (estimated at 250 mbsf), followed by two additional holes deepened to 350 mbsf using the XCB system. Instead, we cored three holes using the APC system to ~290 mbsf, the depth at which we encountered APC refusal. We decided not to deepen the holes to the original planned total depth because we had already reached our primary age target.

Hole U1483A was cored with the APC system using the Icefield MI-5 core orientation tool and nonmagnetic hardware to 293.3 mbsf (Cores 363-U1483A-1H through 31H), where a partial stroke indicated APC refusal. Downhole temperature measurements using the APCT-3 were taken on Cores 4H (37.1 mbsf), 7H (65.6 mbsf), 10H (94.1 mbsf), and 13H (122.6 mbsf), and reliable results were obtained on three of the four deployments. A total of 308.58 m of sediment was recovered over 293.3 m of coring (105%) in Hole U1483A.

Hole U1483B was then cored with the APC system using the Icefield MI-5 core orientation tool and nonmagnetic hardware to 287.0 mbsf (Cores 363-U1483B-1H through 31H). A total of 301.62 m of sediment was collected over this interval (105%). Oriented APC coring using the Icefield MI-5 core orientation tool with nonmagnetic hardware continued in Hole U1483C and reached 284.8 mbsf (Cores 363-U1483C-1H through 31H). One drilled interval (3 m) advanced the hole without coring to avoid alignment of core gaps for stratigraphic correlation. A total of 292.42 m of core was recovered over 281.8 m of coring (104%). Operations at Site U1483 ended at 0800 h on 30 October. Total time spent at the site was 97.5 h (4.1 days).

A total of 92 APC cores were recovered at this site, collecting 902.62 m of sediment over 862.1 m of penetration (105.2%).

Principal results

The sediment cored at Site U1483 is assigned to a single lithologic unit composed of ~293 m of lower Pliocene to recent nannofossil ooze with variable amounts of clay, foraminifers, and siliceous microfossils (primarily diatoms and radiolarians) (Figure **F10**). Tephra layers occur sporadically throughout the unit. Lithologic Unit I is divided into three subunits. Subunit IA is an ~56 m sequence of middle Pleistocene to recent greenish gray clay-bearing and clay-rich nannofossil ooze. Sponge spicules and mollusk shell fragments are common throughout this subunit, whereas pteropods

Figure F10. Site U1483 results summary. cps = counts per second.

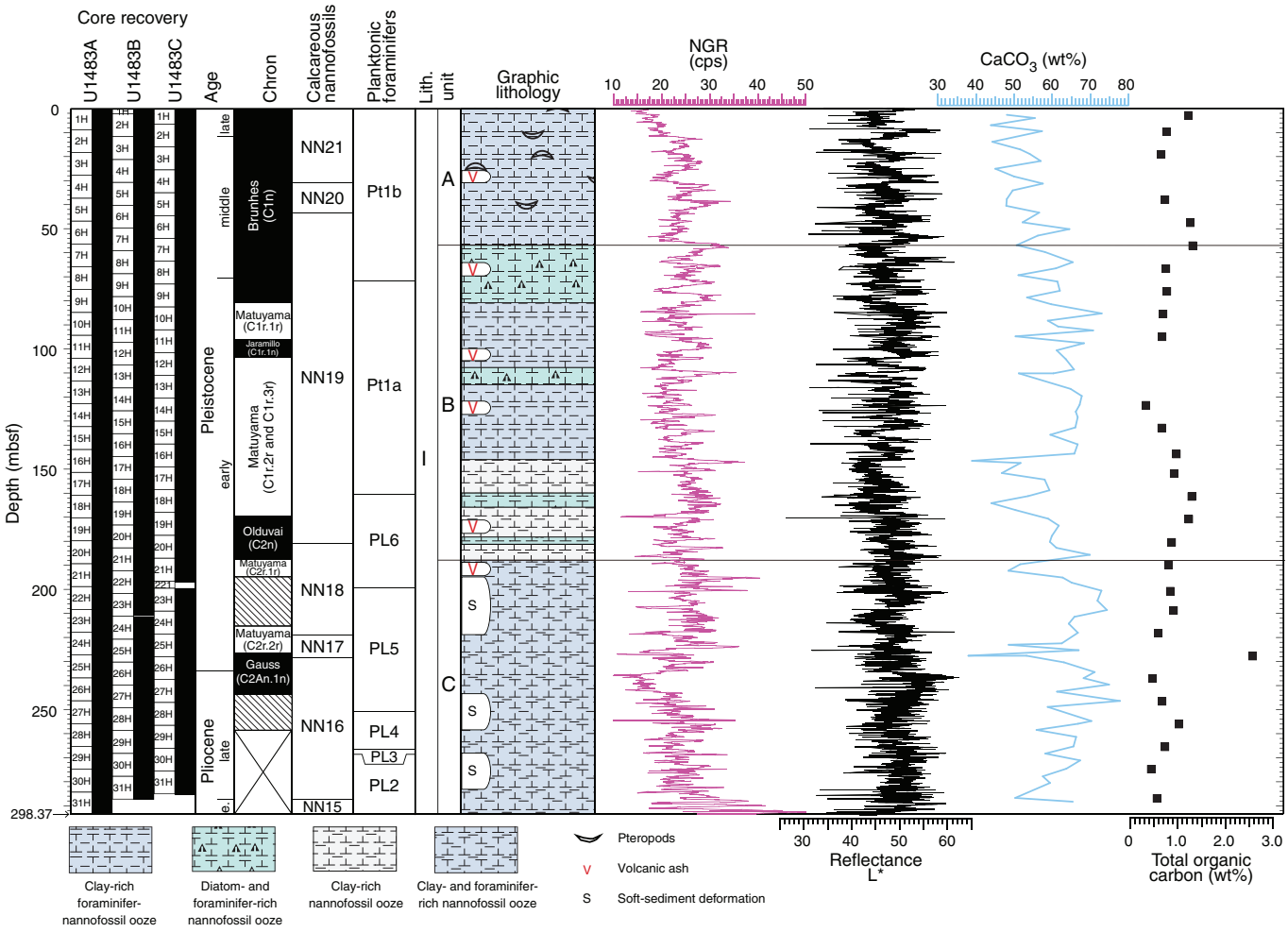

are restricted to the upper 40 mbsf. Meter-scale alternations between dark greenish gray and light greenish gray sediment are apparent and also recorded in NGR and L* records. The boundary between Subunits IA and IB is defined by the first downhole appearance of brownish gray diatom-rich nannofossil ooze. Subunit IB (early to middle Pleistocene) is an ~130 m thick sequence of greenish gray clay-rich nannofossil ooze, diatom-rich nannofossil clay, and clay-rich diatom-nannofossil ooze. This subunit is distinguished by higher biosiliceous content than that in Subunit IA. Clay content increases toward the bottom of Subunit IB. Color alternations are at the section scale (~1.5 m). The darker colored intervals have higher siliceous microfossil and organic matter content than the lighter colored intervals. Shell fragments are also common throughout this subunit. The boundary between Subunits IB and IC is denoted by a significant reduction in the abundance of siliceous microfossils. Subunit IC is composed of ~105 m of greenish gray foraminifer-rich nannofossil clay. Two significant intervals of soft-sediment deformation occur in this subunit (Figure **F10**). The upper unit is ~24 m thick, whereas the lower unit has varying thicknesses among the holes. These intervals include inclined bedding, folding, and microfaulting. Dark gray clay layers that exhibit high bulk density also occur in the deformed intervals.

The 293 m succession recovered at Site U1483 contains abundant, diverse, tropical calcareous nannofossil and planktonic foraminifer assemblages. Planktonic foraminifers dominate the >63 µm size fraction; however, other microfossil groups are also present and include benthic foraminifers, diatoms, radiolarians, silicoflagellates, and occasionally ostracods. The planktonic/benthic foraminifer ratios are typically 99:1. Preservation is generally excellent to very good throughout the entire succession, although a minor decrease in preservation is noted with depth.

Integrated calcareous nannofossil and planktonic foraminifer biostratigraphy, together with magnetostratigraphy, indicates that the succession at Site U1483 spans the late early Pliocene to the recent (Figure **F11**). Calcareous nannofossil and planktonic foraminifer biohorizons are generally in good agreement. The age at the bottom of the recovered succession is >3.59 Ma based on the presence of *Sphaeroidinella seminulina*. Biostratigraphy in the lowermost part of the recovered section (~293–260 mbsf) suggests sedimentation rates of ~10 cm/ky during the late early Pliocene. The interval between ~260 and 193.5 mbsf includes two packages of disturbed sediment. A clustering of biohorizons around 260–243 mbsf coincides with the deeper disturbed interval and is overlain by what appears to be intact stratigraphy, with another interval of clustered biohorizons from ~200 to 193 mbsf. Based on the mixed fossil assemblages found in the two intervals, these clusters could represent the top and base of a single, large mass movement dated to ~2.1 Ma or two (or more) discrete events dated to ~2.8 and 2.1 Ma.

Figure F11. Age-depth plot for Site U1483 showing integrated biomagnetochronology for Hole U1483A. Average sedimentation rates were ~10 cm/ky during deposition of the entire sequence. Two disturbed intervals were observed (gray boxes). These disturbed intervals are associated with intervals of mixed PF assemblages, calcareous nannofossil reworking, and intervals of lithologic disturbance.

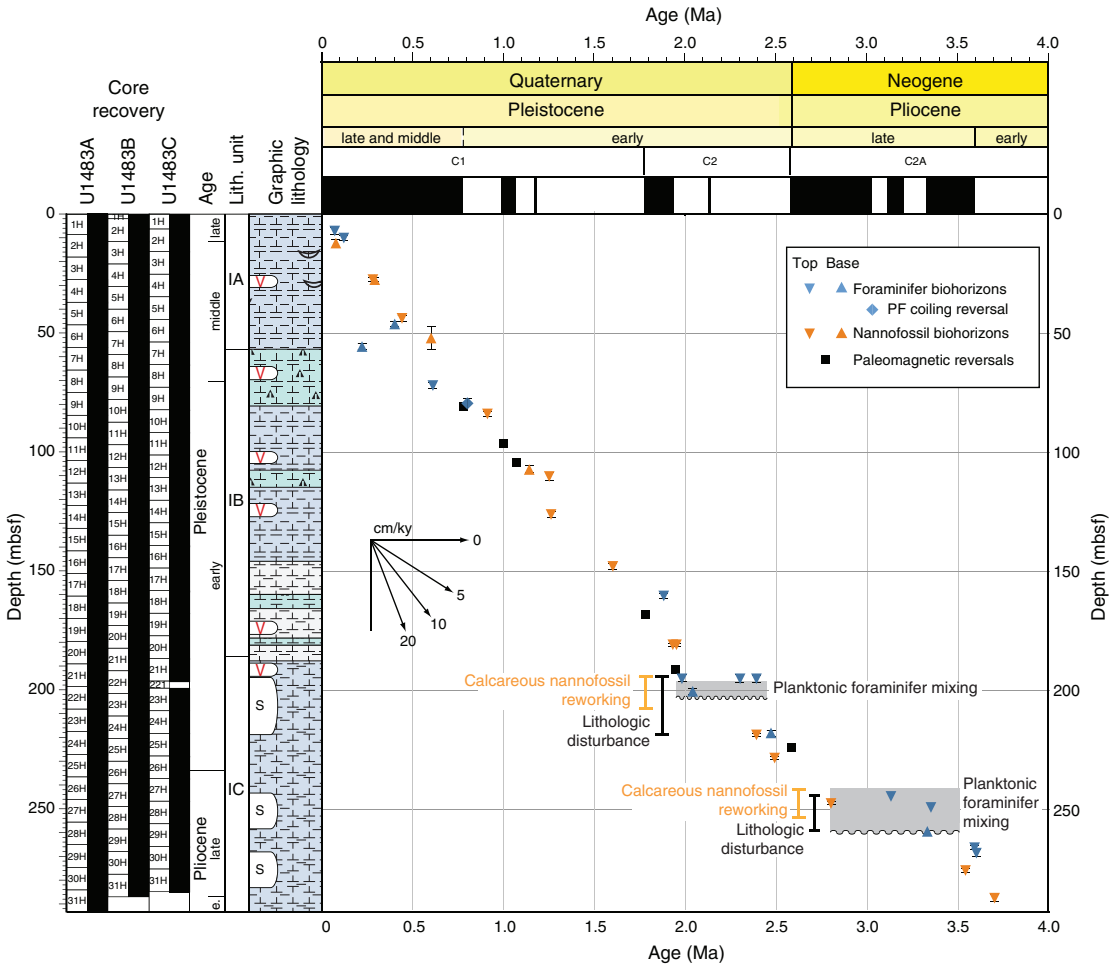

Above the disturbed interval, sedimentation rates were essentially constant at ~10 cm/ky from 2 Ma to present.

Paleomagnetic investigations at Site U1483 involved measurement of the NRM of all archive halves before and after demagnetization in a peak AF of 15 mT. Sixty-two 7 cm^3 discrete samples were taken to investigate paleomagnetic carriers and rock magnetic properties. NRM_{15mT} intensity is higher in the upper ~75 mbsf of each hole, decreases between 75 and 85 mbsf, and remains low and variable deeper than ~85 mbsf, occasionally approaching the measurement noise level of the magnetometer. Decreases in NRM intensity deeper than ~75 mbsf and reductions in the NRM_{15mT}/NRM intensity ratios are coeval with a decrease in interstitial water sulfate to almost zero and with peak methane concentrations, indicating that sediment diagenesis is likely influencing the magnetic mineralogy deeper than ~75 mbsf, although rock magnetic properties suggest that these effects may not be as severe as those experienced at Site U1482. For Holes U1483A and U1483B, azimuthally corrected declination is internally consistent between adjacent cores, although it maintains an ~180° baseline offset in absolute values because declination should cluster around 0° during periods of normal polarity. In Hole U1483C, negative inclination (expected for normal polarity in this Southern Hemisphere location) in the upper part of Hole U1483C is associated with declinations that cluster around 0°/360°. These orientations suggest that the declination offset observed in Holes U1483A and U1483B appears to have self-corrected in Hole U1483C; however, the cause of this self-correction remains unclear.

NRM directions are interpreted for the intervals not affected by soft-sediment deformation. The Matuyama/Brunhes boundary (0.781 Ma) is identified at ~80 mbsf. Below this depth we observe the upper (~93 mbsf; 0.988 Ma) and lower (~100 mbsf; 1.072 Ma) boundaries of the Jaramillo normal and the upper (~170 mbsf; 1.778 Ma) and lower (~186 mbsf; 1.945 Ma) boundaries of the Olduvai normal, with the lower Olduvai occurring a few meters above the upper interval of soft-sediment deformation (Figure **F10**). Guided by biostratigraphy, we also identify the Gauss/Matuyama boundary (~223 mbsf; 2.581 Ma) between the packages of soft-sediment deformation. These reversal horizons are in excellent agreement with both the calcareous nannofossil and planktonic foraminifer biohorizons (Figure **F11**).

The physical property data collected for Site U1483 include *P*-wave velocity, GRA bulk density, magnetic susceptibility, NGR, and thermal conductivity measurements on whole-round cores from all holes and *P*-wave velocity, porosity, and bulk, dry, and grain density measurements on split cores or discrete samples. Despite the relatively homogeneous lithology at Site U1483, physical property pa-

rameters display long-term trends and high-resolution variability throughout the recovered succession. Thermal conductivity, GRA bulk density, MAD dry and bulk densities, and porosity are all dominated by a long-term trend of increasing compaction with depth. Subtle changes in GRA bulk density underlying the compaction trend generally correspond with the lithologic subunits and are likely related to changes in clay content. Strong peaks in magnetic susceptibility are found coeval with the occurrence of some of the tephra layers in multiple holes. Otherwise, magnetic susceptibility and NGR are relatively stable throughout the record (Figure **F10**), unlike the broad long-term trends observed at Site U1482. The two intervals of observed soft-sediment deformation are coincident with elevated GRA and MAD bulk density values observed at ~195–218 and ~243–253 mbsf.

Tie points between holes at Site U1483 were established mainly with WRMSL magnetic susceptibility data, although some were based primarily on color reflectance L* data. In addition, we used WRMSL GRA bulk density and NGR data to aid correlations. We constructed two spliced intervals, one from 0 to 211.5 m CCSF and the other from 239.8 to 266.8 m CCSF. We did not construct splices over the two intervals of soft-sediment deformation (211.5–239.8 and deeper than 266.8 m CCSF) because WRMSL GRA bulk density and magnetic susceptibility data variations indicate that there is not stratigraphic continuity between holes over these intervals. However, we did estimate offsets for the cores within the deformed intervals because there were some features that could be correlated between holes.

A total of 36 interstitial water samples (35 whole-round samples and 1 mudline sample) were analyzed from Hole U1483A from the seafloor to 283.3 mbsf. The interstitial water profiles reflect early diagenetic processes related to organic matter degradation within the sediment, with downhole TOC contents ranging from 0.4 to 1.4 wt% (Figure **F10**). The oxic–suboxic transition at Site U1483 occurs at ~7.5 mbsf, indicated by a rapid increase in dissolved Mn concentration. The SMTZ observed at ~50 mbsf is characterized by quantitative consumption of dissolved SO_4 and increases in pH (from 7.7 to 8.4), alkalinity (up to ~18 mM), and PO_4 (25 µM). Dissolved Ca decreases to 4 mM at the SMTZ, suggesting active carbonate precipitation at this horizon. Mg/Ca and Sr/Ca ratios suggest that calcite (and not high-Mg calcite and/or dolomite) is most likely the dominant authigenic phase at the SMTZ. In addition, the rapid increase in the Ba profile at the SMTZ below 45 mbsf is suggestive of barite dissolution at the SMTZ. In the methanogenic zone below 50 mbsf, methane concentration increases to ~100,000 ppmv at 140 mbsf and then decreases to ~11,200 ppmv at the bottom of Hole U1483A. High methane/ethane ratios suggest that the methane is mostly of biogenic origin.

Downhole K, Mg, Li, Cl, and sodium (Na) concentrations reflect a combination of clay-mineral authigenesis/alteration and interstitial water diffusion. In particular, increasing trends in the Cl and Na profiles possibly reflect an upward diffusion from higher salinity fluids below the recovered sedimentary sequence. Changes in Si, Ca, NH_4, alkalinity, and Li were observed at the depths of deformed sediment intervals in Hole U1483A, suggesting that denser clay layers associated with the deformed sediments are influencing reaction/diffusion rates within, below, and/or above the deformed layers. $CaCO_3$ content ranges between 38 and 78 wt% (average = 59 wt%), showing a general increasing trend downhole in lithologic Subunits IA and IB (Figure **F10**). The interstitial Si concentration is also elevated here relative to Site U1482, and the presence of diatoms and radiolarians indicates the importance of biogenic silica at this site.

Site U1484

Background and objectives

Site U1484 (proposed Site WP-71A) is located ~15 km off the northern coast of Papua New Guinea at 03°07.93′S, 142°46.98′E in 1031 m water depth (Figure **F12**). The site is situated on seismic Line RR1313-WP7-2 (Rosenthal et al., 2016), ~900 m southwest of the crosspoint with seismic Line RR1313-WP7-5 and ~1.5 km east of the location of piston Core RR1313 PC32. The ~7 m piston core and a companion gravity core from this site are characterized by a mixture of clay and volcanic sand with relatively high numbers of planktonic and benthic foraminifers in excellent state of preservation. Preliminary isotope analysis of planktonic foraminifers from the cores indicates >6 m of Holocene sediment, implying sedimentation rates >60 cm/ky. The multichannel seismic (MCS) survey shows >650 m sediment coverage at this site. The MCS profiles ex-

Figure F12. Northern margin of Papua New Guinea (red box in Figure F3) showing the location of Sites U1484–U1487 (yellow circles). Sites U1484 and U1485 are located ~15 and ~19 km offshore Papua New Guinea, respectively. Contour interval = 500 m. Data source: Amante and Eakins (2009).

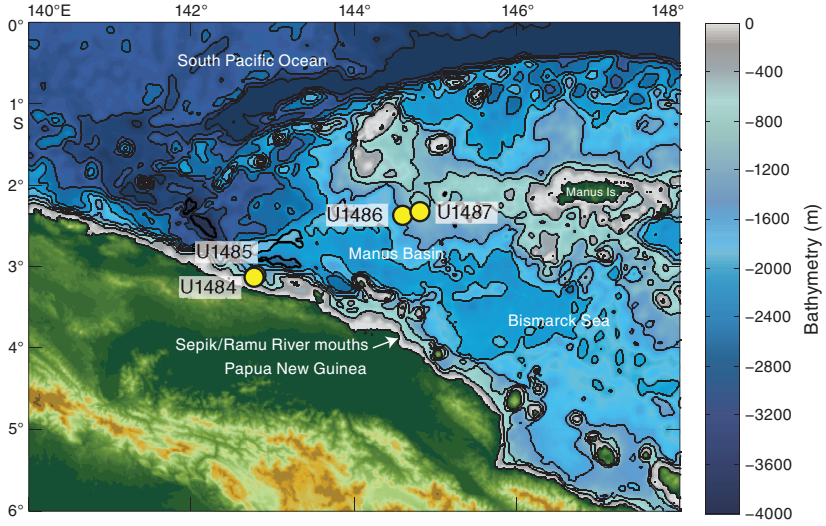

hibit remarkable uniformity of acoustic stratification, indicating a succession of alternating clay-, silt-, and sand-dominated beds down to 0.28 s TWT below the surface with an estimated depth of 225 mbsf, our target drilling depth. Below this depth, the MCS profiles suggest a disturbed zone. We also note a possible disturbed interval between 0.14 and 0.16 s TWT below the seafloor (Rosenthal et al., 2016).

Site U1484 is located in a tectonically complex region east of the Cyclops Mountains and west of the Sepik/Ramu River mouths. The region is bounded to the south by the Bewani-Torricelli fault zone on land, which links to offshore transform faults that eventually connect with a seafloor spreading zone(?) along the Bismarck Sea seismic lineation to the east (Baldwin et al., 2012). Northwest of the site, the southward subduction of the Caroline microplate forms the New Guinea Trench. The continental shelf in this region is exceedingly narrow (<2 km), allowing large amounts of terrigenous sediment discharge from coastal rivers to bypass the narrow continental shelf and accumulate in deeper water (Milliman et al., 1999).

The climatology and oceanography of northern Papua New Guinea is strongly influenced by the seasonal migration of the ITCZ, with enhanced precipitation during boreal winter (Figure **F2A, F2B**). Interannually, precipitation decreases during El Niño events (Figure **F2C, F2D**). Monsoon winds control the surface hydrography of the region such that the NGCC flows westward over the drill sites during the boreal summer southeasterly monsoon (also referred to as the austral summer monsoon in the Southern Hemisphere) (Kuroda, 2000). These currents distribute sediments originating from the Sepik/Ramu River mouths and multitudes of other tributaries along the coast over the northern slopes of Papua New Guinea and adjacent deep basins. The surface current reverses during the boreal winter northwesterly monsoon (Kuroda, 2000), and the surface sediment plume from the Sepik/Ramu River mouths is observed to meander out across the Bismarck Sea (Steinberg et al., 2006). In contrast, the NGCU persists in a westward direction year round at a water depth of ~220 m, widening and strengthening during boreal summer (Kuroda, 2000). This undercurrent supplies terrigenous sediments from the near-bottom river plumes to the drill sites. At ~1000 mbsl, the sediment is bathed in AIW.

The high sedimentation rate at Site U1484 provides the potential to resolve late middle to late Pleistocene centennial- to millennial-scale climate variability in the WPWP. Comparing these high-resolution records with comparable ones for the North Atlantic and eastern equatorial Pacific will allow us to better constrain the mechanisms influencing millennial-scale variability. This site will also provide insights on orbital-scale variability during the late middle to late Pleistocene. Finally, Site U1484 will allow us to examine the southern Pacific contribution to the ITF.

Operations

After a 2097 nmi transit from Site U1483, which was completed in 7.5 days at an average speed of 11.6 kt, the vessel stabilized over Site U1484 at 2245 h on 6 November 2016. We cored three holes at Site U1484 in accordance with the original operations plan that included coring with the APC system to 225 mbsf in three holes (Table **T1**).

Hole U1484A was cored to 195.0 mbsf with the APC system using core orientation and nonmagnetic hardware (Cores 363-U1484A-1H through 21H). We had poor recovery within an interval of sand from ~110 to 130 mbsf. After encountering APC refusal, we switched to the HLAPC system and continued coring to 223.2 mbsf (Cores 22F through 27F), where we terminated the hole. Downhole temperature measurements using the APCT-3 were taken on Cores 4H (37.1 mbsf), 7H (65.6 mbsf), 10H (94.1 mbsf), 13H (122.6 mbsf), and 16H (147.5 mbsf), and reliable results were obtained on three of the five deployments. A total of 220.60 m of sediment was recovered over 223.2 m of coring (99%) in Hole U1484A.

After encountering sand between ~110 and 130 mbsf in Hole U1484A, we altered the operations plan for the remaining holes to include using the HLAPC system over that interval to improve recovery. Hole U1484B was cored with the APC system using orientation and nonmagnetic hardware to 104.8 mbsf (Cores 363-U1484B-1H through 12H), including one 2 m drilled interval to offset core gaps for stratigraphic correlation. We then switched to the HLAPC system and continued coring to 133.0 mbsf (Cores 13F through 18F), which allowed us to better recover the sand found through that interval (recovery of 88% in Hole U1484B compared with 57% in Hole U1484A). We then switched back to the APC system and cored to 190 mbsf (Core 19H) using orientation. The remainder of Hole U1484B was cored with the HLAPC system to 222.9 mbsf (Cores 25F through 31F) after encountering APC refusal with Core 24H. We recovered 220.51 m of core over 220.9 m of coring (100% recovery) in Hole U1484B.

Oriented APC coring with nonmagnetic hardware continued in Hole U1484C to 106.1 mbsf (Cores 363-U1484C-1H through 12H). We then switched to the HLAPC system and cored to 145.7 mbsf (Cores 13F through 21F) to recover the sand interval. One drilled interval (2 m) advanced the hole without coring to avoid alignment of core gaps for stratigraphic correlation. We then switched back to the APC system and cored to 193.2 mbsf (Cores 22H through 26H). After encountering APC refusal, we finished coring the hole to 221.4 mbsf (Cores 27F through 32F) using the HLAPC. A total of 225.46 m of core was recovered over 219.4 m of coring (103%). Operations at Site U1484 ended at 0945 h on 10 November. Total time spent at the site was 83.0 h (3.5 days).

A total of 55 APC cores were recovered at this site, collecting 515.91 m of sediment over 508.4 m of penetration (101.5%). We also collected 33 HLAPC cores, recovering 150.66 m of sediment over 155.1 m of penetration (97.1%). Overall recovery at Site U1484 was 666.57 m of sediment over 663.5 m of coring (100.5%).

Principal results

The sediment cored at Site U1484 is assigned to a single lithologic unit composed of ~224 m of middle Pleistocene to recent terrigenous and hemipelagic sediment (Figure **F13**). Lithologic Unit I is composed of three main components: dark greenish gray clay, silt, and sand. The relative abundances of clay and silt vary downhole. Subordinate amounts of nannofossils and foraminifers are mixed with the terrigenous sediment, and fine-grained intervals alternate with discrete layers of sand- and silt-sized sediment. The upper ~10 mbsf is characterized by decimeter- to meter-thick clay layers with variable amounts of silt and a few thin (centimeter to decimeter) sand layers. From ~10 to 150 mbsf, the abundance and thickness of sand layers increases downhole. Clay is more abundant between ~150 and 175 mbsf, whereas in the deepest part of the succession, sand and clay layers are present in subequal proportions. The amount of clay and nannofossils in the sand layers is negligible; however, large benthic foraminifers are present within some of the coarser sand layers. Sulfide patches and sponge spicules are found in clay-rich intervals, whereas wood and shell fragments are more common in sand layers. The sand layers typically have sharp bases and show both normal and reverse grading. The sand-sized material at Site U1484 consists of four main components: minerals (feldspar,

Figure F13. Site U1484 results summary. cps = counts per second.

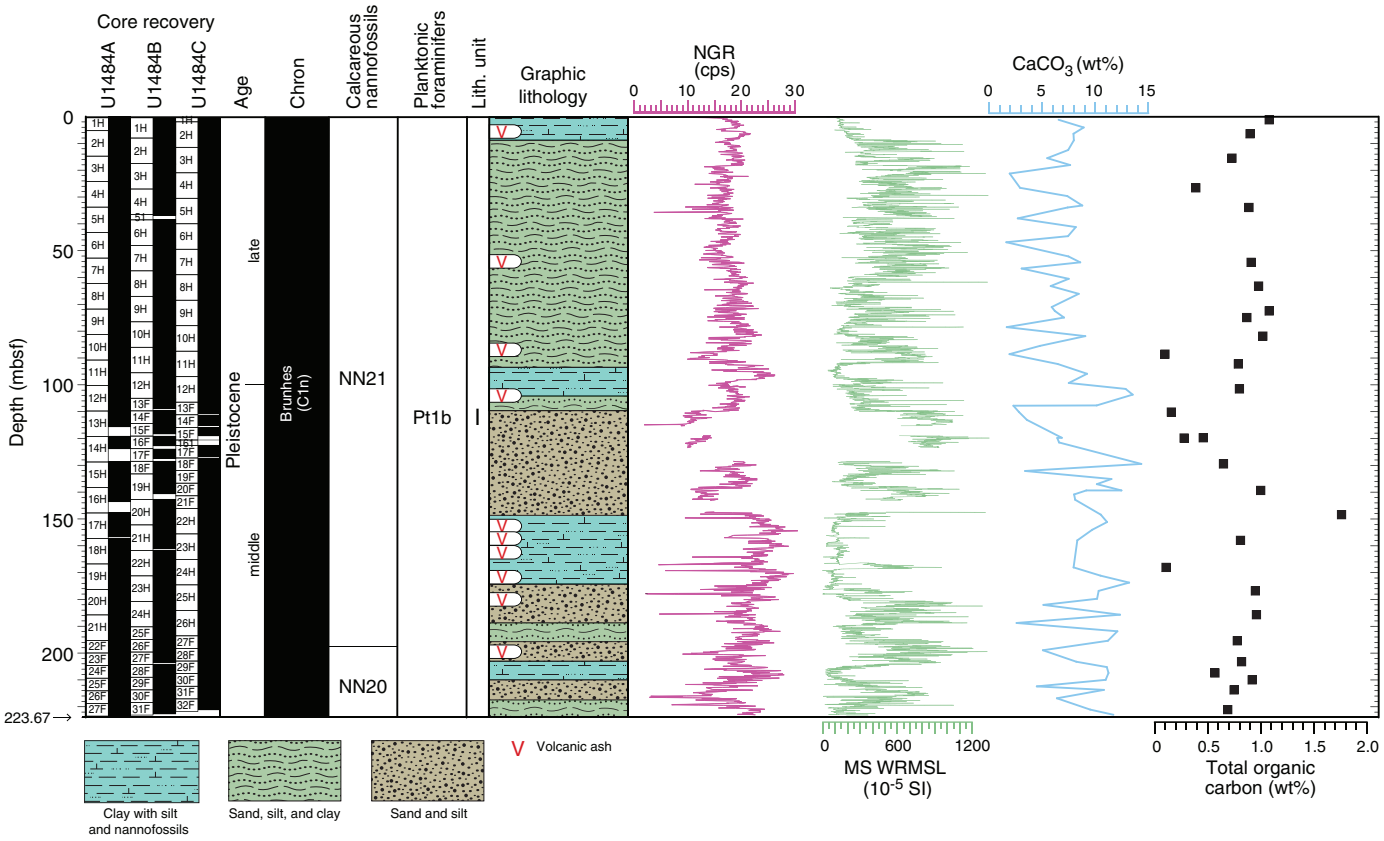

pyroxene, amphibole, and chlorite), volcanic and plutonic rock fragments, mineraloids (pyritized glauconite), and biogenic particles (foraminifers). Several discrete tephra layers up to 5 cm thick are present in the succession.

The sediment succession at Site U1484 contains well-preserved calcareous nannofossils, planktonic foraminifers, and benthic foraminifers. Calcareous nannofossils are not as abundant as they are at Sites U1482 and U1483, but benthic foraminifers are more common, with planktonic/benthic foraminifer ratios reaching 70:30 between ~60 and 150 mbsf. The benthic foraminifer assemblages change downhole. Deeper water species are present in the upper and lower parts of the succession, whereas the middle sections include mixed deeper and shallow-water benthic foraminifers, including some reef-dwelling forms.

Calcareous nannofossil and planktonic foraminifer biostratigraphy indicates that Hole U1484A spans the late middle Pleistocene to recent (Figure **F14**). The upper ~200 mbsf of the succession is within Zone NN21 (late middle Pleistocene to recent), identified by the biohorizon base *E. huxleyi* (0.29 Ma) between ~195 and 200 mbsf. The absence of *G. tosaensis* (the marker for Subzone Pt1a) assigns the entire section recovered at Hole U1484A to Subzone Pt1b (<0.61 Ma), and the absence of *Pseudoemiliania lacunosa* indicates that the base of the succession is within Zone NN20 (0.44–0.29 Ma) (Figure **F13**). The middle/late Pleistocene boundary (0.126 Ma) is located between the biohorizons top acme *Gephyrocapsa caribbeanica* (0.28 Ma) and top *G. ruber* (pink) (0.12 Ma) at ~100 mbsf. Average estimated linear sedimentation rates based on calcareous nannofossil and planktonic foraminifer bioevents were ~75 cm/ky (Figure **F14**).

Paleomagnetic investigations at Site U1484 involved measuring the NRM of archive halves from all holes before and after demagnetization in a peak AF of 10–15 mT. Forty-seven 7 cm^3 discrete samples were taken to investigate paleomagnetic carriers and rock magnetic properties. Discrete magnetic susceptibility, IRM, and IRM ratios indicate relatively high ferrimagnetic mineral concentrations, and despite observations of pyrite in the lower part of the three holes, sediment diagenesis has had relatively little effect on the primary magnetic assemblage.

Sediment in all three holes appears to have been deposited (quasi-)continuously with no major hiatuses. Azimuthally corrected declination from APC cores in all holes is internally consistent between adjacent cores, although it maintains an ~180° baseline offset in absolute values because declination should cluster around 0° during periods of normal polarity. Inclination plots around, or slightly steeper than (owing to a pervasive overprint), expected values of about −6° for the site latitude assuming a GAD field. These observations are consistent with all the sediment recovered at Site U1484 being deposited during the Brunhes (C1n), <0.781 Ma (Figure **F13**). These findings are consistent with biostratigraphic datums that suggest that the sediment at the base of Site U1484 is between 0.29 and 0.44 Ma in age.

Physical properties, including short-term, decimeter-scale variability, correlate well with the alternating clay and silty sand lithologies found at Site U1484. Because of the high sedimentation rates, the effect of increased compaction with depth is only minor at this site. GRA bulk density increases rapidly from 1.5 to 1.75 g/cm^3 from the seafloor to ~12 mbsf and then gradually increases to ~1.8 g/cm^3 at the bottom of the hole. GRA bulk density probably underesti-

Figure F14. Age-depth plot for calcareous nannofossil and planktonic foraminifer biohorizons, Site U1484. Dashed line shows the mean long-term sedimentation rate. The age at the bottom of Hole U1484A is estimated to be 0.29 Ma based on the average linear sedimentation rate of 75 cm/ky.

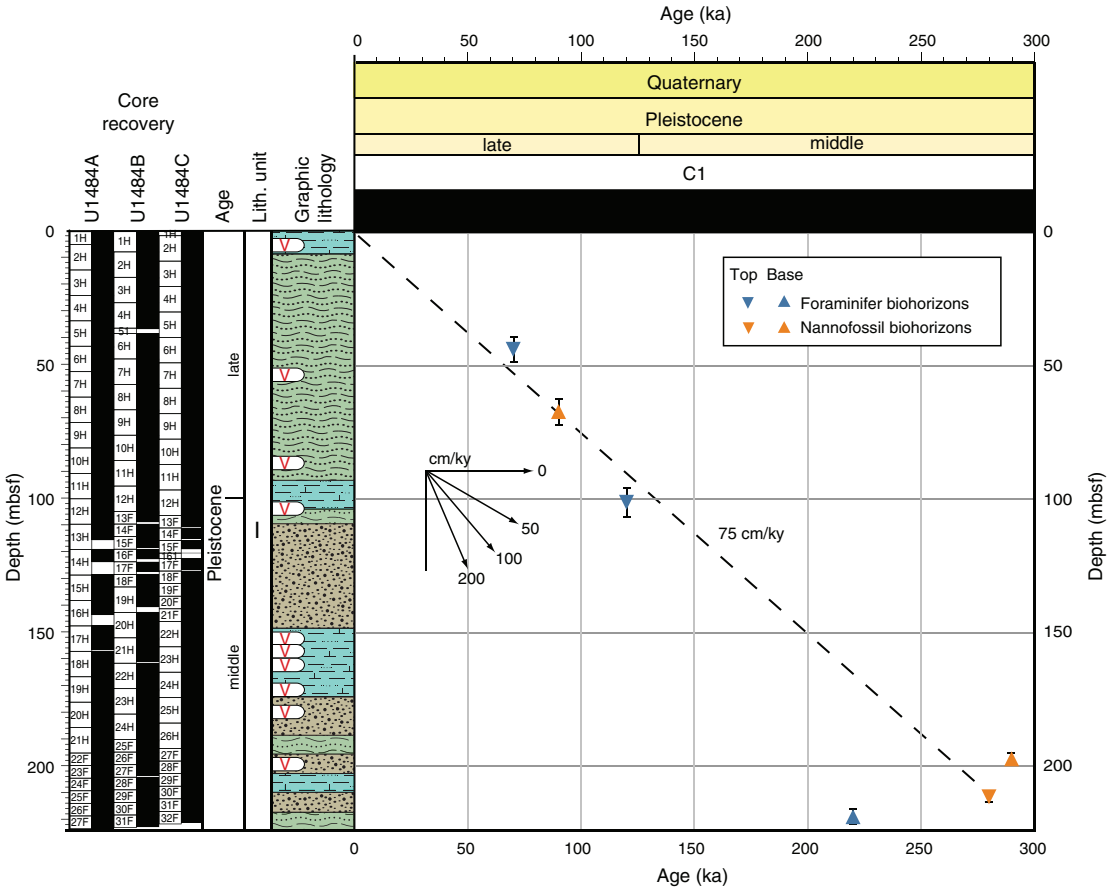

mates the true bulk density compared with discrete MAD bulk density, particularly in the sand layers. This underestimation may be due to significant gas-induced expansion in the sand-rich layers. The high bulk and grain densities additionally correspond to low carbonate content values (~2–3 wt%) and low TOC content (0.1–0.2 wt%) (Figure **F13**). Magnetic susceptibility ranges from 50×10^{-5} to $>1200 \times 10^{-5}$ SI, with lower values corresponding to clay-rich intervals. NGR counts range between ~10 and 30 counts/s, with lower values corresponding to sand intervals (Figure **F13**). In all holes, 12 distinct 10–15 m cycles are observed in GRA bulk density, NGR, and especially magnetic susceptibility, which broadly reflect alternations between clay-rich and silty sand-rich layers. Downhole temperature measurements made with the APCT-3 indicate a geothermal gradient of 40°C/km.

For Site U1484, we constructed a splice for the entire site using all three holes, but there are gaps in the splice mainly because of incomplete recovery of sand intervals. Gas expansion frequently caused extrusion of sediment out of the top and bottom of the core liner and onto the rig floor, resulting in disturbed sediment, especially in the top and bottom sections of each core, as well as voids throughout the recovered sequence. These factors resulted in relatively high growth factors and made it difficult to correlate data between holes. Tie points were established mainly with WRMSL magnetic susceptibility data supplemented with NGR data. The splice is continuous from 0 to 133.98 m CCSF. Below this depth, from 133.98 to 153.85 m CCSF, there are at least three core gaps and some tentative tie points. This interval is underlain by an interval from 153.85 to 270.85 m CCSF that is continuous except for one core gap at 172.55–175.28 m CCSF. The deepest interval, from 270.85 to 284.61 m CCSF, has a few core gaps. In sum, although there were some intervals with discontinuous recovery, we calculated offsets for all cores in all three holes and constructed a nearly continuous splice that has a few gaps.

A total of 24 interstitial water samples (23 whole-round samples and 1 mudline sample) were analyzed from Hole U1484A from the seafloor to 222.4 mbsf. The interstitial water geochemistry reflects early diagenetic processes driven by remineralization of organic matter. The TOC content ranges between ~0.1 and 1.8 wt% (average = 0.88 wt%) (Figure **F13**). The TOC/total nitrogen (TN) ratios in most samples are <10, suggesting that organic matter deposited at Site U1484 is largely of marine origin. Correlations between the downhole profiles of TOC and TN contents suggest that the majority of the nitrogen is organic-bound, with little preferential degradation between organic carbon and nitrogen; however, caution should be taken when interpreting the TOC and C/N records because shipboard TOC values are calculated by the subtraction method. Carbonate content at this site is low, ranging from ~2 to 15 wt% (Figure **F13**).

Rapid progression through suboxic and anoxic organic matter remineralization in the upper portion of the sediment is indicated by enrichments of dissolved Mn and Fe at ~3 mbsf and an abrupt increase in methane and near-complete depletion of dissolved SO_4 (the SMTZ) at ~20 mbsf. The dissolved Ca concentration at the SMTZ is relatively low (~2 mM), suggesting that active carbonate precipitation takes place at this depth, possibly as authigenic aragonite, as supported by a concomitant drop in Sr concentration. Below

the SMTZ, hydrocarbon gas is characterized by very high methane/ethane ratios, which suggests that the methane is mostly of biogenic origin.

A striking feature of interstitial water geochemistry at Site U1484 is the large increase of alkalinity (up to 50 mM) from the seafloor to between ~40 and 50 mbsf. This alkalinity peak is accompanied by enrichments in dissolved Mg, K, and Na, suggesting partial dissolution of silicate minerals occurred within this interval. At Site U1484, this process, termed anoxic silicate weathering (Wallmann et al., 2008), is most likely driven by the presence of substantial amounts of easily alterable fresh volcanogenic material derived from the nearby Papua New Guinea highlands. This process typically represents a net sink for carbon dioxide in methanogenic sediment, which releases HCO_3^-, dissolved cations, and Si into the interstitial water. It may also lead to formation of secondary clay minerals (e.g., smectite) in the sediment, which at Site U1484 could possibly explain some of the observed decrease of dissolved Mg deeper than 50 mbsf. The comparatively low dissolved Fe concentration throughout Hole U1484A (except for the upper 10 mbsf) may be explained by significant formation of pyrite within the sediment column.

Site U1485

Background and objectives

Site U1485 (proposed Site WP-72A) is located ~19 km off the northern coast of Papua New Guinea at 03°06.16′S, 142°47.59′E in 1145 m water depth (Figure **F12**). The site is situated on seismic Line RR1313-WP7-2, ~2 km northeast of the cross point with seismic Line RR1313-WP7-5 (Rosenthal et al., 2016) and ~3.2 km north-northeast of Site U1484. An ~7 m piston core and a companion gravity core retrieved ~4 km to the southwest of the site location are characterized by a mixture of clay and volcanic sand with relatively high numbers of planktonic and benthic foraminifers in excellent state of preservation. Preliminary isotope analysis of planktonic foraminifers from the cores indicates >6 m of Holocene sediment, implying sedimentation rates >60 cm/ky. The multichannel seismic profiles exhibit remarkable uniformity of acoustic stratification indicating a succession of alternating clay-, silt-, and sand-dominated beds down to 0.4 s TWT below the seafloor surface, with an estimated depth of 350 mbsf, just deeper than our target drilling depth of 325 mbsf. There is evidence for a disturbed layer between 0.16 and 0.19 s TWT, but bedding is very uniform below this interval to the target depth (Rosenthal et al., 2016). This site extends the record recovered at Site U1484.

Site U1485 is located in a tectonically complex region east of the Cyclops Mountains and west of the Sepik/Ramu River mouths. The region is bounded to the south by the Bewani-Torricelli fault zone on land, which links to offshore transform faults that eventually connect with a zone of seafloor spreading along the Bismarck Sea seismic lineation to the east (Baldwin et al., 2012). Northwest of the site, the southward subduction of the Caroline microplate forms the New Guinea Trench. The continental shelf in this region is exceedingly narrow (<2 km), allowing large amounts of terrigenous sediment discharge from coastal rivers to bypass the narrow continental shelf and accumulate in deeper water (Milliman et al., 1999).

The climatology and oceanography of northern Papua New Guinea is strongly influenced by the seasonal migration of the ITCZ, with enhanced precipitation during boreal winter (Figure **F2A, F2B**). Interannually, precipitation decreases during El Niño events (Figure **F2C, F2D**). Monsoon winds control the surface hydrography of the region, such that the NGCC flows westward over the drill sites during the boreal summer southeasterly monsoon (also referred to as the austral summer monsoon in the Southern Hemisphere) (Kuroda, 2000). These currents distribute sediments originating from the Sepik/Ramu River mouths and multitudes of other tributaries along the coast over the northern slopes of Papua New Guinea and adjacent deep basins. The surface current reverses during the boreal winter northwesterly monsoon (Kuroda, 2000), and the surface sediment plume from the Sepik/Ramu River mouths is observed to meander out across the Bismarck Sea (Steinberg et al., 2006). In contrast, the NGCU persists in a westward direction year round at a water depth of ~220 m, widening and strengthening during boreal summer (Kuroda, 2000). This undercurrent supplies terrigenous sediments from the near-bottom river plumes to the drill sites. At ~1000 mbsl, the sediment is bathed in AIW.

The high sedimentation rates at Site U1485 provide the potential to resolve late middle to late Pleistocene centennial- to millennial-scale climate variability in the WPWP. Comparing these high-resolution records with comparable ones for the North Atlantic and eastern equatorial Pacific will us to better constrain the mechanisms influencing millennial-scale variability. This site will also provide insights on orbital-scale variability during the late middle to late Pleistocene. Finally, Site U1485 will allow us to examine the southern Pacific contribution to the ITF.

Operations

After a 1.85 nmi transit in dynamic positioning mode from Site U1484, the vessel stabilized over Site U1485 on 10 November 2016. The original operations plan at Site U1485 included three holes using the APC and HLAPC to 315 mbsf. We ultimately cored four holes (Table **T1**). Holes U1485A and U1485B were cored to ~300 mbsf. Hole U1485C was terminated after three cores when it proved unsuitable for covering core gaps for stratigraphic correlation. Hole U1485D was cored to 63.9 mbsf to fill core gaps and intervals where significant numbers of interstitial water samples were taken from each core in Hole U1485A.

Hole U1485A was cored to 188.0 mbsf with the APC using orientation and nonmagnetic hardware (Cores 363-U1485A-1H through 20H). After pumping Core 20H out of the core barrel, we switched to the HLAPC and continued coring to 300.8 mbsf (Cores 21F through 44F), where we encountered a partial stroke, indicating HLAPC refusal. Because we had reached our age target, we decided not to deepen the hole further using the XCB coring system. As Site U1485 is located only ~3.2 km from Site U1484, we opted not to take downhole temperature measurements. Whole-round samples for high-resolution interstitial water analyses were taken at a frequency of one per section in the upper ~54 mbsf of Hole U1485A. A total of 312.36 m of sediment was recovered over 300.8 m of coring (104% recovery) in Hole U1485A.

Because core recovery was generally good in the upper 190 mbsf, we opted not to switch to the HLAPC over the interval with higher sand content that had resulted in poor recovery with the full-length APC at Site U1484. Hole U1485B was cored to 173.5 mbsf (Cores 363-U1485B-1H through 20H) using the APC with orientation and nonmagnetic hardware. We then switched to the HLAPC and continued coring to 297.7 mbsf (Cores 21F through 47F), with one 2 m drilled interval to offset core gaps for stratigraphic correlation. We recovered 291.18 m of core over 295.7 m of coring (98% recovery) in Hole U1485B.

Oriented APC coring with nonmagnetic hardware then continued in Hole U1485C; however, after data collected for stratigraphic correlation indicated that Core 363-U1485C-2H was a copy of Core 1H, we terminated the hole. Hole U1485C was cored to 27.5 mbsf (Cores 1H through 3H) and recovered 29.35 m of sediment (107%

Figure F15. Site U1485 results summary. cps = counts per second.

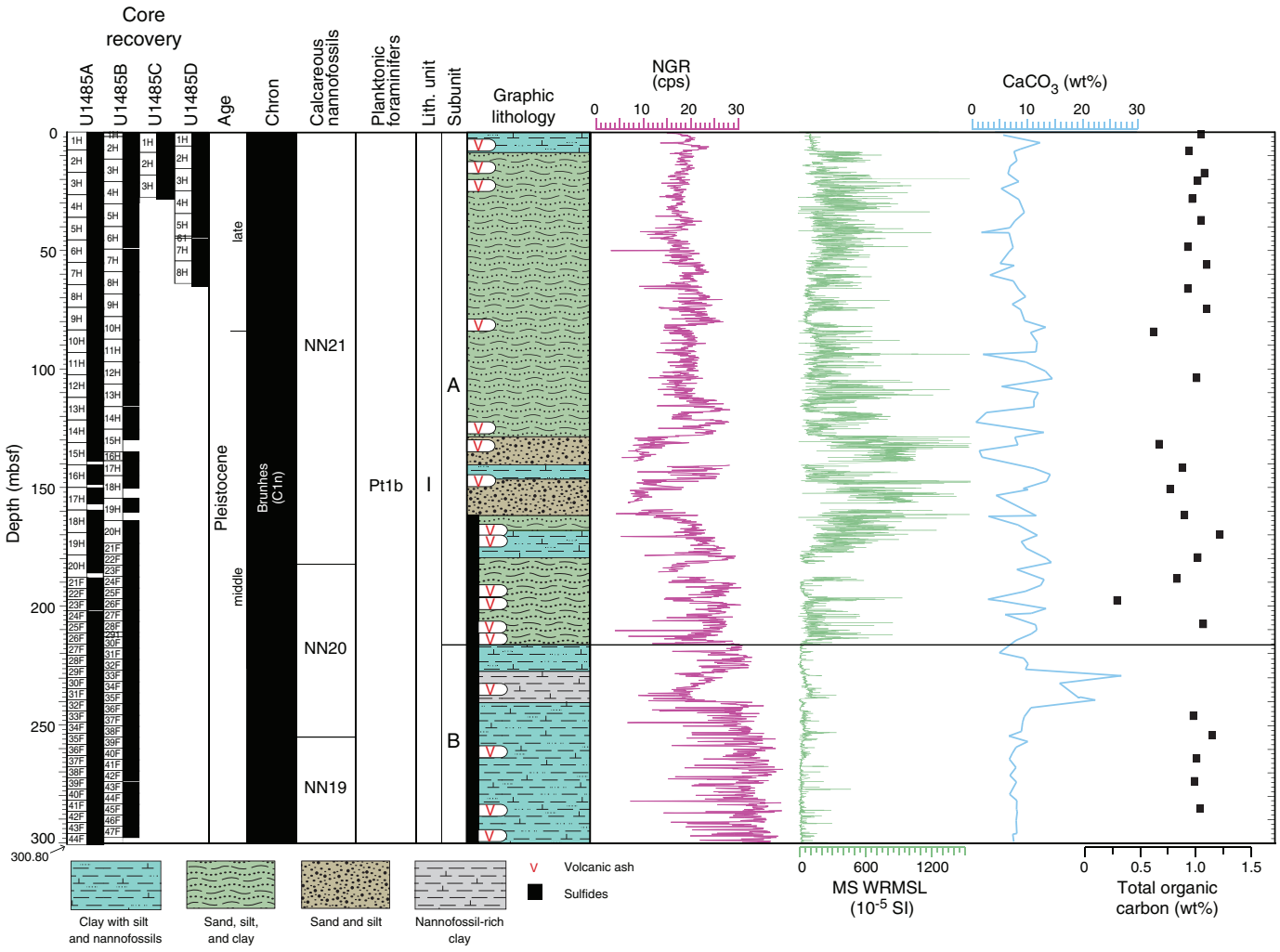

recovery). Hole U1485D was cored specifically to contribute material to the stratigraphic splice, particularly over the interval of high-resolution interstitial water sampling shallower than 55 mbsf. Oriented APC coring with nonmagnetic hardware penetrated to 63.9 mbsf (Cores 363-U1485D-1H through 8H), with one 1 m drilled interval to cover a core gap. A total of 68.22 m of core was collected over 62.9 m of coring (108% recovery). Operations at Site U1485 ended at 2330 h on 13 November. Total time spent at the site was 85.8 h (3.6 days).

A total of 50 APC cores were recovered at this site, collecting 452.28 m of sediment over 451.9 m of coring (100.1% recovery). We also collected 50 HLAPC cores, recovering 248.73 m of sediment over 235 m of coring (105.9% recovery). Total core collected at Site U1485 was 701.11 m of sediment over 686.9 m of coring (102.1% recovery).

Principal results

An ~300 m succession was recovered in four holes at Site U1485. The upper ~225 mbsf shares some similarities with the stratigraphy and lithologies observed at Site U1484, which is located only ~3.2 km south-southwest of the site. The sediment at Site U1485 is assigned to a single lithologic unit composed of ~300 m of middle Pleistocene to recent terrigenous and hemipelagic sediment (Figure **F15**). Lithologic Unit I is divided into two subunits. Subunit IA is an ~216 m sequence of middle Pleistocene to recent sediment composed of three main components (dark greenish gray clay, silt, and sand) that is equivalent to Unit I at Site U1484. The relative abundances of these terrigenous components vary downhole. Subordinate amounts of nannofossils and foraminifers are mixed with the terrigenous sediment, and fine-grained intervals alternate with discrete layers of sand- and silt-sized sediment. As at Site U1484, the upper ~8 mbsf is characterized by thick (decimeter to meter) clay layers with variable amounts of silt and several centimeter- to decimeter-thick sand layers. From ~8 to 127 mbsf, coarser grained material becomes more abundant, with the frequency and thickness of sand layers increasing downhole, although clay-rich intervals are still present over this interval. Two thick sand intervals occur between ~127 and 165 mbsf, separated by a 6 m thick interval of hemipelagic clay. From ~165 to 216 mbsf, the sediment consists of clay with variable amounts of silt and nannofossils, interbedded with thinner sand layers. Shallow-water benthic foraminifers are less frequent in the sand layers at this site compared to Site U1484, whereas shell and wood fragments are common. The sand layers typically have sharp bases and show both normal and reverse grading. The sand-size material at Site U1485 consists of four main components: minerals (feldspar, pyroxene, amphibole, and chlorite), volcanic and plutonic rock fragments, mineraloids (pyritized glauconite), and biogenic particles (foraminifers). Sulfide patches are also present,

Figure F16. Age-depth plot for calcareous nannofossil and planktonic foraminifer biohorizons, Site U1485. Dashed line shows the mean long-term sedimentation rate of ~62.5 cm/ky. The age at the bottom of Hole U1485A is constrained between 0.44 and 0.60 Ma and is estimated as >0.50 Ma based on the nannofossil evidence.

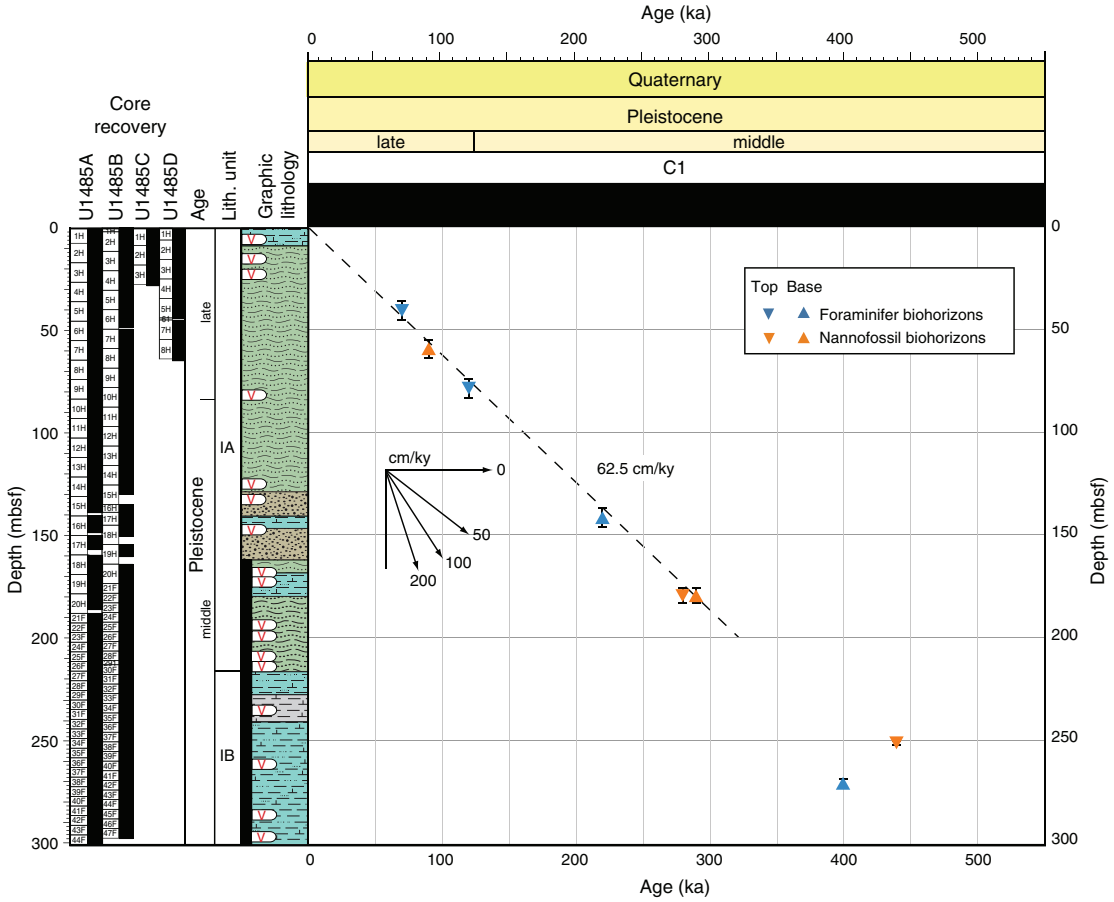

with pyrite occurring frequently deeper than ~165 mbsf. Subunit IB is an ~85 m succession dominated by dark gray clay with variable amounts of silt and nannofossils. The absence of coarse sand layers distinguishes this subunit from Subunit IA. A nannofossil-rich clay layer from ~226 to 240 mbsf has higher carbonate content than the rest of the succession (Figure **F15**). A number of discrete tephra layers up to 4 cm thick are present throughout the succession at Site U1485.

The succession at Site U1485 contains well-preserved calcareous nannofossils, planktonic foraminifers, and benthic foraminifers. The calcareous nannofossil and planktonic foraminifer assemblages are very similar to those at Site U1484; however, the benthic foraminifer assemblages show less influence from downslope transport. The planktonic/benthic foraminifer ratios are consistently around 99:1 (compared with 70:30 at Site U1484). Only a few intervals contain the shallow-water taxon *Rotalinoides compressiusculus*, whereas the bulk of the assemblage is dominated by typical bathyal forms.

Calcareous nannofossil and planktonic foraminifer biostratigraphy indicates that Hole U1485A spans the late middle Pleistocene to recent (Figure **F16**). The upper ~183 mbsf of the succession is within Zone NN21 (late middle to late Pleistocene), identified by the biohorizon base *E. huxleyi* (0.29 Ma) between ~179 and 186 mbsf. From ~183 to 255 mbsf, the sequence is assigned to Zone NN20 based on the absence of *E. huxleyi* and *P. lacunosa*. The biohorizon top *P. lacunosa* (0.44 Ma), found between ~254 and 257 mbsf, indicates the top of Zone NN19. The remainder of the cored succession to 300 mbsf is assigned to the upper part of Zone NN19 (middle Pleistocene). The absence of *G. tosaensis* (the marker for Subzone Pt1a) assigns the entire section recovered at Hole U1485A to Subzone Pt1b (<0.61 Ma) (Figure **F15**). Together, nannofossil and planktonic foraminifer biostratigraphy indicates an age between 0.61 and 0.44 Ma for the bottom of the succession at Hole U1485A. The middle/late Pleistocene boundary (0.126 Ma) is located between the biohorizons top acme *G. caribbeanica* (0.28 Ma) and top *G. ruber* (pink) (0.12 Ma) at ~84 mbsf. Sedimentation rates based on calcareous nannofossil and planktonic foraminifer bioevents were ~62.5 cm/ky (Figure **F16**).

Paleomagnetic investigations at Site U1485 involved measurement of the NRM of archive halves from all holes before and after demagnetization in a peak AF of 10 mT (Holes U1485A and U1485D) and 15 mT (Holes U1485B and U1485C). Sixty-three 7 cm^3 discrete samples were also taken to investigate paleomagnetic carriers and rock magnetic properties. Discrete magnetic susceptibility, IRM, and IRM ratios indicate relatively high ferrimagnetic mineral concentrations in sediment shallower than ~180 mbsf. Deeper than ~180 mbsf, magnetic susceptibility and IRM decrease to relatively low values, and ferrimagnetic grain size is distinctly coarser deeper than ~240 mbsf. This interval was not cored at Site U1484 and is coincident with the occurrence of extensive pyrite in the recovered sediment that may be related to alteration of the pri-

mary magnetic assemblage at depth (e.g., Karlin and Levi, 1983; Rowan et al., 2009).

Sediment in all three holes appears to have been deposited (quasi-)continuously with no major hiatuses. Azimuthally corrected declination is internally consistent between adjacent cores, although it maintains an ~180° baseline offset in absolute values because declination should cluster around 0° during periods of normal polarity. Corrected declination of Hole U1485A varies by ~30°–90° between adjacent cores. This between-core variability is not observed in the other holes at Site U1485, so it is likely these offsets result from incorrect correction from the Icefield MI-5 core orientation tool. The specific tool used (Icefield #2007) generated a similar issue at Hole U1483C, and we concluded this to be a tool-specific issue. This tool was not used for the remainder of the expedition. Inclination plots around or slightly steeper than (owing to a pervasive overprint) expected values of about –6° for the site latitude assuming a GAD field. These observations are consistent with all sediment recovered at Site U1485 being deposited during the Brunhes (C1n), <0.781 Ma (Figure **F15**). These findings are in agreement with biostratigraphic datums that suggest that the base of Site U1485 is between 0.61 and 0.44 Ma (Figure **F16**).

Physical properties correlate well with the alternating clay and silty sand lithologies at Site U1485 over both short and longer scales. Because of the high sedimentation rates, the effect of increased compaction with depth is minimal. GRA bulk density and magnetic susceptibility are particularly sensitive to variations in clay and sand content, recording high-frequency variations. GRA bulk density increases rapidly from 1.5 to 1.65 g/cm^3 between the seafloor and ~10 mbsf. From ~10 to 135 mbsf, GRA bulk density displays 10–15 m cycles with values ranging from 1.4 to 1.85 g/cm^3. Below 185 mbsf, variability in GRA bulk density decreases significantly, ranging between 1.35 and 1.5 g/cm^3, which reflects the dominance of clay. Over most of the record, GRA bulk density and magnetic susceptibility covary. Magnetic susceptibility is generally lower in clay-rich intervals and shows more variability and higher values in silt- and sand-rich intervals (Figure **F15**). Magnetic susceptibility values are consistently low from 0 to 10 mbsf (~150 × 10^{-5} SI). Below this, magnetic susceptibility shows 10–15 m scale cyclicity similar to the GRA bulk density record, with values ranging from 50 × 10^{-5} to >1200 × 10^{-5} SI. In the clay-rich Subunit IB, magnetic susceptibility is significantly lower and shows less variability, averaging ~100 × 10^{-5} SI. NGR counts range between ~10 and 40 counts/s, with the lower values corresponding to sand intervals (Figure **F15**). The NGR record also exhibits 10–15 m scale cyclicity, particularly in the interval from ~10 to 135 mbsf.

For Site U1485, we constructed a splice for the entire site using three holes (U1485A, U1485B, and U1485D), but there are gaps in the splice mainly because of incomplete recovery of sand intervals. Hole U1485C was not used for construction of the splice because the second core appears to repeat the section recovered in the first core, which resulted in termination of coring after only three cores. Gas expansion frequently caused extrusion of sediment out of the top and bottom of the core liner and onto the rig floor, resulting in disturbed sediment, especially in the top and bottom sections of each core, as well as voids throughout the recovered sequence. Tie points were established mainly with WRMSL magnetic susceptibility data supplemented with NGR data. The splice is continuous and well constrained from 0 to 157.41 m CCSF. Reduced core recovery in the relatively sand rich interval from 157.41 to 222.11 m CCSF and gaps aligned between HLAPC cores of adjacent holes from 222.11 to 267.34 m CCSF resulted in a discontinuous splice over this interval. From 267.34 m CCSF to the bottom of the cored section at 373.35 m CCSF, the splice is tentative due to voids caused by gas expansion, low-amplitude magnetic susceptibility values, and low-resolution NGR counts used to establish correlations.

A total of 60 whole-round samples and one mudline sample were collected from the seafloor to 295 mbsf in Hole U1485A. Thirty-six samples were analyzed on the ship, whereas the remaining samples were fixed for shore-based analyses. The interstitial water geochemical profiles at Site U1485 closely resemble those obtained at nearby Site U1484. Near-complete consumption of dissolved SO_4 was observed at ~12 mbsf, coincident with an abrupt increase of methane at the SMTZ. Below the SMTZ, most samples are characterized by high methane/ethane ratios, suggesting that the methane is mostly of biogenic origin. The TOC content at Site U1485 is slightly higher than at Site U1484, ranging from ~0.3 to 1.2 wt% (Figure **F15**). The TOC/TN ratios are usually <10, suggesting that the organic matter deposited at Site U1485 is largely of marine origin; however, caution should be taken when interpreting the TOC and C/N records because shipboard TOC values are calculated by the subtraction method.

As at Site U1484, Site U1485 displays evidence for anoxic silicate weathering occurring within the methanogenic zone, as inferred from marked enrichments of alkalinity (up to 50 mM), K (13.5 mM), and Mg (50 mM) between ~20 and 120 mbsf. Similarly, the carbonate content of Site U1485 is generally low, ranging from to 0.7 to 27.0 wt% with an average of 9.0 wt% (Figure **F15**). Penetration to deeper depths at Site U1485 (300 mbsf) than at Site U1484 (223 mbsf) provides more insights into the sediment-water interactions that occur deeper in the sedimentary sequence at the Papua New Guinea margin. A notable feature is the pronounced downhole depletion observed for several elements (Mg, K, B, and PO_4) along with decreases in alkalinity and pH from ~50 to 120 mbsf. In agreement with results from previous investigations (Michalopoulos and Aller, 1995; Wallmann et al., 2008; Kim et al., 2016), these findings are consistent with secondary clay authigenesis (reverse weathering), a process that releases CO and leads to removal of major cations/anions from interstitial water.

Finally, abrupt changes in concentration or slope are observed in interstitial water profiles of several elements (e.g., K, Mg, Na, Br, and PO_4) coincident with changes in lithology. These changes in lithology likely act as diffusive caps, interrupting communication in interstitial water between the sediment above and below these distinct lithologic changes, thereby imparting slight variations in concentration that overprint the general trends dominated by anoxic sediment weathering and clay mineral authigenesis.

Site U1486

Background and objectives

Site U1486 (proposed Site WP-05A) is located ~215 km west-southwest of Manus Island at 02°22.34′S, 144°36.08′E in 1332 m water depth (Figure **F12**). The seismic profile shows a continuous succession of hemipelagic sediment with acoustic basement estimated at ~225 mbsf (Rosenthal et al., 2016). This site was targeted to recover a complete Pleistocene record with unprecedented resolution for the WPWP.

The tectonic setting of Sites U1486 and U1487 (similar to that of the northern Papua New Guinea Sites U1484 and U1485) was shaped by the oblique northward movement of the Australian plate as it rapidly converged with the Pacific plate. This collision resulted in a complex plate boundary zone that includes volcanic arcs but also resulted in the formation and rotation of microplates within

this zone, as well as lithospheric rupture that formed small oceanic basins (Baldwin et al., 2012). The Bismarck Sea, on the northeastern side of Papua New Guinea (Figure **F12**), forms a back-arc basin with respect to the New Britain arc and is divided into the North Bismarck (NBS) and South Bismarck (SBS) microplates, separated by the active Bismarck Sea left-lateral transform fault and spreading segments (Taylor, 1979). Site U1486 is located on the NBS microplate. To the north, the NBS microplate is bordered by the Manus Trench, which defines the boundary between it and the Pacific plate. Within this complex tectonic regime, the southwestern side of the Manus Basin is considered one of the more stable regions. Magnetic anomalies in the Bismarck Sea indicate rapid asymmetric spreading since 3.5 Ma (Taylor, 1979). The continuous collision between the Australian and Pacific plates causes the SBS microplate to rotate rapidly clockwise (~9°/My), whereas the NBS microplate is rotating slowly anticlockwise (0.3–1.25°/My) (Baldwin et al., 2012). Asymmetric rotation of the North and South Bismarck Basins likely changed the position of New Britain and adjacent islands relative to Papua New Guinea. ODP Leg 193 focused on the eastern part of the Manus Basin, exploring the tectonic, volcanic, and seafloor hydrothermal system activity in this convergent plate margin setting.

An isotope record from piston Core MD05-2920 located near Site U1486 indicates a sedimentation rate of ~10 cm/ky, substantially higher than that found in other open-ocean Pacific sites, with no discernible disturbance for the past ~400 ky (Tachikawa et al., 2011, 2013). The moderately high $CaCO_3$ content (25–45 wt%) and well-preserved foraminifer tests suggest the potential to generate a suborbitally resolved paleoceanographic record of unprecedented quality through the Pleistocene. X-ray fluorescence scanning of Core MD05-2920 demonstrates that centennial precipitation variability can be resolved from the elemental content of the sediment (Tachikawa et al., 2011).

This site was targeted because of its potential to provide an excellent Pleistocene paleoceanographic record to examine orbital-scale climate variability at high resolution through the Pleistocene. The site is ideally located to monitor the contribution from the NGCC and NGCU to the ITF. The NGCC is the southern branch of the westward, cross-equatorial flowing SEC and constitutes the main southern Pacific contribution to the surface transport of the ITF. At ~1300 mbsl, this site is bathed by UCDW originating from the Southern Ocean (Figure **F5B**) and thus will allow for the reconstruction of past variability of this water mass.

Operations

After a 117 nmi transit from Site U1485, the vessel stabilized over Site U1486 at 0921 h on 14 November 2016. The original operations plan included three holes using the APC to 200 mbsf. We ultimately cored four holes (Table **T1**). Hole U1486A consisted of a single full core and was terminated because it did not recover the mudline. Holes U1486B and U1486C were cored to 211.2 and 201.3 mbsf, respectively. Hole U1486D was cored to 186.5 mbsf to fill coring gaps and intervals where significant numbers of interstitial water samples were taken from Hole U1486B for construction of the composite section.

Hole U1486A was cored to 9.5 mbsf with the APC using orientation and nonmagnetic hardware. When Core 363-U1486A-1H retrieved a full core liner, indicating that we missed the mudline, we terminated coring in this hole. A total of 9.95 m of sediment was recovered over 9.5 m of coring (105% recovery) in Hole U1486A.

Hole U1486B was cored to 211.2 mbsf (Cores 363-U1486B-1H through 23H) using the APC with orientation and nonmagnetic hardware. Downhole formation temperature measurements using the APCT-3 were taken on Cores 4H (34.5 mbsf), 7H (63.0 mbsf), 10H (91.5 mbsf), and 13H (120.0 mbsf), obtaining good results on all four deployments. Whole-round samples for high-resolution interstitial water analyses were taken at a frequency of one per section in the upper 150 mbsf of Hole U1486B. Core 23H seemed to be a full stroke; however, only 5.67 m of core was recovered. When drilling out the "rathole," drilling stalled at 211.2 mbsf, indicating something hard at that depth that the core barrel was unable to penetrate. Given that the acoustic basement at Site U1486 was estimated at ~225 mbsf, we speculate that we encountered the acoustic basement at a somewhat shallower depth. The presence of a few small basalt fragments in the core catcher of Core 23H supports this interpretation. We collected 215.49 m of sediment over 211.2 m of coring (102% recovery) in Hole U1486B.

Hole U1486C was cored to 201.3 mbsf (Cores 363-U1486C-1H through 23H) using the APC with orientation and nonmagnetic hardware. We decided to terminate coring above the hard layer encountered in Hole U1486B. Two drilled intervals (each 2 m) were used to advance the hole without recovery for stratigraphic correlation and one core (Core 11H) did not recover any material. We collected 172.70 m of sediment over 197.3 m of coring (88% recovery) in Hole U1486C.

Hole U1486D was cored to 186.5 mbsf in order to fill gaps in the composite stratigraphic section. Continuous coring penetrated to 153.2 mbsf (Cores 363-U1486-1H through 16H) with the APC using orientation and nonmagnetic hardware. We then drilled ahead without coring to 177 mbsf (23.8 m advance) to shoot Core 19H to capture a paleomagnetic reversal that was recovered in Hole U1486B but had fallen within a core gap in Hole U1486C. We collected 166.53 m of core over 162.7 m of coring (102% recovery) in Hole U1486D. Operations at Site U1486 ended at 1015 h on 17 November. Total time spent at Site U1486 was 73.0 h (3.0 d).

A total of 63 APC cores were recovered at this site, collecting 564.67 m of sediment over 580.7 m of coring (97.2% recovery).

Principal results

Sediment at Site U1486 is composed of ~212 m of upper Pliocene to recent volcanogenic sediment, biogenic sediment, and authigenic minerals overlying presumed oceanic crust, which was not cored. The relative abundance of the volcanogenic and biogenic components varies significantly downhole. We assign the recovered succession to one lithologic unit divided into three subunits (Figure **F17**). Subunit IA is an ~57 m sequence of mid-Pleistocene to recent mainly greenish gray biogenic sediment (predominantly foraminifer-rich nannofossil ooze) with clay minerals and rare ash layers. Biosilica is also present, usually in trace amounts, and consists of radiolarians, diatoms, and silicoflagellates. Pteropod tests are also found in the uppermost part of this subunit. The base of the subunit is placed at the first downhole occurrence of a black tephra layer. Subunit IB (~85 m thick) consists mainly of lower Pleistocene biogenic (predominantly nannofossil) sediment mixed with volcanogenic materials, which occur both as dispersed particles and distinct layers (tephra) and clay minerals. Foraminifers are present in varying abundances, as are radiolarians and diatoms, although they always constitute <10% of particles. This subunit is distinctly darker than Subunit IA due to larger proportions of volcanogenic sediment. The dominant lithologies are greenish gray foraminifer-rich nannofossil clay to dark greenish gray ash-rich nannofossil clay. Tephra layers are more abundant in Subunit IB and are typically felsic in composition. Pumice fragments are also present. The base of Subunit IB is defined at a prominent black volcanic ash layer that is marked by an increase in magnetic susceptibility; below this layer

Figure F17. Site U1486 results summary. cps = counts per second, SHMSL = Section Half Multisensor Logger.

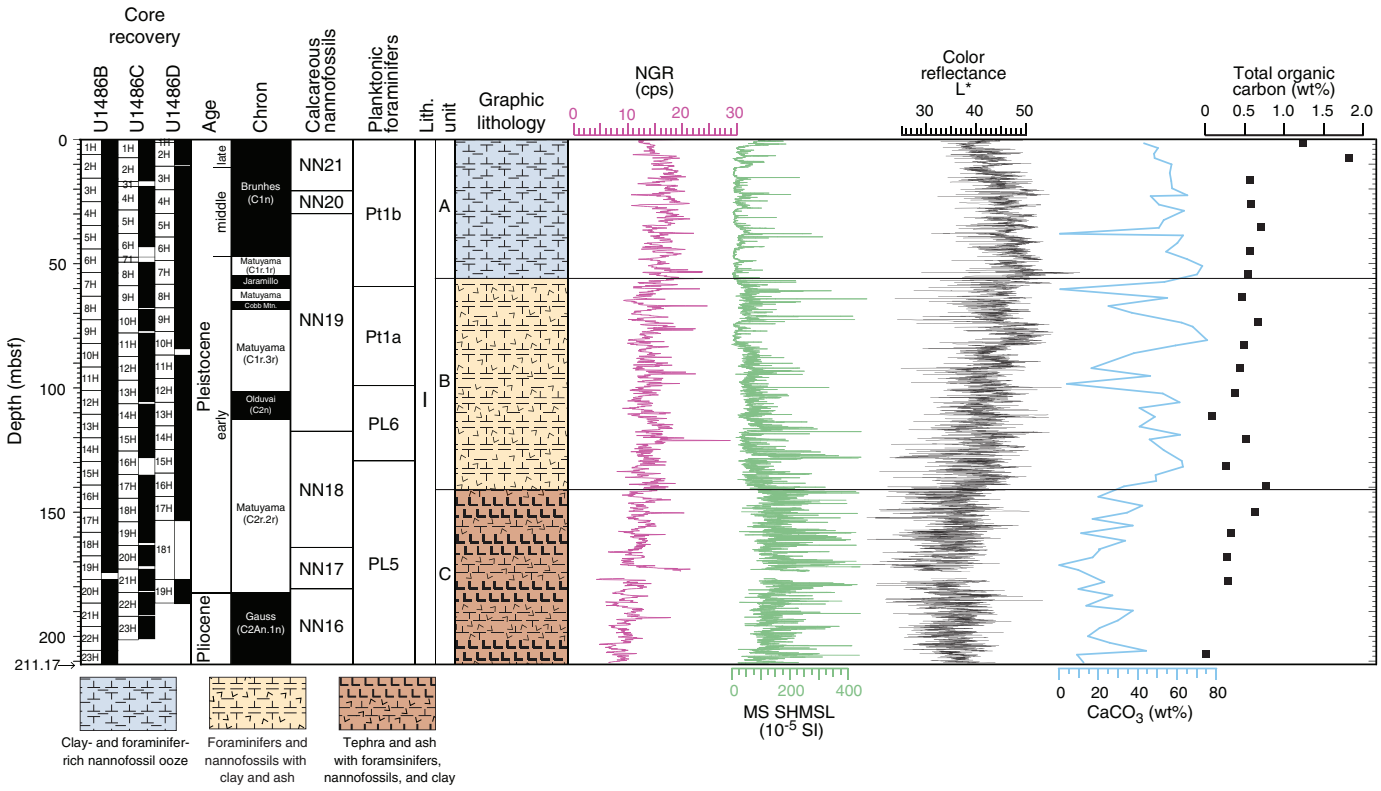

the sediment is distinctly darker in color (Figure **F17**). Subunit IC (~70 m thick; late Pliocene to early Pleistocene) is dominated by the volcanogenic component (ash), which occurs as discrete laminae and layers ranging from a few centimeters to >50 cm thick. These layers show a variety of depositional styles and occur both interbedded and mixed with the biogenic and lithogenic sediment (primarily foraminifer-rich nannofossil clay). The volcanogenic sediment in Subunit IC is more mafic in composition and includes brown volcanic glass and scoria fragments. The bottom ~4 m of Subunit IC is permeated by authigenic zeolites of probable hydrothermal origin. Centimeter-size fragments of basalt with olivine and pyroxene phenocrysts are also found in the bottom part of Subunit IC.

The sediment succession at Site U1486 contains planktonic foraminifers, benthic foraminifers, and calcareous nannofossils that are generally excellently preserved, although some foraminifers are fragmented or show evidence of cementation or incipient recrystallization. There is no obvious change in preservation state with depth; instead, foraminifers in layers with higher proportions of volcanogenic material appear slightly better preserved than those in the biogenic sediments. The benthic foraminifer assemblage is indicative of upper bathyal depths throughout the succession, with planktonic/benthic ratios around 99:1. *Planulina wuellerstorfi* is present in most core catcher samples. The significant amount of volcanic ash in the sediments below ~130 mbsf does not significantly affect the composition of the foraminifer and calcareous nannofossil assemblages.

Calcareous nannofossil and planktonic foraminifer biohorizons, together with magnetostratigraphic horizons, show good agreement (Figure **F18**). The base of the sedimentary sequence is assigned a late Pliocene age between 2.49 and 3.33 Ma, constrained by the presence of *Discoaster surculus* (biohorizon top at 2.49 Ma) and *Globigerinoidesella fistulosa* (biohorizon base at 3.33 Ma) in the absence of *Globorotalia truncatulinoides* (biohorizon base at 2.47 Ma). In the latest Pliocene and earliest Pleistocene, sedimentation rates were high, ~14 cm/ky. Extrapolation of these sedimentation rates yields an age of 2.7 Ma for the base of the recovered succession, which is consistent with the age range based on biohorizons. Sedimentation rates declined markedly through the middle to late Pleistocene to a long-term average of ~6 cm/ky. Based on these linear sedimentation rates, the Pliocene/Pleistocene boundary (2.58 Ma) is placed at ~183 mbsf, just below the base of Chron C2r.2r (2.581 Ma) (Figure **F17**).

Paleomagnetic investigations at Site U1486 involved measurement of the NRM of archive halves from all holes before and after demagnetization in a peak AF of 15 mT. We took two or three 7 cm^3 discrete samples per core from Hole U1486B (N = 49) to characterize the NRM demagnetization behavior and to investigate the rock magnetic properties of the sediment. Discrete magnetic susceptibility, IRM, and IRM ratios indicate relatively high ferrimagnetic mineral concentrations in the upper ~62 mbsf, greater influence of higher coercivity minerals between ~62 and 204 mbsf, and strongly ferrimagnetic phases in the bottom of the hole. Coarser magnetic grain sizes and higher magnetic concentrations in Subunit IC likely reflect the increased occurrence of mafic-rich volcanogenic sediment, with the highest magnetic concentrations associated with primary and altered basaltic fragments found at the bottom of the hole.

The Icefield MI-5 core orientation tool was deployed with nonmagnetic hardware for all cores, which permitted azimuthal correction of declination. Corrected declination is largely coherent between cores; however, absolute values in all holes cluster around 180° for normal polarity and 0° for reversed polarity, suggesting that

Figure F18. Age-depth plot for Site U1486 showing integrated biomagnetochronology for Hole U1486A. Sedimentation rates were ~6 cm/ky for most of the Pleistocene (0–125 mbsf) and 14 cm/ky in the Pliocene and earliest Pleistocene (below 125 mbsf). The base of the hole (203 mbsf) is assigned a latest Pliocene age, ~2.72 Ma, assuming a constant sedimentation rate of 14 cm/ky for the basal 20 m section.

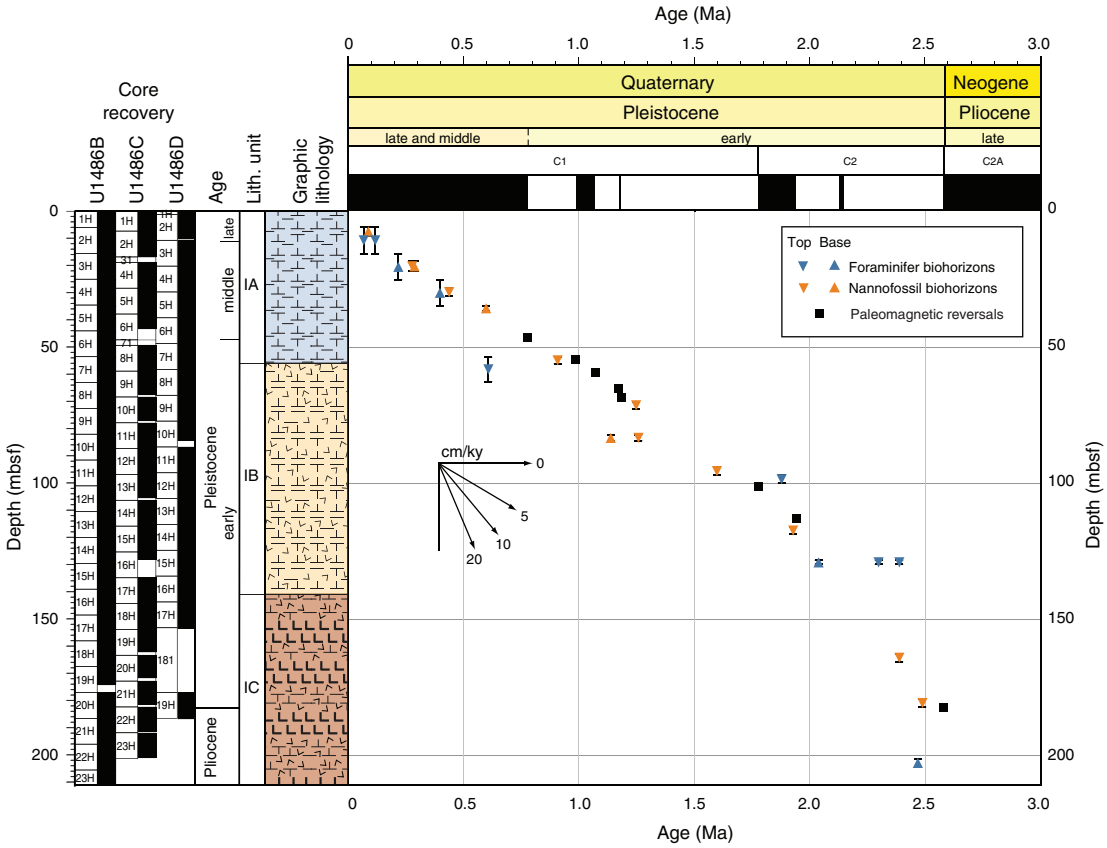

the issues of the baseline offset experienced at the majority of sites during Expedition 363 also affected these measurements. Across all three holes, we observed eight coeval and distinct ~180° changes in declination. These declination shifts occur at the same time that inclination changes from GAD-like values during normal polarity to steeper and more overprinted values during reversed polarity. The Matuyama/Brunhes boundary (0.781 Ma) is identified at ~47 mbsf (Figure **F17**). Below this boundary, we observed the upper (~55 mbsf; 0.988 Ma) and lower (~60 mbsf; 1.072 Ma) boundaries of the Jaramillo normal (C1r.1n), the upper (~66.5 mbsf; 1.173 Ma) and lower (~68.5 mbsf; 1.185 Ma) boundaries of the Cobb Mountain Subchron (C1r.2n), and the upper (~102 mbsf; 1.778 Ma) and lower (~113 mbsf; 1.945 Ma) boundaries of the Olduvai normal (C2n). The Gauss/Matuyama boundary (2.581 Ma) is at ~182 mbsf. Continued normal polarity below this depth in all three holes implies that the recovered sediment is <3.032 Ma because we did not observe the upper boundary of the Kaena reversed subchron (C2An.1n). These reversal horizons are in excellent agreement with both the calcareous nannofossil and planktonic foraminifer datums (Figure **F18**).

Physical property data collected for Site U1486, in particular magnetic susceptibility, show variations that correlate well with the three lithologic subunits defined for the site (Figure **F17**). Magnetic susceptibility values are low in the upper 57 mbsf (~20 × 10^{-5} to 50 × 10^{-5} SI), corresponding to Subunit IA, which consists primarily of biogenic components (foraminifers and nannofossils) mixed with clay and rare tephra layers. Over the same interval, GRA bulk density increases from 1.4 to 1.6 g/cm^3, although variability remains low. Between 57 and 140 mbsf (Subunit IB), average magnetic susceptibility values increase to ~75 × 10^{-5} to 100 × 10^{-5} SI, with frequent peaks reaching 200 × 10^{-5} to 400 × 10^{-5} SI. Within this interval, distinct peaks in magnetic susceptibility, GRA bulk density, and *P*-wave velocity are coincident with darker, volcanogenic-rich layers superimposed on background nannofossil clay with varying proportions of foraminifers and ash. GRA bulk density increases to 1.6 g/cm^3 in Subunit IB. Below 140 mbsf (Subunit IC), magnetic susceptibility average values increase (~200 × 10^{-5} SI) and distinct peaks in magnetic susceptibility, GRA bulk density, and *P*-wave velocity occur more frequently, reflecting the dominance of volcanogenic material in the deepest part of the succession. GRA bulk density reaches 1.8 g/cm^3 by 200 mbsf before decreasing to 1.7 g/cm^3 in the deepest part of Hole U1486B. Unusually high *P*-wave velocity values above 1800 m/s are also found in this interval. These high values coincide with the appearance of indurated sediment containing cemented zeolite precipitates and other minerals associated with the alteration of volcanic glass by hydrothermal fluids, suggesting that hydrothermal alteration was likely due to close proximity to the basaltic basement. NGR decreases linearly downhole from ~20 counts/s at the mudline to 8 counts/s at the bottom of the sedimentary sequence (Figure **F17**).

We constructed a continuous splice for Site U1486 from 0 to 222.59 m CCSF using three holes (U1486B, U1486C, and U1486D). Tie points were established mainly using WRMSL magnetic susceptibility data, aided occasionally by NGR data. Because Hole U1486B

was heavily sampled for interstitial water measurements (one 5–10 cm whole-round sample per section), we avoided using material from this hole for the splice from 0 to 150 mbsf, although this was unavoidable over a few intervals with poor recovery. The deepest core collected at Site U1486, which contains basalt fragments and is presumed to be within meters of volcanic basement, was appended to the bottom of the splice.

Site U1486 was sampled at high resolution (one 5–10 cm whole-round sample per section downhole to 150 mbsf) for interstitial water geochemistry. Of the 106 whole-round samples taken, 39 were processed for standard shipboard analyses, along with one mudline sample, and the remainder were archived for shore-based analyses. The interstitial water profiles reflect the variable sedimentation and tectonic evolution of the site over the past several million years. In the upper 60 mbsf, interstitial water profiles are dominated by moderate changes in alkalinity, SO_4, PO_4, NH_4, and Br that reflect a modest degree of organic matter remineralization. The minimum SO_4 concentration observed in Hole U1486B is ~19 mM, and methane is low (<4 ppm), which is consistent with the relatively low TOC content at the site (average = 0.5 wt%) (Figure **F17**). $CaCO_3$ content is highly variable, ranging from to 0.3 to 75.4 wt% with an average of 40.5 wt%. Overall, $CaCO_3$ content is higher in the upper 138 mbsf (Figure **F17**). Extremely low $CaCO_3$ content is found in ash and silt samples.

Deeper than 60 mbsf, interstitial water profiles show largely linear gradients toward the base of the hole that demonstrate the influence of upward diffusion on the profiles. Superimposed on these linear gradients is smaller scale variability, particularly noticeable in K, B, Na, pH, Cl, and Fe, which can be explained by the interaction of interstitial water with reactive volcanogenic sediment/minerals and clay-mineral alteration. The inverse relationship between Ca (increasing with depth) and Mg (decreasing with depth) is a common feature of sites that were drilled to oceanic basement and is attributed to submarine weathering of basal sediment and basalt (representing a source of Ca) and formation of authigenic clay (representing a sink for Mg). Marked changes in Cl, Mn, and Fe and an increase in SO_4 toward the base of the hole suggest communication not only between interstitial water and basement rock and sediment, but also with crustal fluids.

Site U1487

Background and objectives

Site U1487 (proposed Site WP-14A) is located ~190 km west-southwest of Manus Island at 02°20.00′S, 144°49.17′E in 874 m water depth (Figure **F12**). The site is situated on seismic Line RR1313-WP6-5, ~1.4 km southwest of the crosspoint with Line RR1313-WP6-3a. The seismic profile shows a continuous succession of hemipelagic sediment with acoustic basement estimated at ~185 mbsf (Rosenthal et al., 2016).

The tectonic setting of Sites U1486 and U1487 (similar to that of the northern Papua New Guinea sites) was shaped by the oblique northward movement of the Australian plate as it rapidly converged with the Pacific plate. This collision resulted in a complex plate boundary zone that includes volcanic arcs but also resulted in the formation and rotation of microplates within this zone, as well as lithospheric rupture that formed small oceanic basins (Baldwin et al., 2012). The Bismarck Sea, on the northeastern side of Papua New Guinea (Figure **F12**), forms a back-arc basin with respect to the New Britain arc and is divided into the NBS and SBS microplates, separated by the active Bismarck Sea left-lateral transform fault and spreading segments (Taylor, 1979). Site U1487 is located on the NBS microplate. To the north, the NBS microplate is bordered by the Manus Trench, which defines the boundary between it and the Pacific plate. Within this complex tectonic regime, the southwestern side of the Manus Basin is considered one of the more stable regions. Magnetic anomalies in the Bismarck Sea indicate rapid asymmetric spreading since 3.5 Ma (Taylor, 1979). The continuous collision between the Australian and Pacific plates caused the SBS microplate to rotate rapidly clockwise (~9°/My), whereas the NBS microplate is rotating slowly anticlockwise (0.3°–1.25°/My) (Baldwin et al., 2012). Asymmetric rotation of the North and South Bismarck Basins likely changed the position of New Britain and adjacent islands relative to Papua New Guinea. ODP Leg 193 focused on the eastern part of Manus Basin, exploring the tectonic, volcanic, and seafloor hydrothermal system activity in this convergent plate margin setting.

Site U1487 is upslope from Site U1486 and is expected to show the same sediment composition but with reduced sedimentation rate because of its shallower position. As a companion to Site U1486, Site U1487 was also targeted because of its potential to provide an excellent Pleistocene paleoceanographic record to examine orbital-scale climate variability at high resolution through the Pleistocene. The site is also ideally located to monitor the contribution of the NGCC and NGCU to the ITF. The NGCC is the southern branch of the westward, cross-equatorial flowing SEC and constitutes the main southern Pacific contribution to the surface transport of the ITF. At a water depth of ~880 mbsl, this site is bathed by modified Antarctic Intermediate Water originating from the Southern Ocean (Figure **F5B**) and thus will allow for the reconstruction of past variability of this water mass.

Operations

After a 13.3 nmi transit from Site U1486, the vessel stabilized over Site U1487 at 1145 h on 17 November 2016. Site U1487 was an alternate site added to the operations during the expedition. We planned two holes using the APC to ~175 mbsf, with a third hole to cover stratigraphic gaps if required. We ultimately cored two holes; Hole U1487A was cored to 144.2 mbsf, and Hole U1487B was cored to 144.3 mbsf (Table **T1**).

Hole U1487A was cored with the APC using orientation and nonmagnetic hardware to 144.2 mbsf (Cores 363-U1487A-1H through 16H). Downhole formation temperature measurements using the APCT-3 were taken on Cores 4H (34.9 mbsf), 7H (63.4 mbsf), 10H (91.9 mbsf), and 13H (120.4 mbsf), obtaining good results on all four deployments. We terminated coring after Cores 14H and 16H recorded partial strokes, and Core 15H had to be drilled over due to excessive overpull when attempting to retrieve it. Cores 14H through 16H included unconsolidated sand. We collected 146.43 m of sediment over 144.2 m of coring (102% recovery) in Hole U1487A.

Hole U1487B was then cored to 125.5 mbsf (Cores 363-U1487B-1H through 14H) with the APC using orientation and nonmagnetic hardware. We switched to the HLAPC to core the interval where we encountered unconsolidated sand in Hole U1487A. We cored to 144.3 mbsf (Cores 15F through 18F) with the HLAPC, where we terminated the hole. We collected 148.73 m of core over 144.3 m of coring (103% recovery) in Hole U1487B. Operations at Site U1487 ended at 2215 h on 18 November. Total time spent at Site U1487 was 34.5 h (1.4 days).

A total of 30 APC cores were recovered at this site, collecting 276.34 m of sediment over 269.7 m of coring (102.5% recovery). We also collected 4 HLAPC cores, retrieving 18.82 m of sediment over

Figure F19. Site U1487 results summary. cps = counts per second.

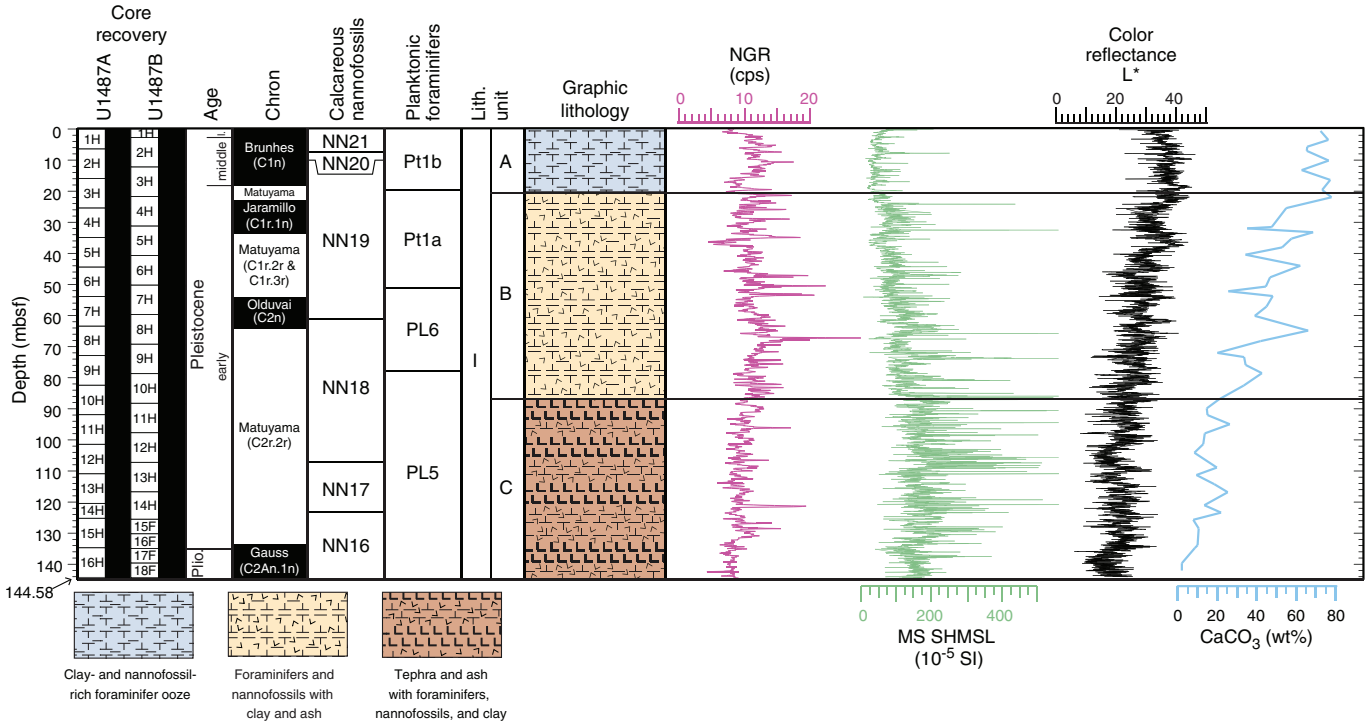

18.8 m of coring (100.1% recovery). In total, we collected 295.16 m of sediment over 288.5 m of coring (102.3% recovery).

Principal results

Sediment at Site U1487 is composed of ~144 m of upper Pliocene to recent volcanogenic, authigenic, and biogenic sediment, with a sequence similar to that seen at Site U1486, which is located 25 km west-southwest. We assigned the recovered succession to one lithologic unit divided into three subunits (Figure **F19**), with the subunits distinguished based on the amount of volcanogenic material in the sediment. Subunit IA (late Pleistocene to recent) spans the upper ~21 m and is composed primarily of biogenic (foraminifer and nannofossil) sediment mixed with clay minerals with rare ash layers. The dominant lithology is nannofossil-rich foraminifer ooze, whereas the sediment at Site U1486 is finer grained and consists mostly of foraminifer-rich nannofossil ooze. Trace amounts of siliceous components (radiolarians, diatoms, and silicoflagellates) are also present. Pteropods are found in the uppermost part of the section. The base of Subunit IA is placed at the second downhole tephra layer, which marks an increase in the proportion of volcanic particles in the sediment. Subunit IB (late Pleistocene) extends from the base of Subunit IA to ~86 mbsf. Biogenic sediment (predominantly foraminifers) is still the main sedimentary component of this subunit, but volcanogenic sediment is more abundant here than in Subunit IA. The main lithology is nannofossil-bearing to nannofossil-rich ash-rich foraminifer ooze. Siliceous microfossils remain present in trace amounts. Tephra layers are typically brown to black and composed primarily of glass shards, indicative of explosive volcanism. Black tephra layers become more common toward the base of the subunit. As at Site U1486, the base of Subunit IB is marked by a prominent volcanic ash layer that corresponds with a shift to higher magnetic susceptibility values (Figure **F19**). Subunit IC (late Pliocene to early Pleistocene) marks the transition from dominantly biogenic above to dominantly volcanogenic sediment below. The principal lithology is ash with varying proportions of nannofossils, foraminifers, and clay. The volcanogenic component in Subunit IC is primarily composed of microscoria, rather than glass, and was likely sourced from less explosive eruptions.

The sedimentary sequence recovered at Site U1487 exhibits many similarities to that recovered at Site U1486. Both sites span the past ~2.7 My and exhibit a reduction in volcanogenic input through time. Despite the overall similarity between the two sites, we note four important differences in the sedimentology of Site U1487 relative to Site U1486:

1. An overall coarser grain size (foraminifer ooze versus nannofossil ooze),
2. Lower sedimentation rates,
3. More intense bioturbation and reworking, and
4. Thicker tephra layers with larger microscoria fragments.

The sediment succession at Site U1487 contains calcareous nannofossils, planktonic foraminifers, and benthic foraminifers throughout. Microfossil preservation is excellent to very good. Benthic foraminifers indicate a deepwater bathyal sedimentary environment with a planktonic/benthic foraminifer ratio typically 99:1 throughout the succession.

Biostratigraphic and magnetostratigraphic horizons are generally in good agreement. The oldest sediment recovered belongs to calcareous nannofossil Zone NN16 and planktonic foraminifer Zone PL5 (late Pliocene) and is estimated to be 2.65 Ma based on extrapolation of the age-depth trend (Figure **F20**). From the base of the hole to ~2 Ma, sedimentation rates averaged ~15 cm/ky, mainly because of the very high rate of volcanic ash deposition early in the site's history. Sedimentation rates slowed significantly in the Pleistocene, averaging ~3.5 cm/ky (Figure **F20**).

Paleomagnetic investigations at Site U1487 involved measurement of the NRM of archive-half sections from Holes U1487A and U1487B before and after demagnetization in a peak AF of 15 mT.

Figure F20. Age-depth plot for Site U1487 showing integrated biomagnetochronology for Hole U1487A. Sedimentation rates averaged ~3.5 cm/ky through much of the Pleistocene (0–60 mbsf) and ~15 cm/ky in the Pliocene and earliest Pleistocene (deeper than 60 mbsf). The age of the oldest recovered sediment is estimated at 2.65 Ma based on extrapolation of the age-depth trend.

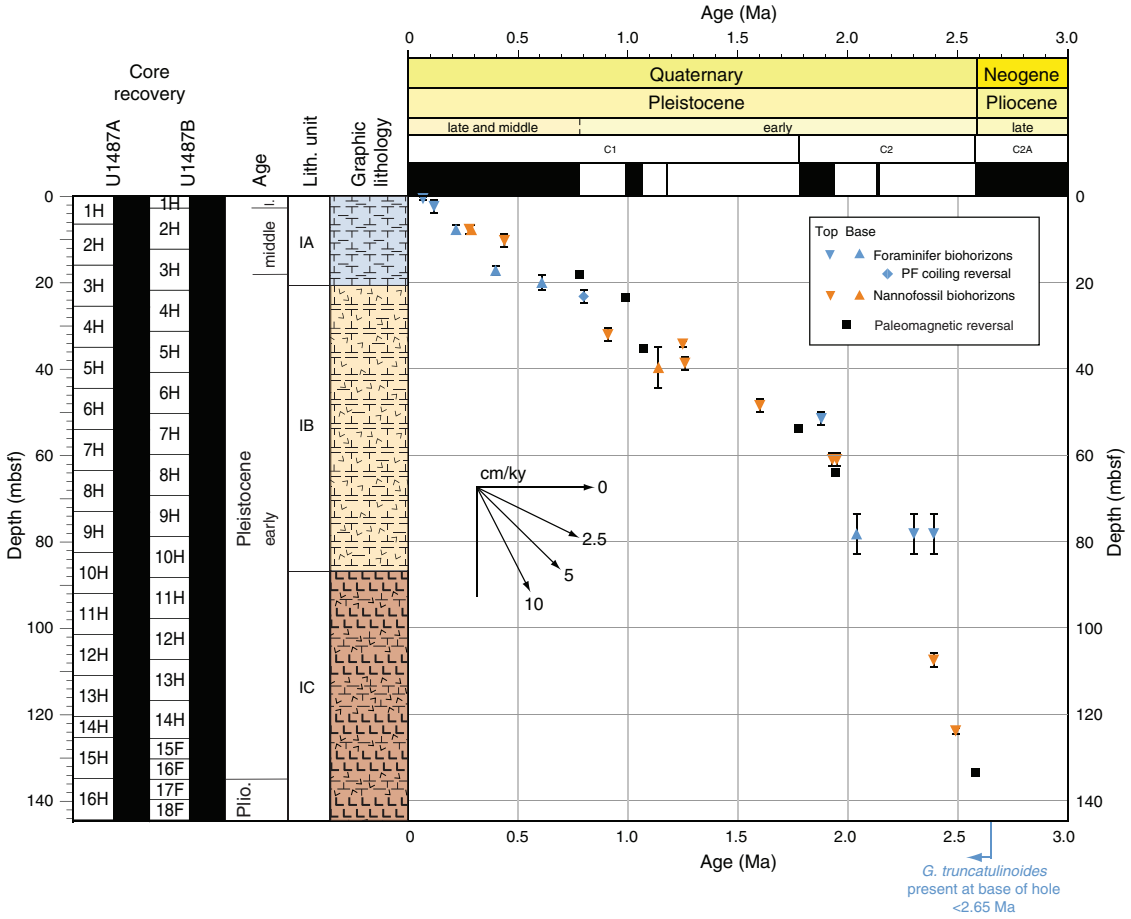

Corrected declination is largely coherent between cores; however, absolute values in all holes cluster around 180° for normal polarity and 0° for reversed polarity, suggesting that the issues of the baseline offset experienced at the majority of sites during Expedition 363 affected these measurements. Relatively soft ferrimagnetic minerals are concentrated in the upper ~24 mbsf; increased magnetic concentration and coercivity with depth likely reflect the increased deposition of mafic-rich volcanogenic ash and tephra. We identify six 180° shifts in declination at Site U1487; the deepest of these is the Gauss/Matuyama boundary (2.582 Ma) at ~134 mbsf (Figure **F19**). Continued normal polarity below this depth in both holes implies that the recovered sediment is younger than 3.032 Ma because we do not observe the upper boundary of the Kaena reversed subchron (C2An.1n). The magnetostratigraphy is in good agreement with both the calcareous nannofossil and planktonic foraminifer datums (Figure **F20**).

All physical property data at Site U1487 exhibit excellent reproducibility between holes and show typical trends consistent with increased downhole volcanogenic input. As with Site U1486, the trends and variability in the Site U1487 physical property data correlate well with the three defined lithologic subunits. These subunits are most easily recognized in magnetic susceptibility, which is low in the upper 22 mbsf (~20 × 10^{-5} to 50 × 10^{-5} SI), corresponding to lithologic Subunit IA, which consists of nannofossil-rich foraminifer ooze with variable amounts of clay and ash (Figure **F19**). Over the same interval, GRA bulk density increases from 1.4 to 1.6 g/cm^3, albeit with low variability. Between 22 and 86 mbsf (Subunit IB), average magnetic susceptibility increases to ~75 × 10^{-5} to 100 × 10^{-5} SI, with a concomitant increase in variability. GRA bulk density also increases to 1.6 g/cm^3. Within Subunit IB, distinct peaks in magnetic susceptibility, GRA bulk density, and *P*-wave velocity occur coincident with darker, volcanogenic-rich layers, superimposed on a background lithology of nannofossil-rich foraminifer ooze with variable clay and ash content. The highest NGR values (~20 counts/s) occur in the upper ~86 mbsf (Subunits IA and IB) of Site U1487, reflecting higher clay content in these subunits relative to Subunit IC (Figure **F19**). NGR variability in the upper 86 mbsf probably reflects changes in the amount of biogenic material. Below 86 mbsf (Subunit IC), average magnetic susceptibility increases to ~200 × 10^{-5} SI and the distinct peaks in magnetic susceptibility, GRA bulk density, and *P*-wave velocity occur more frequently, reflecting the dominance of volcanogenic material in the deepest part of the site.

We constructed a continuous splice for Site U1487 from 0 to 136.0 m CCSF using both Holes U1487A and U1487B. We used WRMSL magnetic susceptibility data aided occasionally by NGR and GRA bulk density to correlate between the holes. Because Hole U1487A was sampled for interstitial water measurements, our general approach was to use Hole U1487B as the backbone of the splice and to use short segments from Hole U1487A to cover gaps in re-

covery encountered in Hole U1487B. There is considerable coarse sand below 136.0 m CCSF, and the WRMSL data did not correlate well between the holes due to drilling disturbance, including possible flow-in that occurred while retrieving the cores from the bottom of the hole. For this reason, the splice has gaps and uncertain tie points from 136.0 m CCSF to the bottom of the hole at 156.0 m CCSF.

Site U1487 was sampled at standard resolution for interstitial water chemistry (~1 whole-round sample per core), with a total of 18 whole-round samples and 1 mudline sample analyzed. Despite the relative proximity of Sites U1487 and U1486, the profiles at Site U1487 display distinct differences from those at Site U1486. Low PO_4 and NH_4 concentrations (<1.5 µM and 0.2 mM, respectively) and a relatively high SO_4 concentration (>24 mM) downhole suggest lower organic matter content at Site U1487. Concentration of methane also remains low throughout the hole. Small downhole interstitial water gradients were observed in several elements (K, Li, and B) and likely reflect clay mineral authigenesis. However, the majority of the interstitial water profiles at Site U1487 display little to no variation with depth and appear to be influenced by advection and/or diffusion of crustal fluids. For example, Ca and Mg concentrations both change by >15 mM from the mudline to ~5 mbsf but vary by <1 mM below that depth. Higher permeability expected from the generally coarser sediment grain size and presence of several faults near Site U1487 that penetrate from the basement through the majority of the sediment column may help facilitate fluid migration.

$CaCO_3$ content shows a monotonic decreasing trend with depth, with $CaCO_3$ content ranging from >60 wt% in the upper 20 mbsf to <10 wt% in the bottom 15 m of the recovered sequence (Figure **F19**). Comparison of $CaCO_3$ content with GRA bulk density data suggests that this trend can be explained by two-component mixing between biogenic carbonate (dominant in the upper portions of the hole) and volcanogenic sediment (dominant in the lower portions of the hole).

Site U1488

Background and objectives

Site U1488 (proposed Site WP-03A) is located atop the southern part of the Eauripik Rise at 02°02.59′N, 141°45.29′E in 2604 m water depth (Figure **F21**). The site is situated on seismic Line RR1313-WP3-1, ~4.4 km southwest of the intersection with seismic Line RR1313-WP3-3. The seismic profile shows a continuous succession of hemipelagic, carbonate-rich sediment with basement at >650 mbsf (Rosenthal et al., 2016). Site U1488 is located ~28 km northwest of Deep Sea Drilling Project (DSDP) Site 62 (Figure **F21**) and close to the location of piston Core MD97-2140, which was used to reconstruct the Pleistocene SST history of the WPWP (de Garidel-Thoron et al., 2005). Leg 7 recovered a nearly continuous sequence of upper Oligocene to Quaternary chalk and carbonate-rich ooze from Site 62 (Winterer and Riedel, 1971). However, recovery was relatively poor, and the sediment was frequently disturbed due to the use of the RCB system.

Site U1488 is situated on the Eauripik Rise within the Caroline Basin north of Papua New Guinea (Figure **F3**). The roughly north–south trending Eauripik Rise is an ~250 km wide aseismic ridge that rises ~1–2 km above the surrounding seafloor and separates the East and West Caroline Basins. Magnetic Anomalies C13–C9 in both basins show that ocean crust formed along roughly east–west spreading centers from the Eocene until the late Oligocene. Offsets in these anomalies and the lack of magnetic lineations beneath the Eauripik Rise support the interpretation that it formed due to excess submarine volcanism along a leaky north–south transform fault

Figure F21. Eauripik Rise and Caroline Basin map (green box in Figure F3) showing the location of Sites U1488–U1490 (yellow circles) and DSDP Site 62 (purple circle). Contour interval = 500 m. Bathymetric data are from Amante and Eakins (2009).

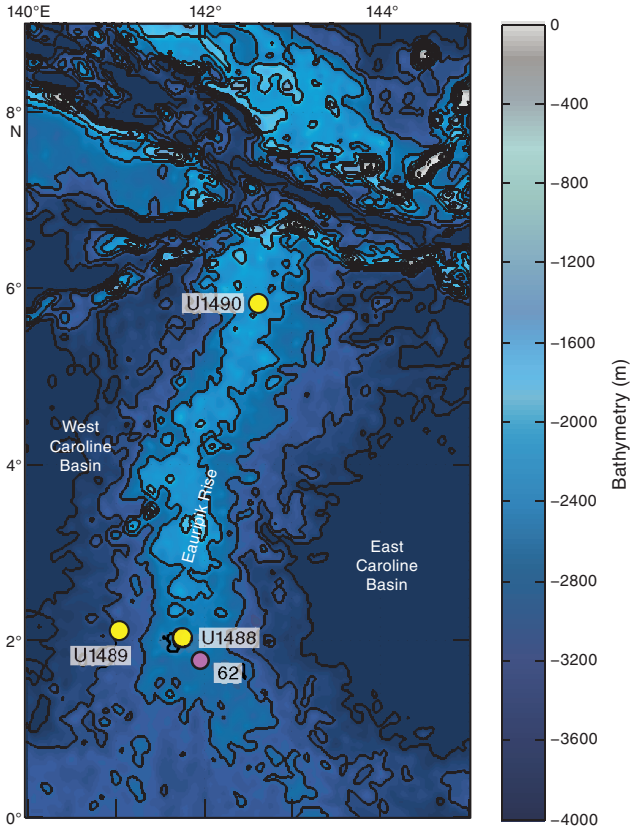

(Hegarty and Weissel, 1988.) An alternative interpretation attributes the formation of the Eauripik Rise to the northward passage of a mantle hotspot that contributed to the tectonically and structurally complex region surrounding the Sorol Trough (Bracey, 1975). Seismic refractions show thickened ocean crust beneath the Eauripik Rise, and a small free air anomaly and positive geoid anomaly indicate a compensated structure reaching deep into the mantle (Hegarty and Weissel, 1988). Although there are no discernible magnetic lineations on the Eauripik Rise, these data and the recovery of tholeiitic basalt at Site 62 (Shipboard Scientific, 1971) make it difficult to argue that it is a remnant of ancient continental material. The igneous rocks recovered from the bottom of Site 62 are slightly vesicular, highly altered, and contain calcite veins with well-preserved foraminifers and nannofossils. The dolomitization of overlying limestone suggests that these basalts intruded into marine chalk, leading to extensive diagenetic reactions near the base of the sedimentary succession.

Site U1488 is located ~2° north of the Equator and is thus suitable for reconstructing the hydrographic history of the WPWP. The comparatively low sedimentation rate at this site, typical of open-ocean environments, will be used along with the record from Site U1490 to reconstruct the evolution of the WPWP since the late Miocene. At 2600 mbsl the site is bathed by modified UCDW (Figure **F5A**) and therefore will be useful to monitor past changes in this water mass. High-resolution interstitial water sampling at this site will be used for geochemical reconstructions of the deep Pacific water mass ($\delta^{18}O$, salinity, and seawater chemistry) during the LGM.

Operations

After a 333.2 nmi transit from Site U1487, the vessel stabilized over Site U1488 at 0400 h on 20 November 2016. The original operations plan called for three holes: the first to APC refusal, estimated at 250 mbsf, followed by two holes to 300 mbsf using both the APC and XCB coring systems. We ultimately cored three holes using only the APC and HLAPC systems, with the deepest penetrating to ~315 mbsf (Table **T1**).

Hole U1488A was cored with the APC system using orientation and nonmagnetic hardware to 300.4 mbsf (Cores 1H through 32H). Downhole formation temperature measurements using the APCT-3 were taken on Cores 4H (34.4 mbsf), 7H (62.9 mbsf), 10H (91.4 mbsf), and 13H (119.9 mbsf), obtaining good results on all four deployments. We also collected high-resolution interstitial water samples at a frequency of one whole-round (5–10 cm) sample per section over the upper 150 mbsf of Hole U1488A. After Cores 31H and 32H had excessive overpull and required drillover to extract them from the formation, we switched to the HLAPC system and continued coring to 314.5 mbsf (Cores 33F through 35F). Because Cores 33F and 35F also required drillover, indicating HLAPC refusal, we terminated coring. We collected 327.20 m of sediment over 314.5 m of coring (104% recovery) in Hole U1488A.

Hole U1488B was cored to 304.9 mbsf (Cores 1H through 33H) with the APC system using orientation and nonmagnetic hardware. Cores 31H through 33H required drillover, indicating APC refusal, so we terminated coring. We collected 315.77 m of core over 304.9 m of coring (104% recovery) in Hole U1488B.

Hole U1488C was cored to recover material for the stratigraphic splice over the upper 150 mbsf, since high-resolution interstitial water sampling was conducted in Hole U1488A over this interval. APC coring using orientation and nonmagnetic hardware proceeded to 159.3 mbsf (Cores 1H through 17H), where we terminated coring. We collected 153.60 m of core over 159.3 m of coring (96.4% recovery) in Hole U1488C.

Operations at Site U1488 ended at 1030 h on 24 November. Total time spent at Site U1488 was 102.5 h (4.3 days). A total of 82 APC cores were recovered at this site, collecting 781.74 m of sediment over 764.6 m of coring (102.2% recovery). We also collected 3 HLAPC cores, retrieving 14.83 m of sediment over 14.1 m of coring (105.2% recovery). In total, we collected 796.57 m of sediment over 778.7 m of coring (102.3% recovery) at Site U1488.

Principal results

We recovered an ~315 m succession of upper Miocene to recent foraminifer-rich nannofossil ooze to foraminifer-nannofossil ooze in three holes at Site U1488. The sediment is assigned to a single lithologic unit (Figure **F22**). Siliciclastic (mainly clay minerals), siliceous (radiolarians, diatoms, sponge spicules, and silicoflagellates), and volcanogenic (ash) particles are present as minor sediment components. Authigenic sulfide precipitates and authigenic clay minerals (e.g., smectite–chlorite) also occur as accessories. The sediment varies downhole with small changes in the color and abundance of different components. The upper ~50 mbsf is composed of light greenish gray clay- and foraminifer-rich nannofossil ooze that transitions to greenish white foraminifer-rich nannofossil ooze between ~50 and ~250 mbsf. The bottom part of the site (deeper than ~250 mbsf) is primarily yellowish white radiolarian/diatom-bearing foraminifer-rich nannofossil ooze. Bioturbation is slight to moderate. Three volcanic ash layers composed of fresh, angular, and colorless glass shards are found at ~6.5, ~93, and ~100 mbsf (Figure **F22**).

Calcareous microfossil assemblages and preservation at Site U1488 are typical of a pelagic, relatively deepwater bathyal environment throughout the recovered succession. Unlike previous sites (U1482–U1487), microfossil preservation at Site U1488 shows a marked increase in recrystallization (foraminifers) and some fragmentation, etching, and overgrowth (foraminifers and calcareous nannofossils) downhole. Biostratigraphic and magnetostratigraphic horizons indicate recovery of a continuous sequence of pelagic sediment spanning the last ~10 My (Figure **F23**). The oldest sediment recovered at Site U1488 is constrained to be younger than ~10.47 Ma by the absence of the planktonic foraminifer *P. mayeri* and older than 9.69 Ma by the presence of the calcareous nannofossil *Catinaster coalitus*. The Miocene/Pliocene boundary (5.333 Ma) is placed at ~149 mbsf (Figure **F22**) based on linear interpolation between the biohorizon base *Ceratolithus armatus* (5.35 Ma) and biohorizon base *Ceratolithus cristatus* (5.12 Ma). The base of the late Pliocene (3.60 Ma) is placed at ~92 mbsf, between the biohorizon top *Reticulofenestra pseudoumbilicus* (3.70 Ma) and biohorizon top *Sphenolithus abies* (3.54 Ma). The Pliocene/Pleistocene boundary is placed at ~60 mbsf, just below the base of Chron C2r.2r at 59.70 mbsf, and the base of the middle Pleistocene is at the base of Chron C1n at ~19 mbsf. The middle/late Pleistocene boundary is placed between the biohorizon top *P. lacunosa* (0.44 Ma) and biohorizon top *G. ruber* (pink) (0.12 Ma) at ~12 mbsf. Long-term average sedimentation rates through the late Miocene and Pliocene were remarkably consistent at ~4 cm/ky. These rates roughly halved through the early Pleistocene (~2 cm/ky) before they increased in the middle to late Pleistocene (~3 cm/ky) (Figure **F23**). Benthic foraminifer assemblages are characteristic of intermediate to deep bathyal depths with *Laevidentalina* spp. and *Uvigerina* spp. as the dominant forms.

Paleomagnetic investigations at Site U1488 involved measurement of the NRM of archive-half sections from Hole U1488A, the upper ~67 mbsf of Hole U1488B, and the upper ~102 mbsf in Hole U1488C before and after demagnetization in a peak AF of 15 mT. Corrected declination is largely coherent between cores; however, absolute values in all holes cluster between 90° and 180° for periods of normal polarity and between 270° and 0°/360° for reversed polarity, suggesting that the issues of a baseline offset experienced at the majority of sites during Expedition 363 also affected these measurements. Relatively soft ferrimagnetic minerals are concentrated in the uppermost ~45 mbsf. Between ~45 and ~50 mbsf, NRM_{15mT}, magnetic susceptibility, and SIRM values decrease, and below ~50 mbsf, average magnetic susceptibility values fall to 0.6×10^{-5} SI. NRM_{15mT}, magnetic susceptibility, and SIRM values deeper than ~50 mbsf are approximately two orders of magnitude lower than those in the upper ~45 mbsf and often approach the noise level of their respective instruments, indicating a significant reduction in magnetic mineral concentration deeper than ~50 mbsf that resulted in an uninterpretable paleomagnetic record. We identify six 180° shifts in declination in Holes U1488A and U1488B and nine horizons in Hole U1488C (Figure **F23**) before ultimate degradation of the paleomagnetic signal. The deepest of these are the Gauss/Matuyama boundary (2.582 Ma) at ~60 mbsf in Holes U1488A and U1488B and the upper boundary of C2An.2n (~82 mbsf; 3.207 Ma) in Hole U1488C (Figure **F22**).

All physical properties at Site U1488 exhibit excellent reproducibility between holes. GRA bulk density shows an increasing trend with depth from 1.4 g/cm^3 at the seafloor to 1.8 g/cm^3 at the bottom of the hole, likely caused by compaction. At a break in this trend between ~245 and 285 mbsf, values remain at ~1.75 g/cm^3 before increasing to 1.8 g/cm^3. *P*-wave velocity also shows an increasing trend with depth caused by compaction, increasing from 1500 m/s at the seafloor to ~1600 m/s at 310 mbsf. NGR values are ~25 counts/s at the seafloor and then rapidly decreases to ~8 counts/s

Figure F22. Site U1488 results summary. cps = counts per second.

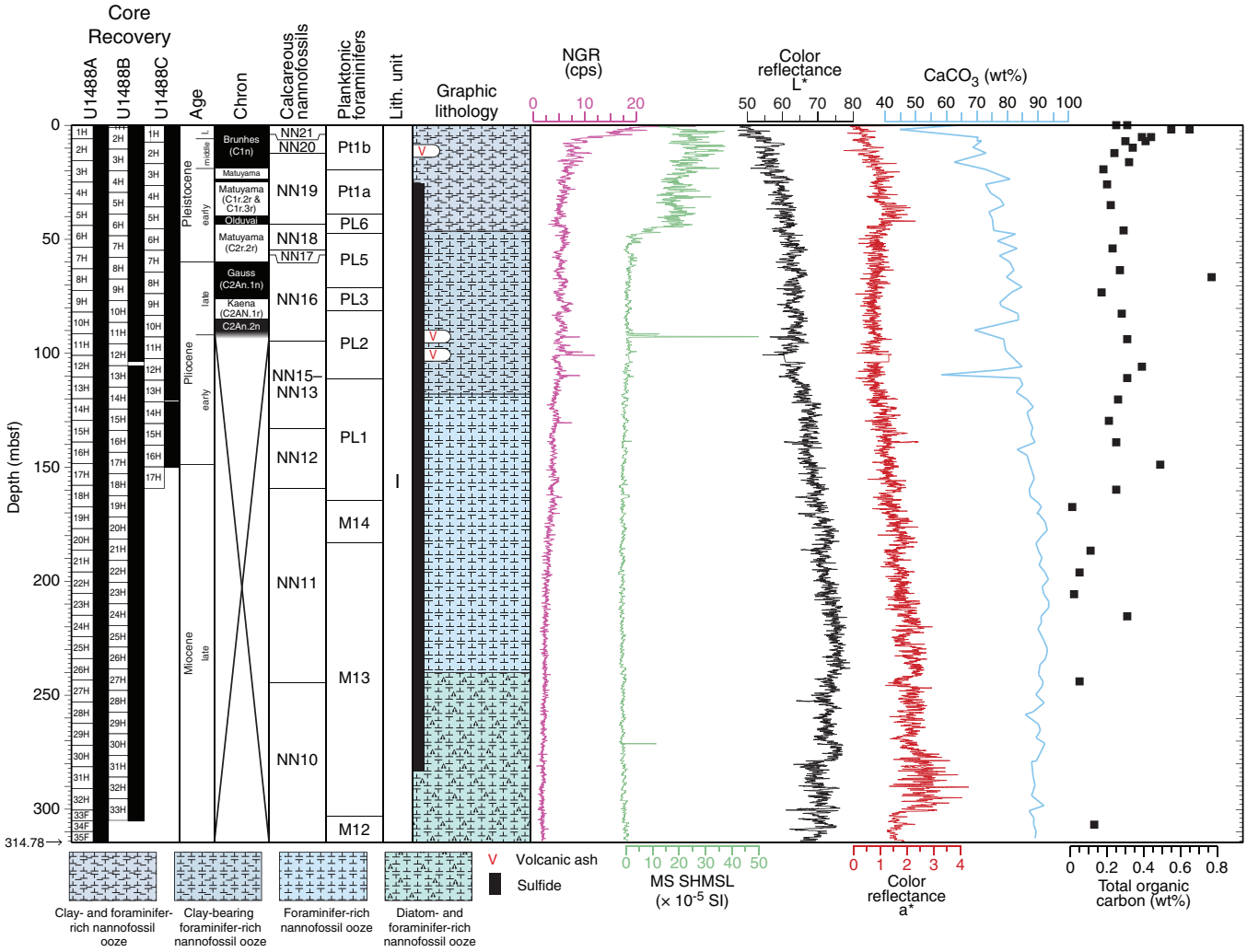

by 8 mbsf. NGR then gradually decreases to 2 counts/s over the length of the record. Magnetic susceptibility also initially exhibits moderate susceptibility (~30 × 10^{-5} SI) before decreasing abruptly at ~45 mbsf to values averaging <3 × 10^{-5} SI to the bottom of the site (Figure **F22**). Thermal conductivity increases from 0.9 to 1.3 W/(m·K) from the seafloor to the bottom of the hole. Deeper than 150 mbsf, the thermal conductivity slope decreases and variability increases. Downhole formation temperature measurements indicate a geothermal gradient of 59°C/km at Site U1488.

We constructed a continuous splice for Site U1488 from 0 to 324.89 m CCSF using three holes (U1488A, U1488B, and U1488C). Tie points were established with WRMSL magnetic susceptibility, GRA bulk density, and *P*-wave velocity data, as well as NGR and L* color reflectance data. Because the upper 150 mbsf (equivalent to ~162 m CCSF) of Hole U1488A was heavily sampled (one 5 or 10 cm whole-round sample per section) for high-resolution interstitial water analyses, our general approach was to avoid using material from that interval in Hole U1488A because Hole U1488C was cored specifically to recover material for the splice. The splice is continuous and well constrained from 0 to 324.89 m CCSF, although a few tentative tie points should be verified during postcruise research. Only Hole U1488A penetrated deeper than 324.89 m CCSF, and therefore we appended the last two cores of Hole U1488A to the bottom of the splice.

At Site U1488, a total of 113 whole-round samples and one mudline sample were collected for interstitial water analysis. High-resolution sampling was conducted in the upper 150 mbsf of Hole U1488A with the goal of reconstructing Cl concentration and $\delta^{18}O$ of UCDW during the LGM. Preliminary shipboard chlorinity measurements suggest that reconstruction of the salinity of UCDW will be possible with the samples collected.

The interstitial water profiles at Site U1488 are controlled in large part by carbonate diagenesis, indicated by a steady 10-fold enrichment in Sr down to ~100 mbsf accompanied by an increase of dissolved Ca, although a moderate increase in alkalinity over the same depth suggests both dissolution and recrystallization are taking place. Deeper than ~100 mbsf, linear increases in alkalinity, SO_4, Ca, and Li and decreases in Sr, K, and pH are likely reflecting communication with a deep fluid source through diffusion. In general, $CaCO_3$ is the major constituent of the sediment of Site U1488, with an average content of 83.5 wt% (Figure **F22**). $CaCO_3$ content increases with depth from ~70 wt% near the seafloor to >90 wt% at ~170 mbsf. TOC content shows several stepwise decreases downhole, from ~0.5 to 0.2 wt% in the uppermost 25 mbsf and then further decreases from 0.2 wt% at ~170 mbsf to minimal values that often are below the detection limit (Figure **F22**). TN content shows a trend similar to that of TOC content. Shallower than 80 mbsf, where both TOC and TN contents are above the detection limit, the

Figure F23. Age-depth plot for Site U1488 showing integrated biomagnetochronology for Hole U1488A. Magnetochron reversals from Hole U1488C are shown where they extend below those reliably recorded in Hole U1488A. Age of the oldest recovered sediment at Site U1488 is constrained to ~10.47 Ma by the absence of the PF *Paragloborotalia mayeri* and >9.69 Ma by the presence of the calcareous nannofossil *Catinaster coalitus* at 314.52 mbsf. Sedimentation rates averaged ~2–3 cm/ky in the Pleistocene (0–50 mbsf) and ~4 cm/ky in the late Miocene to Pliocene (below 50 mbsf).

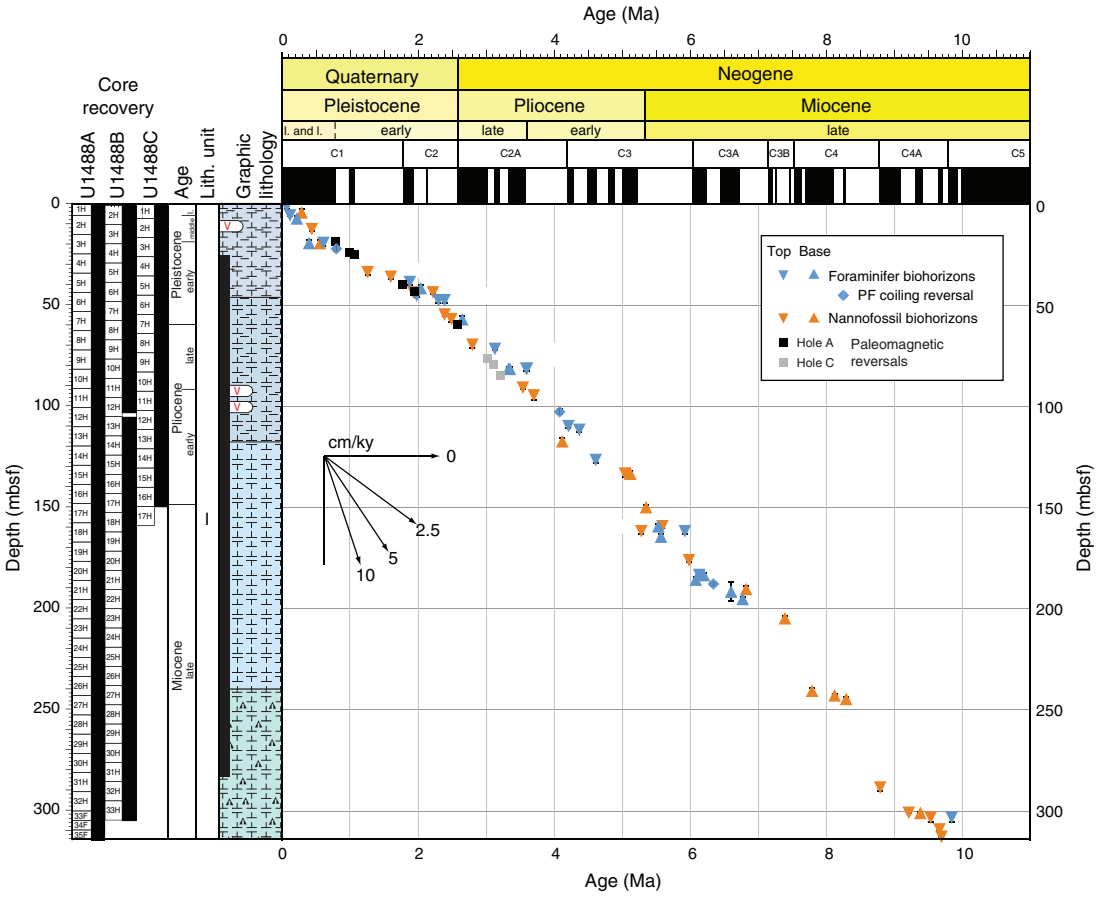

C/N ratio is low, suggesting that the majority of the organic matter is derived from marine production; however, caution should be taken when interpreting the TOC and C/N records because shipboard TOC values were calculated by the subtraction method.

Site U1489

Background and objectives

Site U1489 (proposed Site WP-04A) is located on the western slope of the southern Eauripik Rise at 02°07.19′N, 141°01.67′E in 3421 m water depth (Figure **F21**). The site is situated on seismic Line RR1313-WP4-2 at the intersection with seismic Line RR1313-WP4-3. The seismic profile shows a continuous succession of hemipelagic, carbonate-rich sediment with basement at >650 mbsf (Rosenthal et al., 2016). Site U1489 is located ~81 km west-northwest of Site U1488 and ~105 km northwest of DSDP Site 62 and shows a similar sedimentary cover (Shipboard Scientific Party, 1971).

Site U1489 is situated on the western slope of the southern part of Eauripik Rise, within the Caroline Basin north of Papua New Guinea (Figure **F3**). The roughly north–south trending Eauripik Rise is an ~250 km wide aseismic ridge that rises ~1–2 km above the surrounding seafloor and separates the East and West Caroline Basins. Magnetic Anomalies C13–C9 in both basins show that ocean crust formed along roughly east–west spreading centers from the Eocene until the late Oligocene. Offsets in these anomalies and the lack of magnetic lineations beneath the Eauripik Rise supports the interpretation that it formed due to excess submarine volcanism along a leaky north–south transform fault (Hegarty and Weissel, 1988.) An alternative interpretation attributes the formation of the Eauripik Rise to the northward passage of a mantle hotspot that contributed to the tectonically and structurally complex region surrounding the Sorol Trough (Bracey, 1975). Seismic refractions show thickened ocean crust beneath the Eauripik Rise, and a small free-air anomaly and positive geoid anomaly indicate a compensated structure reaching deep into the mantle (Hegarty and Weissel, 1988). Although there are no discernible magnetic lineations on the Eauripik Rise, these data and the recovery of tholeiitic basalt at Site 62 (Shipboard Scientific Party, 1971) make it difficult to argue that it is a remnant of ancient continental material. The igneous rocks recovered from the bottom of Site 62 are slightly vesicular and highly altered and contain calcite veins with well-preserved foraminifers and nannofossils. The dolomitization of overlying limestone suggests that these basalts intruded into marine chalk leading to extensive diagenetic reactions near the base of the sedimentary succession.

Site U1489 is located ~2° north of the Equator and is thus suitable for reconstructing the hydrographic history of the WPWP. The comparatively low sedimentation rate at this site, typical of open-ocean environments, allows coring of the middle Miocene at a relatively shallow depth, which was not possible at Site U1488, offering the opportunity to reconstruct the evolution of the WPWP from the MMCO to the middle Miocene climate transition associated

with expansion of the Antarctic ice sheet. At ~3400 mbsl, the site is bathed by modified LCDW and therefore will be useful to monitor past changes in this water mass (Figure **F5A**). Because this site is close to Site U1488 but at ~900 m deeper water depth, comparing results from these two sites also offers the opportunity to investigate potential diagenetic effects of foraminifer geochemical proxy records. High-resolution interstitial water sampling at this site will be used for geochemical reconstructions of the deep Pacific water mass ($\delta^{18}O$, salinity, and seawater chemistry) during the LGM.

Operations

After a 44 nmi transit from Site U1488, the vessel stabilized over Site U1489 at 1442 h on 24 November 2016. Site U1489 was an alternate site that was added during the expedition to complement the record cored at Site U1488. We initially planned to core three holes to 200 mbsf; however, we requested and received permission to core to 5.0 s TWT at our site location on seismic reflection profile Line RR1313 WP4-2. We ultimately cored four holes at Site U1489 (Table **T1**). Hole U1489A consisted of a single full APC core, which indicated we missed the mudline. Hole U1489B was cored with the APC system to 129.2 mbsf. We terminated coring in this hole because of coring difficulties that resulted in poor recovery and core disturbance. Hole U1489C was cored to 385.6 mbsf using a combination of APC, HLAPC, and XCB coring, and Hole U1489D was cored with the APC system to 127.2 mbsf, drilled without coring to 274.0 mbsf, and then cored with the XCB system to 385.6 mbsf.

Hole U1489A was cored with the APC system using orientation and nonmagnetic hardware. Core 1H recovered a full core barrel, indicating that we had missed the mudline, so we terminated coring. We collected 9.53 m of core over 9.5 m of coring (100% recovery) in Hole U1489A.

Hole U1489B was cored to 129.2 mbsf with the APC system using orientation and nonmagnetic hardware (Cores 1H through 14H). Downhole formation temperature measurements using the APCT-3 were taken on Cores 4H (34.2 mbsf), 7H (62.7 mbsf), 10H (91.2 mbsf), and 12H (110.2 mbsf); however, only one measurement was of good quality (Core 10H). The measurements taken while collecting Cores 4H and 7H showed possible movement related to heavy seas, and the measurement from Core 12H was of very poor quality. We also collected high-resolution interstitial water samples at a frequency of one (5–10 cm) whole-round sample per section over the entire cored succession in Hole U1489B. Coring difficulties included premature failure of the APC shear pins due to ship motion on Cores 3H and 8H, as well as one core with no recovery (Core 11H) and two cores requiring a second coring attempt to retrieve sediment (Cores 12H and 13H). As these cores appeared very disturbed, we opted to terminate coring in Hole U1489B. We collected 120.66 m of core over 129.2 m of coring (93% recovery) in Hole U1489B.

Hole U1489C was cored to 269.5 mbsf (Cores 1H through 29H) with the APC using orientation and nonmagnetic hardware. Core 29H required drillover to extract it from the formation, indicating APC refusal. We switched to the HLAPC system and cored only to 278.9 mbsf (Cores 30F and 31F) before excessive overpull indicated HLAPC refusal. We then switched to the XCB system to core to 385.6 mbsf (Cores 32X through 42X), where we terminated coring. We collected 376.35 m of core over 385.6 m of coring (98% recovery) in Hole U1489C.

Hole U1489D was cored to recover material for the splice over the upper ~120 mbsf interval that was heavily sampled for interstitial water in Hole U1489B and to collect a second copy of the deeper succession at Site U1489. Hole U1489D was cored with the APC system using orientation and nonmagnetic hardware to 127.2 mbsf (Cores 1H through 14H). Because several of the APCT-3 measurements provided spurious results in Hole U1489B, we opted to take additional measurements in Hole U1489D while collecting Cores 4H (32.2 mbsf), 7H (60.7 mbsf), 10H (89.2 mbsf), and 13H (117.7 mbsf). All four measurements provided good results. We drilled without coring from 127.2 to 274.0 mbsf and then cored using the XCB system to 385.6 mbsf (Cores 16X through 27X), where we terminated coring. We collected 229.24 m of core over 238.8 m of coring (96% recovery) in Hole U1489D.

Operations at Site U1489 ended at 0212 h on 30 November . Total time spent at Site U1489 was 131.5 h (5.5 days). We collected a total of 58 APC cores, recovering 527.85 m of core over 535.4 m of coring (98.6% recovery). We also collected 2 HLAPC cores, recovering 9.05 m of core over 9.4 m of coring (96.3% recovery) and 23 XCB cores, retrieving 198.88 m of core over 218.3 m of coring (92.6% recovery). In total, we collected 735.78 m of sediment over 763.1 m of coring (96.4% recovery).

Principal results

The recovered sedimentary succession at Site U1489 consists of ~386 m of lower Miocene to recent nannofossil ooze and chalk with varying proportions of clay (Figure **F24**). Biosilica (mainly radiolarians) is a major component in the lowermost part of the site. The recovered succession at Site U1489 is assigned to one lithologic unit divided into two subunits. Subunit IA consists of ~280 m of upper Miocene to recent light greenish gray foraminifer-bearing clay-rich nannofossil ooze and white clay-bearing foraminifer-rich nannofossil ooze, with clay content decreasing downhole. Color alternations occur at the centimeter to meter scale and also include thinly bedded pale yellow sediment. Grayish green and pale purple laminae are common in the upper part of Subunit IA. Soft-sediment deformation is a prominent feature in the lower part of Subunit IA (between ~100 and 260 mbsf) and is characterized by a series of large-scale soft-sediment deformation intervals intercalated with pelagic sediment. These intervals occasionally include coarse-grained foraminifer ooze or very thickly bedded homogeneous clay-bearing foraminifer-rich nannofossil ooze. Subunit IB consists of ~112 m of lower to upper Miocene light greenish gray foraminifer-bearing clay-rich chalk. Near the base of the subunit, biosilica becomes more abundant and the sediment transitions to pale yellow foraminifer-bearing radiolarian-rich chalk and light gray radiolarian-rich chalk. This subunit also shows color alternations between lighter and darker chalk, as well as minor soft-sediment deformation features. There is an abrupt change to white chalk at the very base of the succession.

Calcareous microfossil assemblages and preservation are typical of a pelagic, relatively deepwater bathyal environment throughout Site U1489. Foraminifer preservation is generally good to very good in the upper part of the succession (Subunit IA) but is moderate to poor in the chalk of Subunit IB. Calcareous nannofossil preservation also decreases with depth, although this is most prevalent in the discoasters, which show significant overgrowth in the chalk. The planktonic/benthic foraminifer ratio is on the order of 99:1 and the benthic foraminifers *P. wuellerstorfi* and *Cibicidoides mundulus* are present in most of the samples examined throughout the hole. Other common taxa include *Laevidentalina* spp.

Integrated calcareous nannofossil and planktonic foraminifer biostratigraphy generally shows excellent congruence between both

Figure F24. Site U1489 results summary. cps = counts per second.

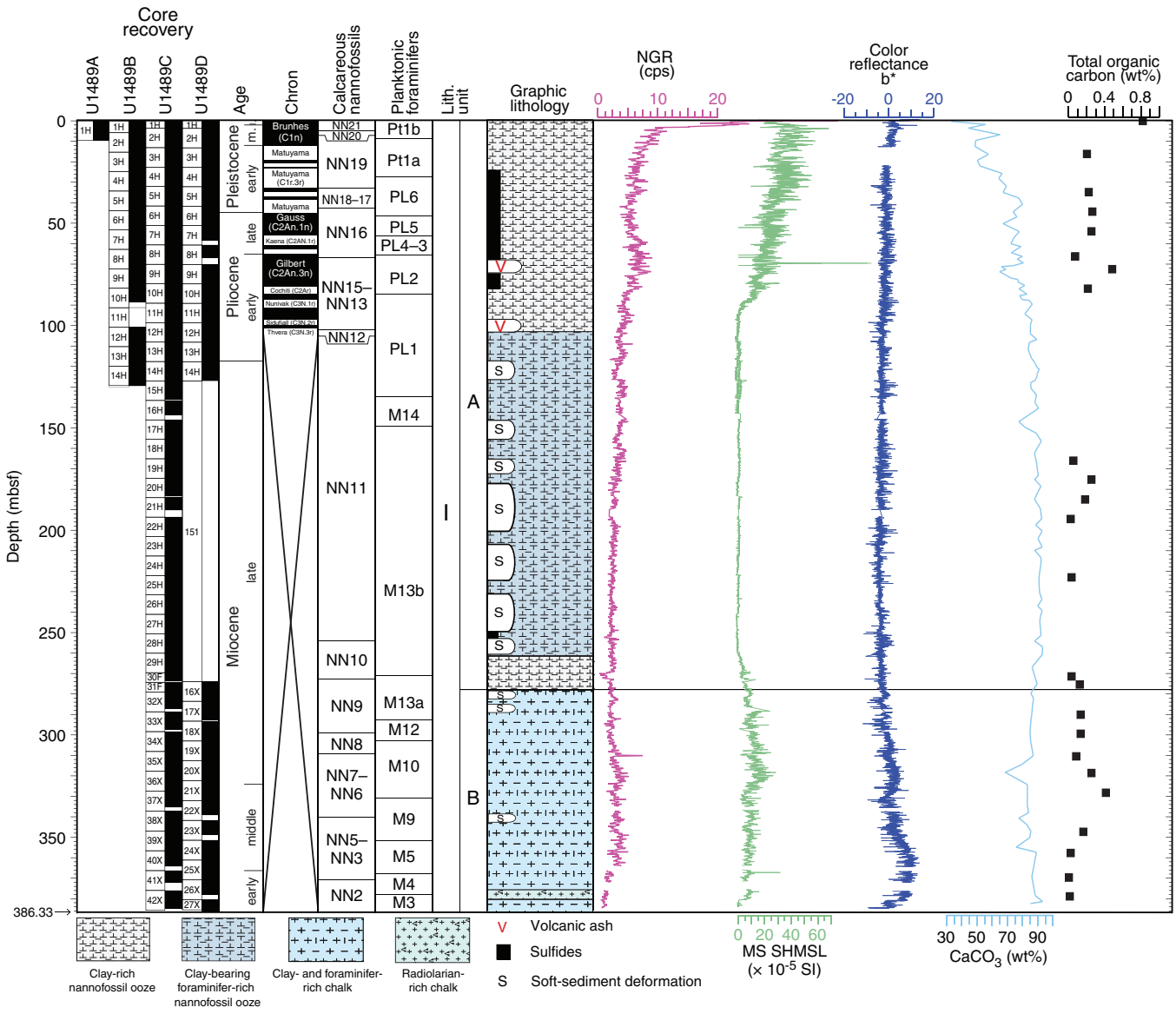

fossil groups and the magnetostratigraphy (Figure **F25**). The age at the base of the succession is constrained to the early Miocene based on the biohorizon base *Sphenolithus belemnos* at ~380 mbsf and the presence of *Dentoglobigerina binaiensis* and absence of *Globigerinoides altiaperturus* and *Tenuitella munda* at ~384 mbsf. The Miocene/Pliocene boundary is placed at ~115 mbsf, above the biohorizon base *C. armatus*. The Pliocene/Pleistocene boundary is located at ~45 mbsf based on the biohorizon top *D. surculus* and the Gauss/Matuyama boundary (Figure **F24**). Long-term average sedimentation rates through the early to middle Miocene were low (~0.3 cm/ky). Average sedimentation rates in the late Miocene increased to ~2 cm/ky. In the latest Miocene and earliest Pliocene, average sedimentation rates increased to ~5 cm/ky; however, this interval is complicated by soft-sediment deformation, and the estimated sedimentation rate is based on sparse bioevents (and no magnetostratigraphic reversal events). Above this interval of deformed sediment, Pliocene and Pleistocene sedimentation rates average ~2 cm/ky (Figure **F25**), which is comparable to those of the late Miocene at Site U1488.

Paleomagnetic investigations at Site U1489 involved measurement of the NRM of archive-half sections from Holes U1489A–U1489D before and after demagnetization in a peak AF of 15 mT. Corrected declination is largely coherent between cores; however, absolute values in Hole U1489B cluster around 90° for periods of normal polarity and around 270° for reversed polarity, with the opposite being true (270° for normal polarity and 90° for reverse polarity) in Holes U1489C and U1489D. Relatively soft ferrimagnetic minerals are concentrated in the uppermost ~90 mbsf. Between ~90 and 100 mbsf, NRM_{15mT}, magnetic susceptibility, and SIRM values decrease, and deeper than ~100 mbsf, average magnetic susceptibility, NRM_{15mT}, and SIRM values are ~1–2 orders of magnitude lower than in the upper ~90 mbsf and often approach the noise level of their respective instruments, indicating a significant reduction in magnetic mineral concentration deeper than ~100 mbsf. We identify as many as twenty-two 180° shifts in declination in Holes U1489B–U1489D (Figure **F25**). The Matuyama/Brunhes boundary (0.781 Ma) is placed at ~15 mbsf, the Gauss/Matuyama boundary (2.581 Ma) at ~45 mbsf, and the Gilbert/Gauss boundary (3.596

Figure F25. Age-depth plot for Site U1489 showing integrated biomagnetochronology for Hole U1489C. The stratigraphy of the base of Hole U1489C is constrained by biohorizon base *Sphenolithus belemnos* (19.03 Ma) and by the presence of *Dentoglobigerina binaiensis* (>19.30 Ma) and absence of *Globigerinoides altiaperturus* (>20.03 Ma) and *Tenuitella munda* (<20.78 Ma) at ~380 mbsf. Average sedimentation rates varied from ~0.3 to 5 cm/ky.

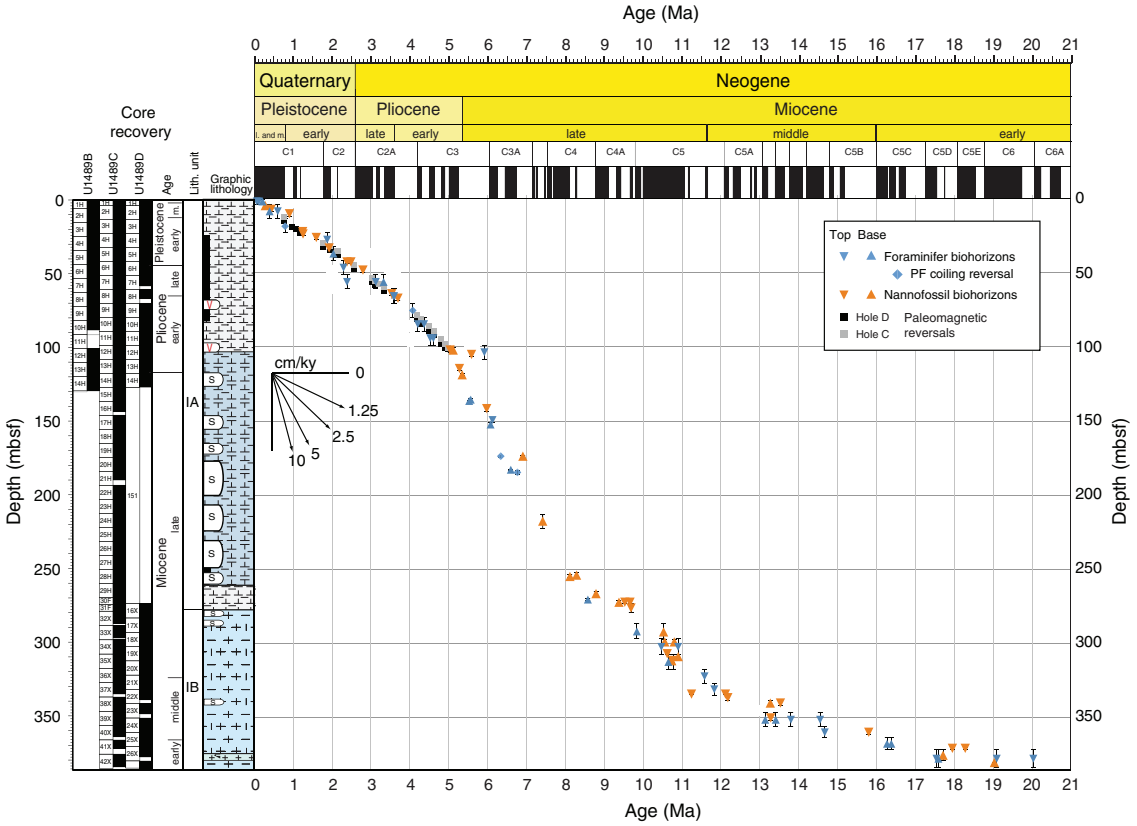

Ma) at ~65 mbsf. The deepest of these declination shifts is identified as the upper boundary of the Thvera normal (C3n.3r; 4.997 Ma) at ~101 mbsf (Figure **F24**).

All physical property measurements are generally reproducible across holes with the exception of some intervals in Hole U1489B that are likely due to core disturbance during recovery. GRA bulk density increases downhole from ~1.3 to 1.8 g/cm^3, with an increase in variability deeper than 270 mbsf caused by an increase in sediment induration coincident with the switch to XCB coring. Magnetic susceptibility values are relatively high (~20 × 10^{-5} to 60 × 10^{-5} SI) in the upper 90 mbsf, with distinct cyclicity that transitions from the 1–3 m scale to the 0.4–0.6 m scale at 21 mbsf. Magnetic susceptibility values between 90 and 260 mbsf are extremely low (<3 × 10^{-5} SI) in the light-colored sediment but increase to a mean of ~9 × 10^{-5} SI between 260 and 385 mbsf (Figure **F24**). NGR deceases rapidly from 30 to 10 counts/s over the upper 5 mbsf and then gradually decreases to <1 count/s by the bottom of the site (~385 mbsf). Two intervals of slightly higher NGR between 55 and 84 mbsf and between 310 and 360 mbsf correspond to higher clay content in the sediment. In general, the short-term cyclicity in magnetic susceptibility and NGR coincide with light–dark variations in the sediment. In general, *P*-wave velocity values increase slightly and increase in variability with depth. Discrete MAD bulk density is offset by ~0.05 g/cm^3 in the uppermost 265 mbsf compared with GRA bulk density. Below 265 mbsf, where the sediment became indurated and XCB coring commenced, the variability of GRA bulk density increases and the MAD bulk density values correspond well with the highest GRA bulk density values. Thermal conductivity increases with depth from ~0.9 to 1.3 W/(m·K), similar to the trend seen in the MAD bulk density and dry density, which is likely primarily due to compaction. Downhole formation temperatures were measured in both Holes U1489B and U1489D because the APCT-3 tool showed evidence of movement in some of the measurements taken in Hole U1489B. The more reliable measurements from Hole U1489D confirm the results from Hole U1489B and indicate a geothermal gradient of 31°C/km.

Stratigraphic correlations between holes at Site U1489 primarily used WRMSL magnetic susceptibility data and were aided by additional whole-round measurements of GRA bulk density, *P*-wave velocity, NGR, and L* measured on split cores. Overlap between holes provided two continuous spliced intervals from 0 to 140.95 m CCSF and from 305.70 to 371.25 m CCSF. The interval between these spliced sections corresponds to the interval of soft-sediment deformation in the lower part of Subunit IA that was cored only once. Gaps between an additional five cores deeper than 371.25 m CCSF in both Holes U1489C and U1489D prevented the construction of a deeper continuous spliced section.

A total of 100 whole-round samples and one mudline sample were collected for interstitial water analysis at Site U1489: 69 samples from Hole U1489B and 32 from Hole U1489C. Because of coring problems and sediment disturbances deeper than ~90 mbsf in Hole U1489B, interstitial water sampling resumed at 88 mbsf in Hole U1489C and continued to the bottom of the hole (381.8 mbsf). Small but nonetheless significant offsets are observed in downhole profiles between the two holes, particularly for Cl, PO_4, K, and B, and should be accounted for in future interpretations of the intersti-

tial water profiles. High-resolution sampling was conducted in the upper ~130 mbsf at this site with the goal of reconstructing the Cl concentration and $\delta^{18}O$ of LCDW during the LGM. Preliminary shipboard chlorinity measurements suggest that reconstruction of the salinity of LCDW will be possible with the samples collected at this site.

Carbonate diagenesis and minor amounts of organic matter remineralization are the dominant controls on the interstitial water chemistry, along with upward diffusion from a deep fluid source. Muted trends in Ca, Mg, and Li suggest a weaker influence of deep fluids at this site relative to Site U1488, with chemistry reflective of basalt–seawater interaction. Differences in basement age and sediment thickness between the two sites likely contribute to the observed differences. Calcium carbonate content averages 82 wt% and increases with depth from ~50 wt% near the seafloor to >90 wt% at ~175 mbsf (Figure **F24**). TOC is low (average = ~0.14 wt%) and varies between 0 and 0.8 wt% (Figure **F24**), which is reflected in the moderate degree of SO_4 depletion and low concentrations of Br, NH_4, and PO_4. Nitrogen was detected in trace amounts.

Site U1490

Background and objectives

Site U1490 (proposed Site WP-02A) is located on the northern edge of the Eauripik Rise at 05°48.95′N, 142°39.27′E in 2341 m water depth (Figure **F21**). The site is situated on seismic Line RR1313-WP2-1 ~3.6 km east of the intersection with seismic Line RR1313-WP2-6. The seismic profile shows a continuous succession of hemipelagic, carbonate-rich sediment. At Site U1490, horizontally bedded layers continue downsection to ~0.07 s TWT below the seafloor, where reflector geometry shows a dramatic change in depositional processes. From ~3.26 to ~3.60 s TWT, an apparently uninterrupted accumulation of current-controlled mud waves occurred, with the exception of a possible break at 3.27 s TWT (Rosenthal et al., 2016). Other MCS lines in the survey grid surrounding Site U1490 show these features as well. The wavelengths are ~1 km and oriented southwest–northeast (perpendicular to seismic Line RR1313-WP2-1), with 15–18 m maximum amplitude that gradually decreases upsection, possibly reflecting a several million–year record of current-controlled bedforms (Baldwin et al., 2017).

Site U1490 is located ~431 km north of Site U1488 at the northern end of the Eauripik Rise (Figure **F21**), where it terminates in a tectonically complex region that includes the Sorol Fault, Sorol Trough, and Caroline Ridge (Hegarty and Weissel, 1988). The roughly north-south–trending Eauripik Rise is an ~250 km wide aseismic ridge that rises ~1–2 km above the surrounding seafloor and separates the East and West Caroline Basins. Magnetic Anomalies C13–C9 in both basins show that ocean crust formed along roughly east–west spreading centers from the Eocene until the late Oligocene. Offsets in these anomalies and the lack of magnetic lineations beneath the Eauripik Rise support the interpretation that it formed as a result of excess submarine volcanism along a leaky north–south transform fault (Hegarty and Weissel, 1988.) An alternative interpretation attributes the formation of the Eauripik Rise to the northward passage of a mantle hotspot that contributed to the tectonically and structurally complex region surrounding the Sorol Trough (Bracey, 1975).

Site U1490 is located ~6° north of the Equator and is therefore suitable for reconstructing the hydrographic history of the northern part of the WPWP. The comparatively low sedimentation rate at this site (~1 cm/ky) will be used along with the record from Site U1488 to reconstruct the evolution of the WPWP since the Miocene. At ~2300 mbsl, the site is bathed by modified UCDW and therefore may be used to monitor past changes in this water mass (Figure **F5A**).

Operations

After a 242 nmi transit from Site U1489, the vessel stabilized over Site U1490 at 0000 h on 1 December 2016. The original operations plan at Site U1490 called for two advanced piston corer (APC) holes to 250 mbsf and a third APC hole to 150 mbsf. With ~2 days of contingency remaining, we opted to deepen Hole U1490A to XCB refusal (382.8 mbsf), core Hole U1490B to HLAPC refusal (292.9 mbsf), and then use the remaining time to core as deeply as possible in Hole U1490C (170.0 mbsf) (Table **T1**).

Hole U1490A was cored to 251.2 mbsf (Cores 1H through 27H) with the APC using orientation and nonmagnetic hardware. Downhole formation temperature measurements using the advanced piston corer temperature tool (APCT-3) were taken on Cores 4H (32.7 mbsf), 7H (61.2 mbsf), 10H (89.7 mbsf), 13H (118.2 mbsf), and 16H (146.7 mbsf), with some movement detected on two of the runs (Cores 4H and 10H). Cores 25H through 27H experienced excessive overpull and required drillover to extract them from the formation, indicating APC refusal. We switched to the HLAPC system and continued coring to 270.0 mbsf (Cores 28F through 31F), where excessive overpull and drillover indicated HLAPC refusal. We then cored with the XCB to 376.7 mbsf (Cores 32X through 42X). While cutting Core 43X, the rate of penetration slowed dramatically, so we retrieved the core after only a 5.6 m advance. The XCB cutting shoe showed extensive wear, and a small amount of chert was recovered in the bottom of the core. Core 44X advanced only 0.5 m over 45 min, so we terminated coring at 382.8 mbsf. No core was recovered, and the XCB cutting shoe had lost all of its carbide teeth. We collected 367.35 m of core over 382.8 m of coring (96% recovery) in Hole U1490A.

Hole U1490B was cored with the APC system using orientation and nonmagnetic hardware to 228.0 mbsf (Cores 1H through 25H). Core 25H required drillover to extract it from the formation, and the core liner had to be pumped out of the core barrel. We switched to the HLAPC and continued to core to 262.9 mbsf (Cores 26F through 33F). We terminated coring in Hole U1490B when Core 33F required drillover. We retrieved 267.60 m of core over 258.9 m of coring (103% recovery) in Hole U1490B.

Hole U1490C was cored with the APC system using orientation and nonmagnetic hardware to 170 mbsf (Cores 1H through 20H). Coring was terminated when a ground fault was detected in the top drive motor that could not be repaired within the amount of time remaining for coring operations (~18 h). The drill bit was pulled clear of the seafloor at 1017 h on 5 December and retrieved to the rig floor. The vessel was secured for transit, and we departed for Guam at 0542 h on 6 December, ending operations at Site U1490.

A total of 125.75 h (5.2 days) was spent at Site U1490. We collected 69 APC cores, recovering 662.07 m of core over 641.2 m of coring (103.3% recovery) and 11 HLAPC cores, retrieving 53.7 m of core over 51.7 m of coring (103.9% recovery). We also collected 13 XCB cores, recovering 87.42 m of core over 112.8 m of coring (77.5% recovery). Overall core recovery for Site U1490 was 803.19 m of sediment over 805.7 m of coring (99.8% recovery).

Transit to Guam

The 485 nmi transit from Site U1490 to Guam was completed in 49.0 h at an average speed of 9.9 kt. The pilot boarded the vessel at

0600 h on 8 December 2016. Expedition 363 ended with the first line ashore at the Port of Guam at 0648 h.

Principal results

We recovered an ~380 m sequence of upper Oligocene to recent sediment that contains calcareous microfossils (mainly nannofossils and foraminifers), siliceous microfossils (radiolarians, diatoms, and sponge spicules), clay minerals, and volcanic ash. The sediment is assigned to one unit divided into three subunits based primarily on downhole variations in biosilica, clay minerals, and ash (Figure **F26**). Subunit IA (~185 m thick) includes a sequence of upper Miocene to recent foraminifer-rich nannofossil ooze with variable but generally low amounts of clay. Coarser, decimeter-thick layers dominated by foraminifer ooze are also present. In Subunit IB (late early to early late Miocene; ~78 m thick), clay minerals become a significant component of the sediment, and their abundance increases downhole. The primary lithology in Subunit IB is clay-rich foraminifer-nannofossil ooze. Biosilica (mainly sponge spicules and radiolarians) is also one of the sediment constituents of this subunit. Subunit IC is ~124 m thick and was deposited during the late Oligocene to the middle Miocene. The uppermost ~10 m of this subunit is composed of greenish radiolarian-rich nannofossil ooze, whereas the remainder is radiolarian-rich chalk. Discrete, dark gray to black partially indurated layers and nodules and indurated rock fragments (chert) are exclusively found in this subunit. The number, thickness, and degree of induration of these layers increase downhole. Siliceous particles, either volcanic glass and/or biosilica (radiolarians, sponge spicules, and diatoms), are the dominant lithologic component of these layers, although calcareous components are also occasionally present.

Calcareous nannofossils and planktonic foraminifers are present throughout the ~380 m sequence recovered at Site U1490. Planktonic foraminifer preservation is very good to good for most of the succession, although it decreases to moderate to poor in the chalk of Subunit IC, whereas calcareous nannofossil preservation is moderate through most of the succession. Benthic foraminifers indicate a deepwater environment, and the planktonic/benthic foraminifer ratio is ~99:1 throughout the succession. The assemblages are similar to those from other Eauripik Rise sites (U1488 and U1489). The most common species are *Laevidentalina* spp., *P. wuellerstorfi*, and *Oridorsalis umbonatus*.

Calcareous nannofossil and planktonic foraminifer biostratigraphy indicates that the recovered succession spans the latest Oligocene to recent (Figure **F27**). A series of paleomagnetic reversals identified in the lower and middle Miocene interval correlate well with the biostratigraphic datums. There is no evidence of hiatuses, but the uppermost ~40 m of the site is complicated because of reworking of calcareous nannofossil and planktonic foraminifer marker species. The age at the base of the succession is constrained to ~24 Ma based on extrapolation through Oligocene/Miocene boundary biohorizons and the presence of common *Cyclicargolithus abisectus* (~24 Ma) at the base of the hole. The Oligocene/Miocene boundary is placed at ~340 mbsf based on the presence of *Sphenolithus delphix*. The Miocene/Pliocene boundary is located at ~90 mbsf between the biohorizon bases *C. cristatus* and *C. armatus*, and the Pliocene/Pleistocene boundary is approximated by the biohorizon top *D. surculus* at ~35 mbsf (Figure **F26**). The sedimentation rate appears to have been near constant for long periods, separated by four inflection points at 3.60, 5.33, 9.11, and 22.25 Ma, the last three of which correspond to marked changes in lithology. Average sedimentation rates were ~4.7 cm/ky in the latest Oligocene, ~0.88 cm/ky in the early and middle Miocene, 1.57 cm/ky in the late Miocene, 2.9 cm/ky in the early Pliocene, and 1.4 cm/ky in the late Pliocene and Pleistocene (Figure **F27**).

Paleomagnetic investigations at Site U1490 involved measurement of the NRM of archive-half sections from Holes U1490A–U1490C before and after demagnetization in a peak AF of 15 mT. We measured the entire sediment succession in Hole U1490A but ceased measurement between ~36 and 161.5 mbsf in Hole U1490B and below ~31 mbsf in Hole U1490C because data quality decreased and became increasingly uninterpretable. Corrected declination is largely coherent between cores; however, absolute values in Holes U1490A and U1490B cluster around 270° for periods of normal polarity and around 90° for reversed polarity. For Hole U1490C, no baseline offset was observed and corrected declination during intervals of normal polarity cluster around 0°/360° and 180° for reversed polarity. In the upper ~16 mbsf, WRMSL magnetic susceptibility data and discrete magnetic susceptibility and SIRM values suggest moderately low (ferri)magnetic mineral concentration. Between ~16 and 175 mbsf, average magnetic susceptibility data decrease to negative values, associated with the diamagnetic properties of carbonate that dominate the sediment and an almost complete absence of ferrimagnetic minerals. Below ~168 mbsf, discrete magnetic susceptibility data and SIRM begin to steadily increase, a change associated with greater proportions of clay and ash in the sediment. We identify fifty distinct ~180° shifts in declination in Holes U1490A–U1490C (Figure **F27**). We observe five reversals in the youngest part of the succession, including the Matuyama/Brunhes boundary at ~8 mbsf. Deeper than ~170 mbsf, we observe 45 geomagnetic reversals with an almost complete record from the upper boundary of C4An (8.771 Ma; ~171 mbsf) to the upper boundary of C6n (18.748 Ma; ~263 mbsf) in Hole U1490B (Figure **F26**).

All physical property measurements are generally reproducible among the three holes at Site U1490. GRA and discrete sample (MAD) bulk density generally agree well in terms of long-term trends and short-term variability. The upper 3 mbsf is characterized by the transition away from the mudline, with a rapid increase in GRA bulk density and a decrease in NGR (Figure **F26**). GRA bulk density linearly increases from ~1.6 g/cm^3 at the top of the hole to ~1.9 g/cm^3 at 230 mbsf, a change related to increased compaction with depth. Magnetic susceptibility is extremely low between 20 and 180 mbsf with an average value around -0.8×10^{-5} SI that corresponds to light-colored sediment with high carbonate content (nannofossil ooze). Magnetic susceptibility increases to ~7×10^{-5} SI, and *P*-wave velocity increases from ~1500 to ~1700 m/s at ~180 mbsf, coincident with increased clay content in Subunit IB. Between 230 and 270 mbsf, a second transition is evident in all of the physical properties, with GRA bulk density decreasing from ~1.9 to ~1.7 g/cm^3, which coincides with the highest peaks in magnetic susceptibility, with values up to 20×10^{-5} SI. A broad magnetic susceptibility maximum with values up to ~330×10^{-5} SI is concurrent with the first major peak of ~8 counts/s in NGR at ~255 mbsf, which coincides with an indurated ash layer. Deeper than 270 mbsf (Subunit IC), we observe a general increase in the short-term variability of all physical properties, with values ranging from 1.5 to 1.9 g/cm^3 for GRA bulk density, an increase in average magnetic susceptibility to ~10×10^{-5} SI with peaks frequently reaching ~200×10^{-5} to 300×10^{-5}, NGR values frequently reaching ~4 counts/s and occasionally reaching ~15 counts/s in the volcanogenic-rich dark layers, and an

Figure F26. Site U1490 results summary. cps = counts per second.

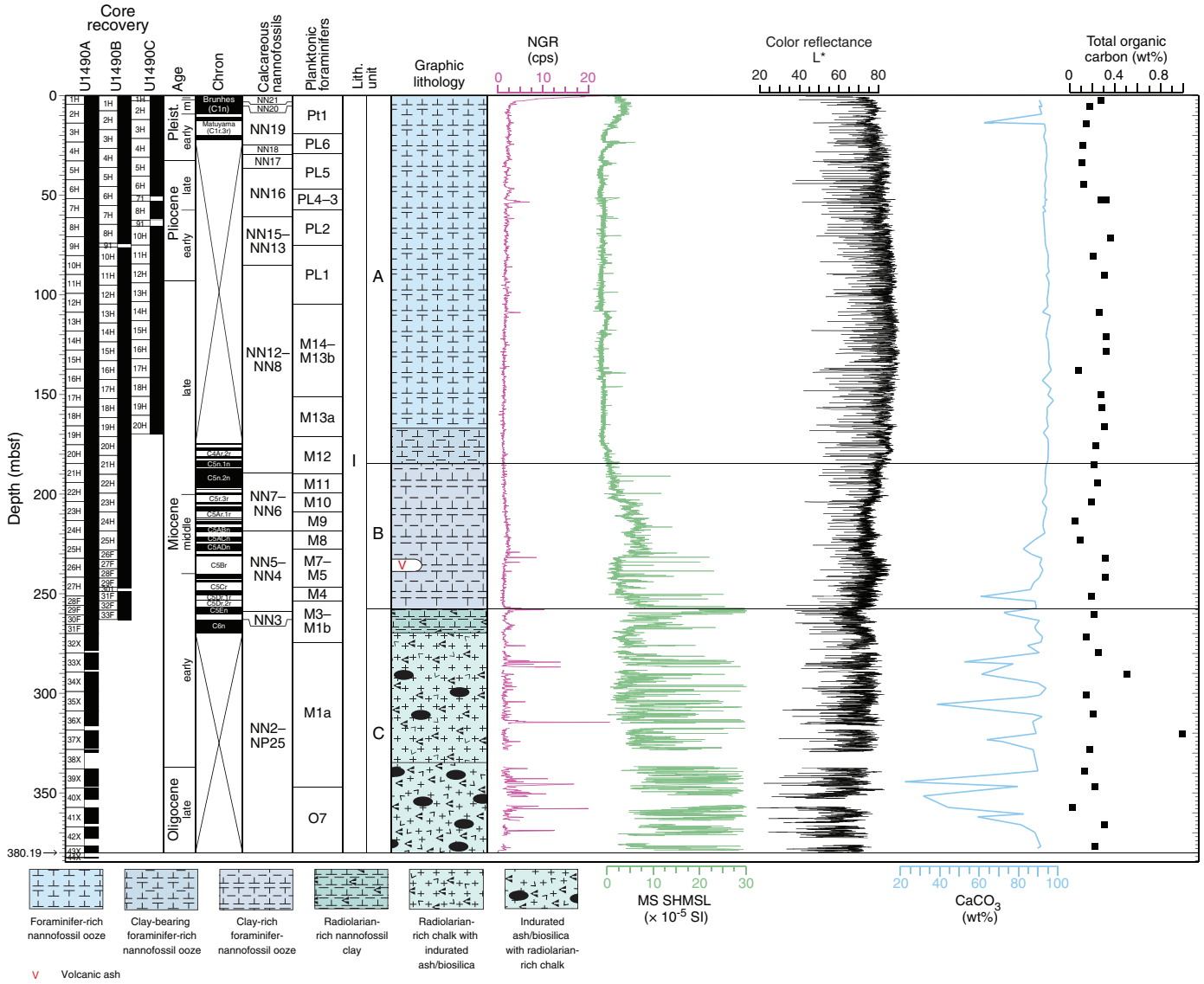

increase in *P*-wave velocity from ~1540 to ~1960 m/s. This large variability is also observed in dry density, grain density, porosity, and thermal conductivity. This interval is associated with the presence of black layers consisting of silica mixed with volcanogenic material, which become more indurated downhole.

Stratigraphic correlation between holes at Site U1490 primarily used Section Half Multisensor Logger (SHMSL) color reflectance data, mainly redness (a*) and luminosity (L*), as well as WRMSL magnetic susceptibility data. In addition, we used WRMSL GRA bulk density and NGR data. We constructed a splice for the entire site using all three holes. The splice is continuous and well constrained from 0 to 295.95 m CCSF, with the exception of one gap at 258.01 m CCSF. A few tentative tie points should be verified during postcruise research.

A total of 36 whole-round samples and one mudline sample were collected from Hole U1490A for interstitial water geochemical analyses, spanning from 0 to 326 mbsf. Sampling for interstitial water chemistry was halted deeper than 326 mbsf due to biscuiting and subpar recovery of core. The interstitial water profiles at this site indicate relatively weak remineralization of organic matter throughout the sediment column, supported by observations of very low TOC content (0 to 1.0 wt%; average of 0.2 wt%) (Figure **F26**). Low dissolved Fe and Mn concentrations in the shallowest sediment at the site suggest minimal suboxic remineralization of organic matter, and significant SO_4 (>21 mM) is present at depth. High carbonate content (~94 wt%) in the upper 230 mbsf (Figure **F26**) is associated with a dissolved Sr profile, reflecting a moderate degree of carbonate recrystallization and/or dissolution. The interstitial water profiles at Site U1490 are dominated by upward diffusion from a deeper fluid source with a geochemical signature characteristic of basalt– and/or volcanogenic sediment–seawater interaction. Marked depletion of Na and enrichment of Ca at this site suggest a unique deep fluid source and possible compositional variability of underlying basalt along the Eauripik Rise. Lower and more variable carbonate content deeper than 230 mbsf coincides with clay- and radiolarian-rich intervals and the presence of frequent ash layers (Figure **F26**).

Figure F27. Age-depth plot for Site U1490 showing integrated biomagnetochronology for Hole U1490A. An age of ~24 Ma was reached at the base of the sedimentary sequence based on extrapolation through Oligocene/Miocene boundary biohorizons and the presence of common *Cyclicargolithus abisectus* (~24 Ma) at ~382 mbsf. Average sedimentation rates varied from ~0.9 to 5 cm/ky.

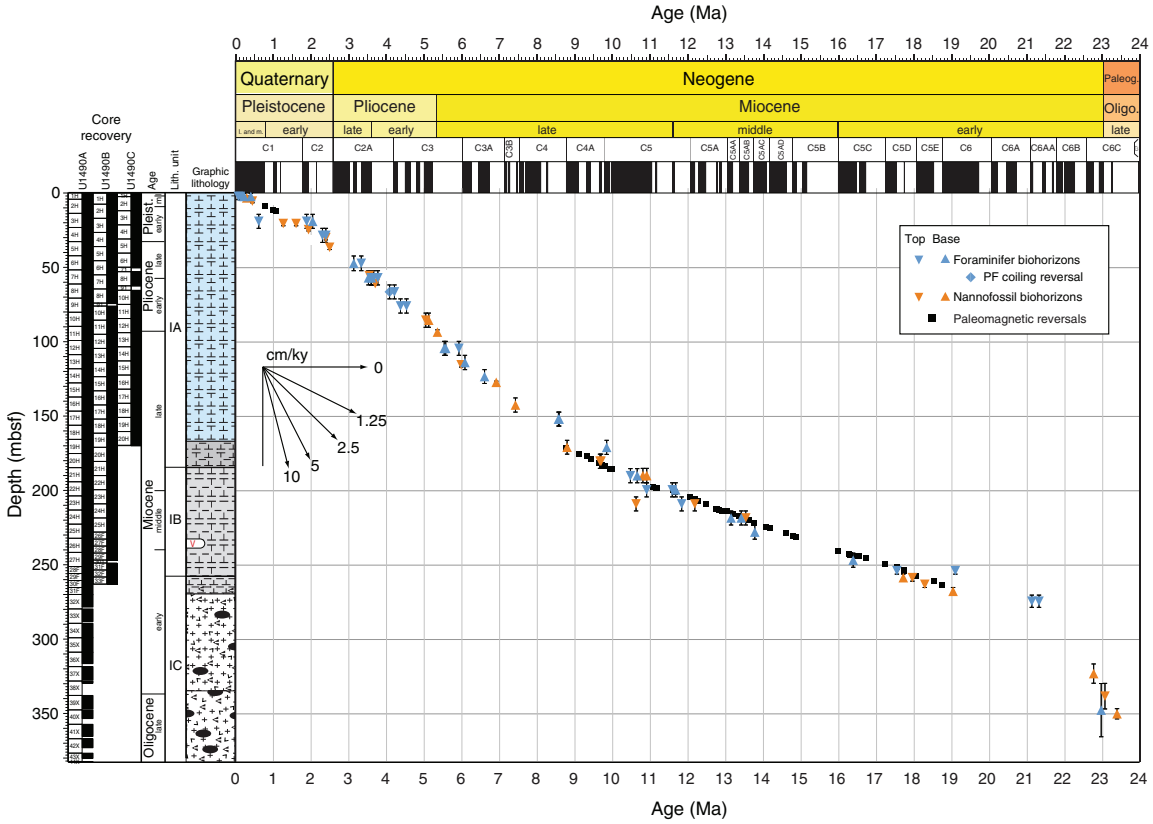

Preliminary scientific assessment

Expedition 363 sought to document the regional expression of climate variability (e.g., temperature, precipitation, and productivity) in the IPWP as it relates to the evolution of Earth's climate from the middle Miocene to late Pleistocene on millennial to geological timescales. To achieve these objectives, we selected sites with a wide geographical distribution and variable depositional environments. The sites are strategically located at the heart of the WPWP, off northern Papua New Guinea and on the Eauripik Rise south of Guam, as well as on its southwestern edge along the northwest margin of Australia to capture the most salient features of the IPWP (Figures **F1**, **F3**). Combining sites with rapidly accumulating sediment at marginal locations and more typical open-ocean sites with relatively low accumulation rates offers the opportunity to trace the Neogene evolution of the IPWP at different temporal resolutions. Furthermore, the large range of water depths (Figure **F5**) allows reconstruction of the thermocline, intermediate, and deepwater contributions from the Northern and Southern Hemisphere to the low-latitude interocean exchange through the ITF, as well as monitoring changes in intermediate and deeper water exchange in response to tectonic- or climate-related processes.

Nine sites were cored during Expedition 363, two in the eastern Indian Ocean off northwest Australia and seven in the WPWP (Figures **F1**, **F3**). We recovered an IODP record totaling 6956 m of sediment in 875–3421 m water depth with an average recovery of 101.3% during 39.6 days of on-site operations (Table **T1**). Most of the sites were cored primarily using the APC system until refusal, which was generally encountered between 250 and 350 mbsf (Figure **F4**). One hole on the northwest Australian margin (U1482C) was cored and logged to 534 mbsf. The total expedition recovery is substantially more than the original primary operations plan, which targeted sediment recovery of 6015 m at seven sites and downhole logging at one site (Rosenthal et al., 2016). Potential security risks in Mindanao, Philippines, precluded us from conducting operations at proposed Site WP-09A in the Davao Bay, offshore South Mindanao; instead, we followed the alternate operations plan that included drilling several additional sites in the WPWP. Two alternate sites at distal locations, proposed Site WP-13A on the Benham Rise (near DSDP Site 292) and proposed Site WP-15A on the Ontong Java Plateau (at the location of ODP Site 806), were not cored due to time limitations. Overall, clement weather and smooth seas allowed for speedy transits to drilling locations, and there was no significant loss of operational time due to mechanical breakdown or equipment damage.

Our scientific objectives required a wide spatial distribution of IPWP climate records with variable sedimentation rates in a variety of geologic settings. Sites U1482 and U1483 are adjacent to some of the world's oldest preserved in situ ocean crust, just seaward of the continental slope of northwest Australia. Sites U1484 and U1485 are in a fore-arc region south of the New Guinea Trench. Sites U1486 and U1487 are on upper Pliocene ocean crust of the adjacent Manus Basin in the northern Bismarck Sea. Sites U1488, U1489, and U1490 are located on upper Oligocene ocean crust of the Caroline microplate (Figure **F28**). The high quality of cores recovered, as well as the extensive documentation of the geologic, biostratigraphic, paleomagnetic, and geochemical background (Figures **F29**, **F30**, **F31**, **F32**, **F33**, **F34**) and the excellent to good preservation of

Figure F28. A. Bathymetric map with locations of sites (red circles) cored during Expedition 363. B. Regional tectonic setting. Locations of volcanoes (red triangles) from **http://volcano.si.edu**. Bathymetry from **http://topex.ucsd.edu/marine_topo**. Blue lines = strike-slip faults, green lines = extensional faults, black lines = unknown fault type. Large black triangles = subduction zones, small black triangles = thrusts. Maps courtesy of Robert Hall.

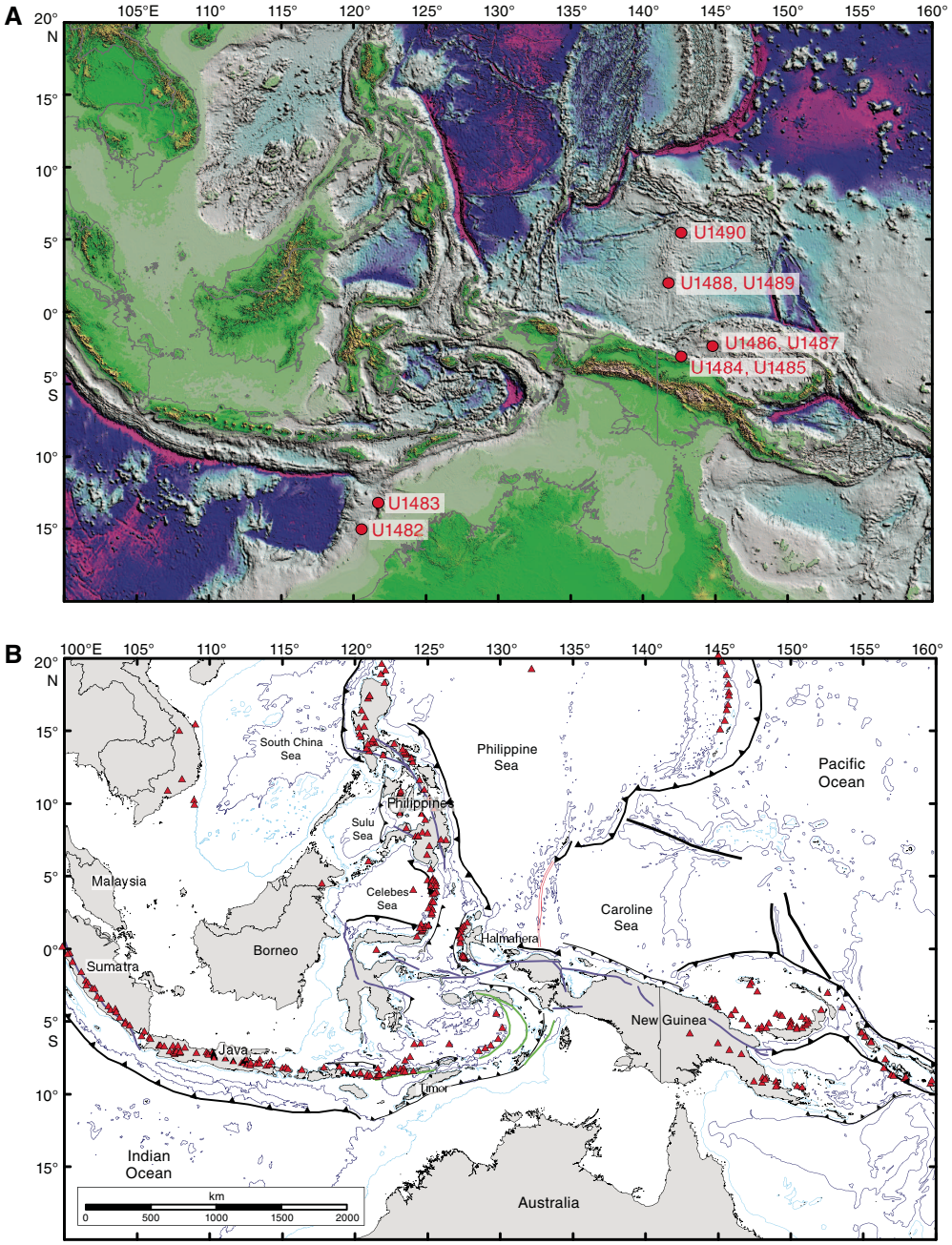

foraminifer shells and calcareous nannofossils at most sites (Figure **F35**), will allow us to meet and even exceed all of the expedition's primary objectives.

Primary objectives

1. *Investigate millennial-scale climate variability in the WPWP.*

Sites U1484 and U1485 are located ~15 and 19 km, respectively, offshore of the northern coast of Papua New Guinea (Figure **F12**) in relatively shallow water depths (1030 and 1145 mbsl, respectively). The proximity to land and to the Sepik/Ramu River mouths results in high sedimentation rates exceeding 50 cm/ky, making the sites suitable for investigating Holocene and late to middle Pleistocene centennial- to millennial-scale climate variability. Biostratigraphy suggests that ages at Sites U1484 and U1485 extend possibly to ~300 ka and ~500 ka, respectively (Figure **F30**). The sediment primarily consists of nannofossil-rich clay, with interbedded sand and silt layers (Figure **F29**). Postcruise research will investigate the timing and processes responsible for the deposition of sand layers at both sites.

The sediment is rich in organic matter compared with typical pelagic sediment, with wood fragments visible on split core surfaces, and excellent foraminifer preservation (Figure **F35**) will provide the opportunity to reconstruct climate variations with a resolution comparable to that of ice cores, North Atlantic sediment drifts, and Southeast Asian speleothem records. These new records

Figure F29. Lithologic summary of Expedition 363 sites grouped by region. Main lithologic characteristics are displayed along with MS for eight sites and reflectance spectroscopy and colorimetry (RSC) parameter L* for Site U1483. Blue, gray, green, brown, and red colors represent biocarbonate-, clay mineral–, biosilica-, siliciclastic-, and volcanogenic-dominated lithologies, respectively. Boundaries between background-colored fields represent isochrons for late Oligocene to recent subepochs based on shipboard bio- and magnetostratigraphic age models. This figure is available in an **oversized format**.

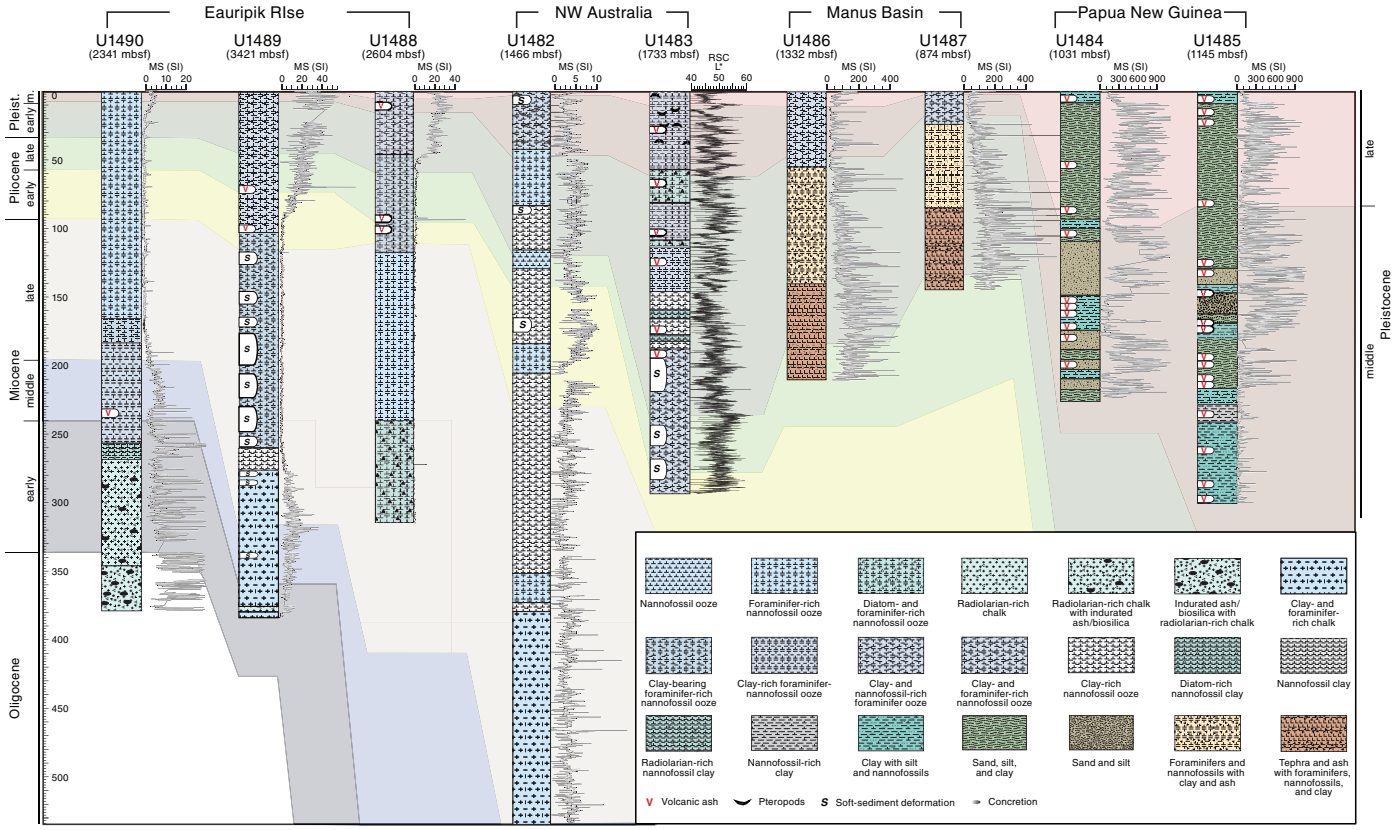

will allow better constraints of the mechanisms influencing millennial-scale variability and its effects on temperature and precipitation in this region. The recovery of high accumulation rate sections from several previous interglacials (e.g., MIS 5e to MIS 13) and glacials offers the possibility to assess whether Holocene trends are typical of previous interglacials with similar orbital forcings or late Holocene climate was already affected by anthropogenic CO_2.

2. *Reconstruct orbital-scale climate variability through the Neogene.*

All sites cored during Expedition 363 resolve orbital-scale variability at moderate to high resolution (Figure **F30**). Site U1483 northwest of Australia and Sites U1486 and U1487 in the Manus Basin provide extended upper Pliocene to recent successions at exceptionally high resolution (6–10 cm/ky) for these regions. Site U1482 northwest of Australia and Sites U1488–U1490 on the Eauripik Rise provide lower resolution records over longer timescales. Sites U1482 and U1488 cover the late Miocene at a resolution of 3–6 cm/ky, whereas Sites U1489 and U1490 extend to the middle and early Miocene, respectively, at a resolution of ~1–2 cm/ky. With excellent recovery, these sites are suitable for detailed paleoceanographic and paleoclimatic reconstructions through the middle Miocene to Pleistocene at orbital and suborbital resolution, comparable with records across the Pacific Ocean and in other ocean basins. Specifically, pairing of northwest Australian sites at the southwestern edge of the IPWP with sites at the heart of the WPWP will allow us to document the spatial pattern of temperature and precipitation variability in the IPWP under different climate background states in relation to changes in radiative forcing (CO_2 and insolation) to better constrain climate sensitivity throughout the Neogene. Spanning a large bathymetric depth range (Figure **F5**), these sites are also suitable for reconstructing changes in intermediate and deepwater properties (e.g., temperature and carbonate chemistry) related to the formation processes of these water masses in high-latitude seas, ocean circulation, and ice-volume fluctuations through time.

The middle to late Miocene is still a poorly constrained interval of the geological timescale, mainly because of incomplete recovery in both marine and land-based sections, which has hampered refinement and verification of astronomical tuning and isotope stratigraphy. Although physical property parameters and bulk isotopes can provide useful high-resolution, local climate records, developing a well-constrained benthic stable isotope chronostratigraphy is essential for the correlation of climatic events on a global scale and anchoring the Neogene geological timescale. The northwest Australian Site U1482 and the Eauripik Rise Sites U1488–U1490 recovered reasonably well preserved, extended upper Miocene sediment successions from multiple holes (Figure **F29**), allowing construction of uninterrupted splices that have high potential for further calibration of the Neogene timescale. Eauripik Rise Site U1490 additionally has a well-defined shipboard magnetostratigraphy over the ~9 to ~19 Ma interval (Figure **F32**), offering an outstanding opportunity to directly correlate magnetostratigraphy, biostratigraphy, and benthic isotope cyclostratigraphy over this entire interval.

Figure F30. Summary age-depth relationships for Expedition 363 sites color-coded according to geographic area and summary climate history of the Neogene, including global benthic foraminifer oxygen isotope stack (Zachos et al. 2001). More negative isotope ratios represent warmer deep-water temperatures and/or lower global ice volume. The Middle Miocene Climate Optimum and the early Pliocene Warm Period are highlighted, together with an indication of Antarctic and Northern Hemisphere ice sheet extent.

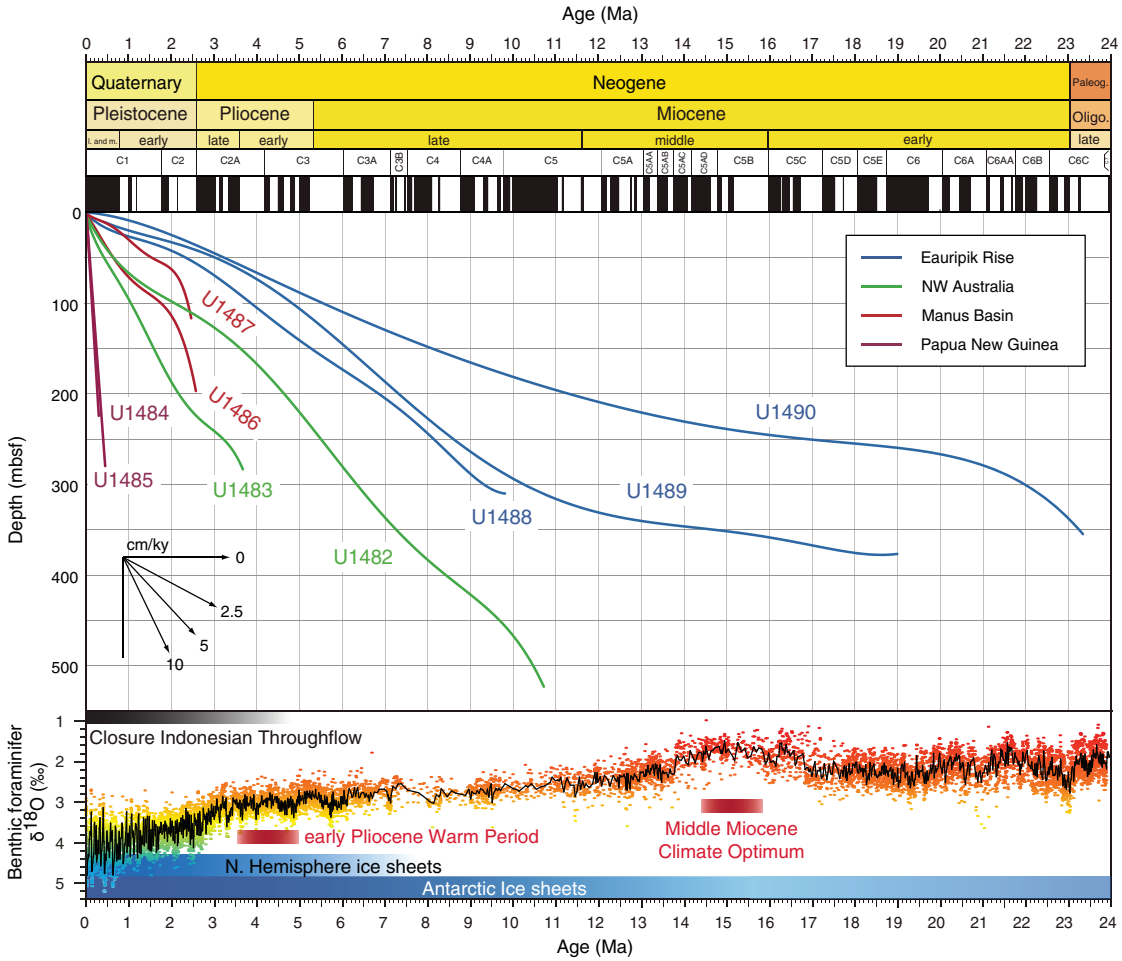

3. Reconstruct the Miocene to late Pleistocene evolution of the Australian monsoon.

The forcing and feedback processes that drive and respond to short- and long-term variability of the Asian-Australian monsoon system remain controversial. This controversy is largely due to the fact that this large-scale, low-latitude climate feature consists of several regional subsystems that are intricately linked through the seasonal migration of the ITCZ but exhibit distinct seasonality of rainfall and wind patterns in response to different forcings (Figure **F36**). Sites U1482 and U1483, located off northwest Australia (Figure **F7**), are suitable to trace the long-term history of the Australian monsoon subsystem from the late Miocene to late Pleistocene. The influence of the warm Leeuwin Current at these sites (Figure **F6**) and their proximity to land will allow assessment of the Australian monsoon's sensitivity to changes in climate boundary conditions such as global ice volume and greenhouse gas concentrations, as well as regional SST changes. These new climate records will also be used to investigate the temporal and regional coupling between different monsoonal subsystems and, in particular, the timing of major reorganizations in wind (driving upwelling and productivity) and precipitation (altering salinity and terrigenous runoff) patterns. The combined records from Sites U1482 and U1488–U1490 will also shed light on the synchroneity and repercussions of the late Miocene biogenic blooms through the Pacific and Indian Oceans and linkages with low- and high-latitude climate change. Furthermore, Expedition 363 will provide a Southern Hemisphere perspective, complementing the overarching goal of several Integrated Ocean Drilling Program and recent IODP expeditions (Expedition 346: Asian Monsoon, Expedition 353: Indian Monsoon Rainfall, Expedition 355: Arabian Sea Monsoon, Expedition 359: Maldives Monsoon and Sea Level, and Expedition 356: Indonesian Throughflow) to unravel the evolution and variability of Indo-Asian-Australian monsoon subsystems over multiple timescales.

4. Reconstruct changes in the ITF through the Neogene.

At present, ITF variability is strongly related to tropical dynamics and in particular to the seasonal reversal of monsoonal winds driven by the latitudinal displacement of the ITCZ. However, on millennial and orbital scales, high-latitude processes and sea level changes might have exerted a major influence on ITF variability. On longer timescales, tectonically driven constrictions in the Indonesian seaways might have altered the balance between Northern and Southern Hemisphere–sourced water contributing to the ITF (Figure **F6**), which in turn could have impacted global climate. In the

Figure F31. Calcareous nannofossils from selected Expedition 363 sites. A. *Emiliania huxleyi*; U1485A-1H-CC. B. *Gephyrocapsa oceanica*; U1485A-1H-CC. C. *Gephyrocapsa* >5.5 µm; U1486B-8H-CC. D, E. *Pseudoemiliania lacunosa*; (D) U1489C-2H-6, 60 cm, (E) U1489B-2H-6, 75 cm. F. *Reticulofenestra asanoi*; U1483A-9H-6, 50 cm. G. *Helicosphaera sellii*; U1486B-10H-CC. H, I. *Calcidiscus macintyrei*; (H) U1486B-12H-CC, (I) U1486B-19H-CC. J. *Coccolithus pelagicus*; U1486B-15H-CC. K. *Discoaster triradiatus*; U1482A-18H-CC. L. *Discoaster pentaradiatus*; U1489C-8H-4, 60 cm. M. *Discoaster brouweri*; U1482A-12H-2, 75 cm. N. *Discoaster variabilis*; U1489B-12H-CC. O. *Discoaster surculus*; U1482B-38H-CC. P. *Sphenolithus abies*; U1483A 31H-CC. Q, R. *Reticulofenestra pseudoumbilicus*; (Q) U1483A-31H-CC, (R) U1489B-10H-CC. S. *Scyphosphaera globulata*; U1488A-14H-2, 60 cm. T, U. *Ceratolithus cristatus*; (T) U1489B-3H-CC, (U) U1482B-18H-CC. V, W. *Ceratolithus armatus*; (V) U1482B-27H-4, 50 cm, (W) U1482B-27H-CC. X. *Amaurolithus tricorniculatus*; U1482A-22H-6, 75 cm. Y. *Amaurolithus delicatus*; U1482B-27H-CC. Z. *Amaurolithus primus*; U1489C-22H-CC. AA. *Triquetrorhabdulus carinatus*; U1489C-31F-CC. AB. *Discoaster* sp.; U1486B-22H-6, 81 cm. AC. *Discoaster tamalis*; U1489B-6H-CC. AD. *Discoaster asymmetricus*; U1483A-31H-CC. AE. *Cyclicargolithus floridanus*; U1489C-38X-6, 40 cm. AF. *Coronocyclus nitescens*; U1489C-42X-4, 30 cm. AG. *Triquetrorhabdulus carinatus*; U1489C-41X-CC. AH. *Sphenolithus heteromorphus*; U1489C-41X-CC. AI. *Sphenolithus belemnos*; U1489C-41X-CC. AJ. *Nicklithus amplificus*; U1482B-33H-CC. AK. *Discoaster quinqueramus*; U1489C-24H-CC. AL. *Discoaster berggrenii*; U1482C-41X-CC. AM. *Catinaster calyculus*; U1489C-31F-CC. AN. *Catinaster coalitus*; U1489C-30F-CC.

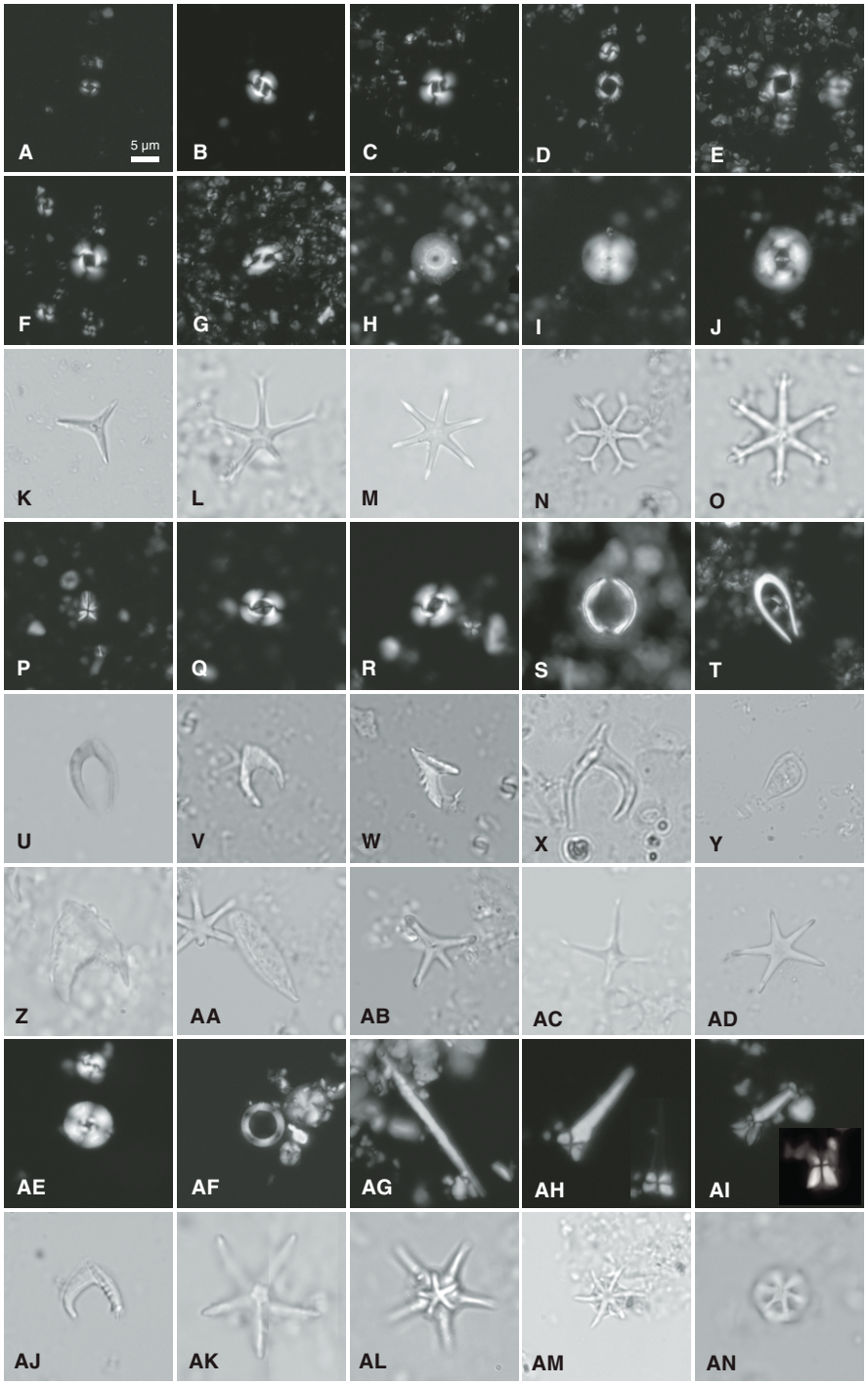

Figure F32. NRM intensity (Int.; blue) and azimuthally corrected declination (Dec.; red) after peak AF demagnetization for Expedition 363 sites. Higher intensity values at Sites U1484–U1487 are influenced by greater terrigenous flux (Sites U1484 and U1485) and volcanogenic inputs (Sites U1486 and U1487). Downhole reductions in intensity, most evident at Sites U1488 and U1489 but also occurring at Sites U1482 and U1483, reflect the influence of sediment diagenesis and the dissolution of magnetite at depth. Where NRM intensity values are low and approach the sensitivity of the magnetometer (10^{-5} A/m), declination becomes increasingly scattered and uninterpretable. In the higher NRM intensity intervals, magnetostratigraphic interpretations are made and age is assigned through correlation of declination to the geomagnetic polarity timescale (Cande and Kent, 1995) of the geologic timescale (Hilgen et al., 2012). This figure is available in an **oversized format**.

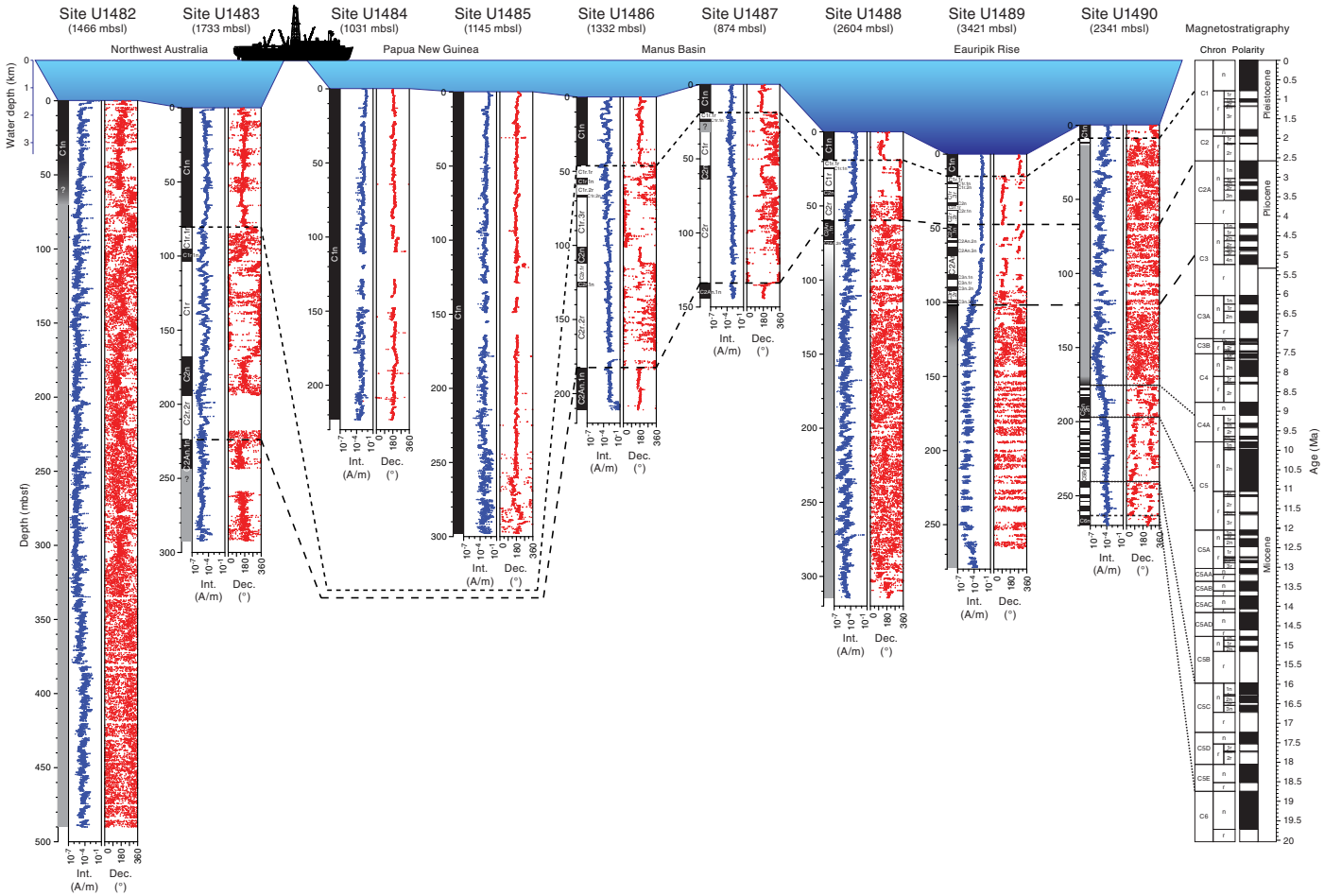

modern ocean, the main ITF transport occurs within the thermocline. Therefore, we expect that comparing changes in the thermocline structure of sites located in the heart of the WPWP, the source region for the ITF, and off northwest Australia/Timor Sea, where the ITF exits into the Indian Ocean, will allow reconstruction of changes in the ITF transport on different timescales. Specifically, records of surface and thermocline temperatures from Sites U1482 (northwest Australia) and U1488 (Eauripik Rise) should allow for distinguishing between broad equatorial responses to global climate change and ITF-related response to the tectonic evolution of the Indonesian seaways from the late Miocene to present. Higher sedimentation rates at Sites U1483 (off northwest Australia) and U1486/U1487 (Manus Basin) will allow for a more detailed reconstruction of ITF variability at orbital and millennial timescales through the entire Pleistocene (Figure **F30**).

5. *Assess the density structure of the western equatorial Pacific during the LGM.*

Because our sites span a large water depth range (Figure **F5**), we conducted high-resolution interstitial water sampling (one sample per section) from the seafloor to as deep as 150 mbsf at four Pacific sites. The interstitial water samples will be used to assess the density structure of the western equatorial Pacific during the LGM. High-resolution interstitial water sampling at Sites U1485, U1486, U1488, and U1489 (western equatorial Pacific Ocean) and moderate-resolution sampling at Site U1482 (eastern Indian Ocean) will generate density profiles of intermediate and deep waters during the LGM based on precise $\delta^{18}O$ and chlorinity measurements. Shipboard analyses indicate that Sites U1488 and U1489 are the least affected by exchange reactions with basement rocks and clay minerals and show the expected diffusion profile, making them suitable for this purpose. At the other two sites where high-resolution sampling took place (Sites U1485 and U1486), the upper sections seem to recover the LGM profile, although shipboard measurements suggest that interactions with basement rock and/or clay mineral diagenesis have a strong influence on the lower part of the profiles. Measurements of oxygen and strontium isotopes will help us to understand the basement–sediment interactions and diagenetic processes at these sites.

Figure F33. NGR data (orange) plotted on core photos (generated using CODD; Wilkens et al., 2017; **https://www.codd-home.net**) for all Expedition 363 sites. Dashed black bars indicate close-ups only available in the site reports. Solid black bars indicate close-ups (see Figure F34) selected as representative of the different site characteristics. Boundaries between background-colored fields represent isochrons for late Oligocene to recent subepochs based on shipboard bio- and magnetostratigraphic age models. This figure is available in an **oversized format**.

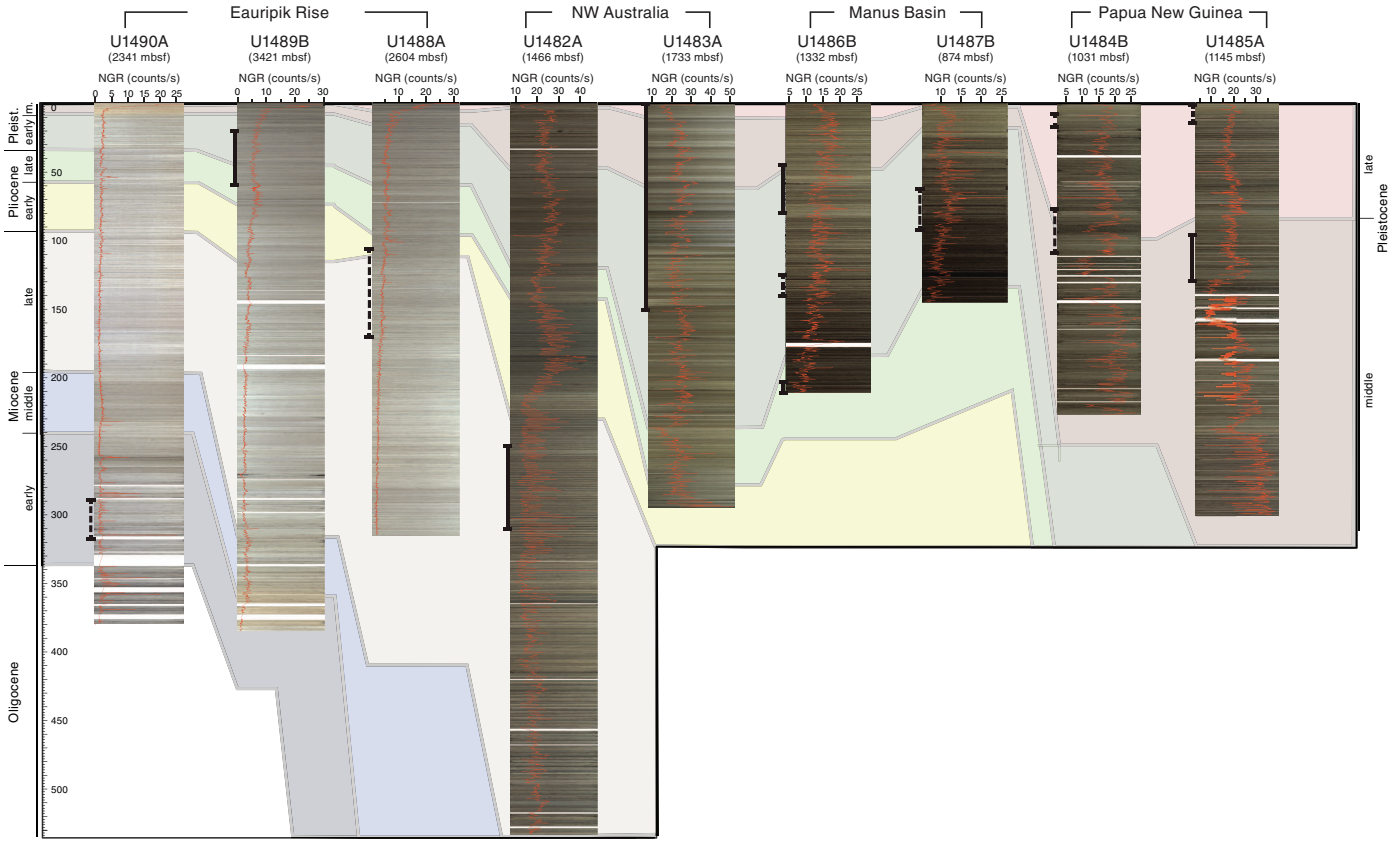

Figure F34. Close-ups of intervals of holes chosen as representative for different sites (see Figure F33) with major physical property measurements overlaid on the composite core photos (generated using CODD; Wilkens et al., 2017; **https://www.codd-home.net**). V_P = *P*-wave velocity.

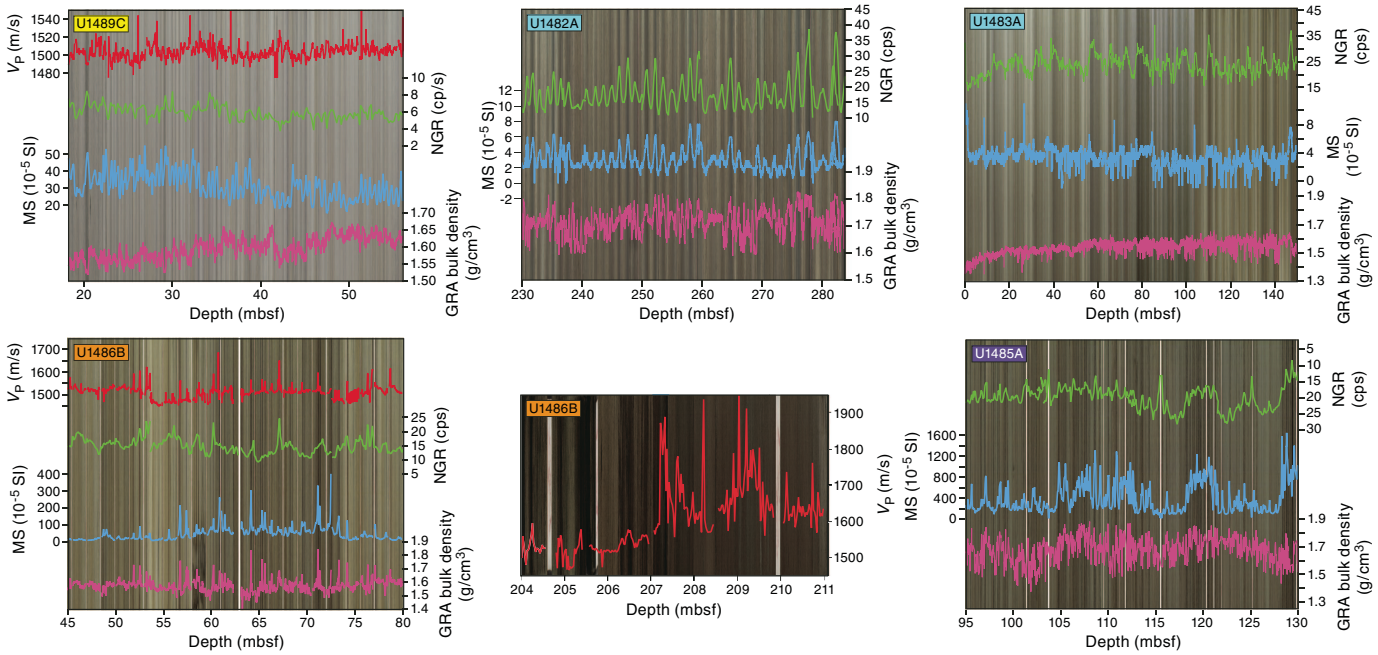

Figure F35. Foraminifer (F) and calcareous nannofossil (N) preservation at Expedition 363 sites. Clay-rich sediment from northwest Australia Sites U1482 and U1483, Papua New Guinea Sites U1484 and U1485, and Manus Basin Sites U1486 and U1487 are characterized by excellent to very good preservation. Carbonate-rich sediment at Eauripik Rise Sites U1488, U1489, and U1490 generally exhibit very good preservation becoming moderate to poor at the ooze-to-chalk transition. This figure is available in an **oversized format**.

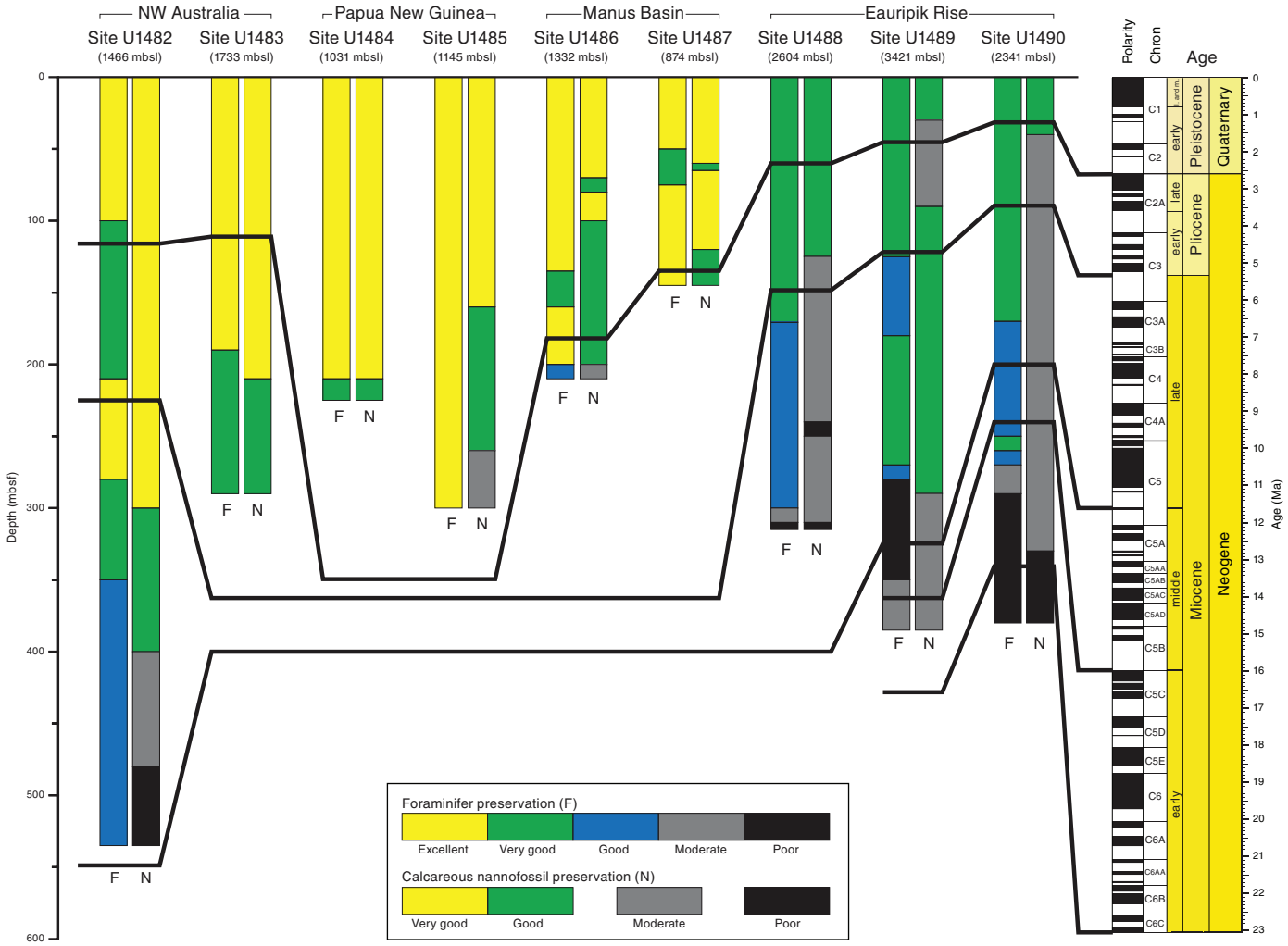

6. Use interstitial water profiles to reconstruct diagenetic processes and their implications for seawater composition.

The large variability in the geologic settings and lithologies of Expedition 363 sites provides the opportunity to study diagenetic processes under various depositional conditions. Interstitial water profiles at marginal Sites U1484 and U1485 (off northern Papua New Guinea) and Sites U1486 and U1487 (Manus Basin), which are rich in volcanogenic sediment (Figure **F29**), are strongly influenced by organic matter remineralization and exchange reactions with basement rocks and clay minerals. The interstitial water samples taken at these sites offer the opportunity for investigating diagenetic processes with emphasis on understanding silicate weathering and dissolution using various isotope systems (e.g., Si, S, Sr, and U isotopes). Splits of interstitial water samples were taken from the pelagic, carbonate-rich sediment at Sites U1488–U1490 for the purpose of reconstructing past seawater chemistry and investigating carbonate diagenesis (e.g., by measuring B, Ca, and Mg isotopes).

Additional highlights

Late Miocene to Holocene depositional history of the northwest Australian margin

The ages assigned to the sedimentary successions recovered at northwest Australian Sites U1482 and U1483 (Figures **F9**, **F11**, **F30**) diverge substantially from previous ages estimated from wireline log data calibrated with stratigraphic and lithologic data from well cuttings (see figures AF5–AF7 and AF9–AF11 in Rosenthal et al., 2016). Following regional seismic projections, we anticipated reaching two prominent reflectors corresponding to (1) a middle Miocene unconformity (~14 Ma) at ~500 mbsf at Site U1482 and (2) a late Miocene unconformity (~6 Ma) at ~250 mbsf at Site U1482 and at ~200 mbsf at Site U1483. However, the ages at the base of Sites U1482 (~535 mbsf) and U1483 (~293 mbsf) are ~10.5 and <3.6 Ma, respectively (Figure **F30**). These ages are considerably younger than was expected at these depths, implying that sedimentation rates in this region differ markedly from previous estimates based on seismic stratigraphy. These new ages will trigger reinterpretation of un-

Figure F36. Strategic locations of Sites U1482 and U1483 designed to monitor the short-and long-term variability of the Australian monsoon. Intensification of the Pilbara Heat Low and its eastward extension to the Kimberleys (indicated by dotted orange lines in large map) during austral summer drive the onset of the wet austral summer monsoon. Wind direction reverses over northwest Australia during the dry austral winter monsoon (small map), when trade winds intensify. Yellow arrows = main eolian dust paths in September (from Hesse and McTainsh, 2003). Figure modified from Kuhnt et al. (2015). Base map was generated with GeoMapApp (**http://www.geomapapp.org**) using the Global Multi-Resolution Topography synthesis database (Ryan et al., 2009). Drainage basins of the Fitzroy and Ord Rivers (**https://data.gov.au/dataset/australias-river-basins-1997**) are marked with a black line. Approximate extensions of the Fitzroy and Ord Rivers on the northwest Australian shelf during the LGM are indicated by blue dashed lines. Generalized wind patterns (white arrows) from Gentilli (1971).

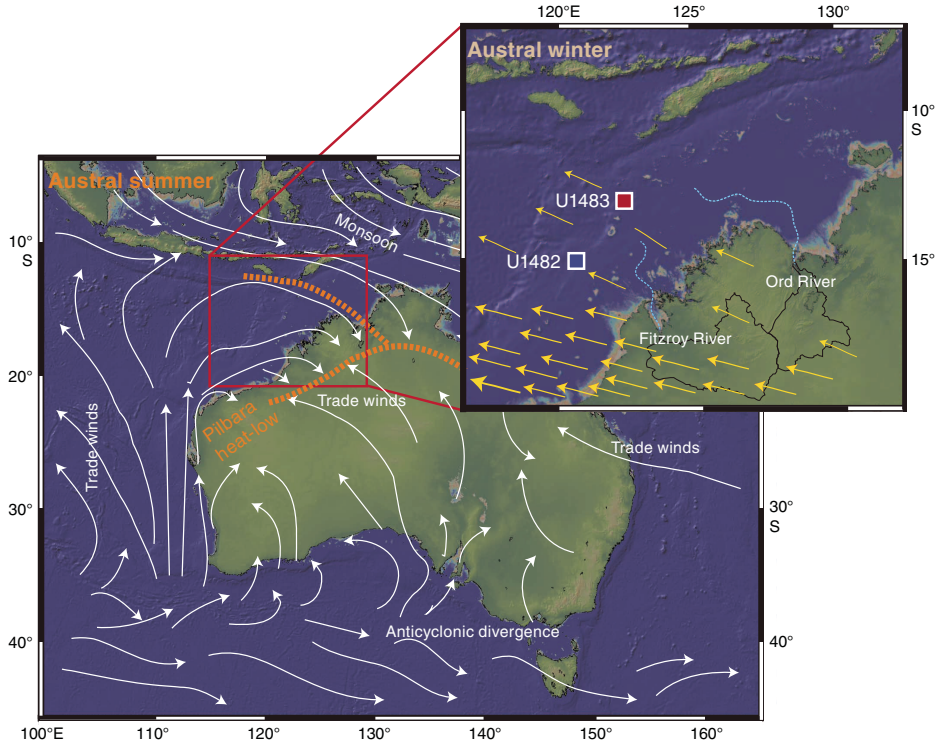

conformities and depositional sequences along the northwest Australian margin. Thus, the records from Sites U1482 and U1483 have high potential to better constrain the Neogene tectonic and paleoceanographic evolution of the northwest Australian margin, including the causes for the widespread demise of the reef system.

Middle Miocene to Holocene carbonate accumulation in the IPWP

Calcium carbonate records from the eastern equatorial Pacific Ocean document substantial changes in the calcite compensation depth (CCD) through the Neogene to the present, suggesting extensive changes in ocean carbonate chemistry (e.g., Pälike et al., 2012). The CCD behaved in a highly dynamic way in the eastern Pacific Ocean during the MMCO and was generally shallower during the late Miocene than at present. In contrast, $CaCO_3$ mass accumulation rates in the eastern Indian, western equatorial Pacific, and southwest Pacific Oceans record higher $CaCO_3$ accumulation rates during the late Miocene (the so called Miocene "biogenic bloom") than at present. We have generated $CaCO_3$ records at a resolution of three per core to document these changes at the northwest Australian Sites U1482 and U1483 (late Miocene to recent) and the Eauripik Rise Sites U1488 and U1489 (early Miocene to recent) to assess the regional extent and magnitude of changes in their carbonate records. These data will provide the framework for more detailed shore-based analyses and regional comparisons. The new records will help to evaluate changes in the oceanic carbonate budget in relation to ocean circulation and global climate trends through the Neogene.

Late Pliocene Admiralty Islands volcanism

The sediment succession at Sites U1486 and U1487 in the Manus Basin consists of clay-rich biogenic ooze overlying a thick succession of volcanogenic-rich sediment with multiple centimeter- to decimeter-thick tephra layers and minor biogenic components (Figures **F17**, **F19**, **F29**). The age at the bottom of the holes, when APC coring reached or came close to refusal, is ~2.7 Ma (Figures **F18**, **F20**, **F30**), and the age of the underlying basement is estimated to be 3.5 Ma (Taylor, 1979). These sites offer the opportunity to examine the repercussions of this prolonged and intense period of volcanism for global climate cooling, both indirectly through the chemical alteration of the fresh basalt and the resulting effect on seawater composition and more directly due to their impact on atmospheric opacity and greenhouse gases.

Intercalibration of biostratigraphy, magnetostratigraphy, and isotope stratigraphy

The calibration of nannofossil and planktonic foraminifer datums, which provide the main biostratigraphic framework over the Neogene geological timescale, is primarily based on previous drilling in the Mediterranean Sea, Atlantic Ocean, and eastern Pacific Ocean. However, these calibrations need to be further expanded to other oceanic regions to test their global applicability. The mostly excellent to good preservation of calcareous microfossils in contin-

uous, extended Miocene to Pleistocene sediment successions from the northwest Australian Sites U1482 and U1483 and the WPWP Sites U1484–U1490 (Figure **F35**) will allow high-resolution taxonomic and biostratigraphic studies, as well as detailed correlation of bioevents with isotope stratigraphy and magnetostratigraphy. These sites offer the opportunity to improve the calibration of speciation/extinction events and to test the synchroneity/diachroneity of bioevents in different ocean basins (Atlantic, Pacific, and Indian Oceans). Furthermore, these sites are suitable for investigating gradual or abrupt morphological changes, including coiling changes in planktonic foraminifers, that have the potential for stratigraphy and to explore relationships between evolutionary events and changing ocean chemistry and circulation through most of the Neogene.

Site survey data

The supporting site survey data for Expedition 363 are archived at the IODP Site Survey Data Bank. Data can be accessed at **http://ssdb.iodp.org/SSDBquery/SSDBquery.php** by selecting the appropriate proposal number.

References

Adkins, J.F., McIntyre, K., and Schrag, D.P., 2002. The salinity, temperature, and $\delta^{18}O$ of the glacial deep ocean. *Science,* 298(5599):1769–1773. **https://doi.org/10.1126/science.1076252**

Amante, C., and Eakins, B.W., 2009. *ETOPO1 1 Arc-Minute Global Relief Model: Procedures, Data Sources and Analysis.* NOAA Technical Memorandum NESDIS NGDC-24. National Geophysical Data Center, NOAA. **https://doi.org/10.7289/V5C8276M**

Anderson, R.F., Ali, S., Bradtmiller, L.I., Nielsen, S.H.H., Fleisher, M.Q., Anderson, B.E., and Burckle, L.H., 2009. Wind-driven upwelling in the Southern Ocean and the deglacial rise in atmospheric CO_2. *Science,* 323(5920):1443–1448. **https://doi.org/10.1126/science.1167441**

Ayliffe, L.K., Gagan, M.K., Zhao, J., Drysdale, R.N., Hellstrom, J.C., Hantoro, W.S., Griffiths, M.L., et al., 2013. Rapid interhemispheric climate links via the Australasian monsoon during the last deglaciation. *Nature Communications,* 4:2908. **https://doi.org/10.1038/ncomms3908**

Baldwin, K.E., Mountain, G.S., and Rosenthal, Y., 2017. Sediment waves in the Caroline Basin suggest evidence for Miocene shifts in bottom water flow in the western equatorial Pacific. *Marine Geology,* 393:194–202. **https://doi.org/10.1016/j.margeo.2017.07.017**

Baldwin, S.L., Fitzgerald, P.G., and Webb, L.E., 2012. Tectonics of the New Guinea region. *Annual Review of Earth and Planetary Sciences,* 40(1):495–520. **https://doi.org/10.1146/annurev-earth-040809-152540**

Bracey, D.R., 1975. Reconnaissance geophysical survey of the Caroline Basin. *Geological Society of America Bulletin,* 86(6):775–784. **https://doi.org/10.1130/0016-7606(1975)86<775:RGSOTC>2.0.CO;2**

Brierley, C.M., Fedorov, A.V., Liu, Z., Herbert, T.D., Lawrence, K.T., and LaRiviere, J.P., 2009. Greatly expanded tropical warm pool and weakened Hadley circulation in the early Pliocene. *Science,* 323(5922):1714–1718. **https://doi.org/10.1126/science.1167625**

Broccoli, A.J., Dahl, K.A., and Stouffer, R.J., 2006. Response of the ITCZ to Northern Hemisphere cooling. *Geophysical Research Letters,* 33(1):L01702. **https://doi.org/10.1029/2005GL024546**

Broecker, W., and Barker, S., 2007. A 190‰ drop in atmosphere's $\Delta^{14}C$ during the "Mystery Interval" (17.5 to 14.5 kyr). *Earth and Planetary Science Letters,* 256(1–2):90–99. **https://doi.org/10.1016/j.epsl.2007.01.015**

Brown, J.N., Langlais, C., and Sen Gupta, A., 2015. Projected sea surface temperature changes in the equatorial Pacific relative to the Warm Pool edge. *Deep Sea Research, Part II: Topical Studies in Oceanography,* 113:47–58. **https://doi.org/10.1016/j.dsr2.2014.10.022**

Bruch, A.A., Uhl, D., and Mosbrugger, V., 2007. Miocene climate in Europe—patterns and evolution: a first synthesis of NECLIME. *Palaeogeography, Palaeoclimatology, Palaeoecology,* 253(1–2):1–7. **https://doi.org/10.1016/j.palaeo.2007.03.030**

Cande, S.C., and Kent, D.V., 1995. Revised calibration of the geomagnetic polarity timescale for the Late Cretaceous and Cenozoic. *Journal of Geophysical Research: Solid Earth,* 100(B4):6093–6095. **https://doi.org/10.1029/94JB03098**

Cane, M., and Clement, A.C., 1999. A role for the tropical Pacific coupled ocean-atmosphere system on Milankovitch and millennial timescales, Part II: global impacts. *In* Clark, P.U., Webb, R.S., and Keigwin, L.D. (Eds.), *Mechanisms of Global Climate Change at Millennial Time Scales.* Geophysical Monograph, 112:373–383. **https://doi.org/10.1029/GM112p0373**

Cane, M.A., and Molnar, P., 2001. Closing of the Indonesian Seaway as a precursor to East African aridification around 3–4 million years ago. *Nature,* 411(6834):157–162. **https://doi.org/10.1038/35075500**

Carolin, S.A., Cobb, K.M., Adkins, J.F., Clark, B., Conroy, J.L., Lejau, S., Malang, J., and Tuen, A.A., 2013. Varied response of Western Pacific hydrology to climate forcings over the last glacial period. *Science,* 340(6140):1564–1566. **https://doi.org/10.1126/science.1233797**

Ceppi, P., Hwang, Y.-T., Liu, X., Frierson, D.M.W., and Hartmann, D.L., 2013. The relationship between the ITCZ and the Southern Hemispheric eddy-driven jet. *Journal of Geophysical Research: Atmospheres,* 118(11):5136–5146. **https://doi.org/10.1002/jgrd.50461**

Chen, T., Robinson, L.F., Beasley, M.P., Claxton, L.M., Andersen, M.B., Gregoire, L.J., Wadham, J., Fornari, D.J., and Harpp, K.S., 2016. Ocean mixing and ice-sheet control of seawater $^{234}U/^{238}U$ during the last deglaciation. *Science,* 354(6312):626–629. **https://doi.org/10.1126/science.aag1015**

Chiang, J.C.H., and Bitz, C.M., 2005. Influence of high latitude ice cover on the marine Intertropical Convergence Zone. *Climate Dynamics,* 25(5):477–496. **https://doi.org/10.1007/s00382-005-0040-5**

Christensen, B.A., Renema, W., Henderiks, J., De Vleeschouwer, D., Groeneveld, J., Castañeda, I.S., Reuning, et al., 2017. Indonesian Throughflow drove Australian climate from humid Pliocene to arid Pleistocene. *Geophysical Research Letters,* 44(13):6914–6925. **https://doi.org/10.1002/2017GL072977**

Clark, P.U., Marshall, S.J., Clarke, G.K.C., Hostetler, S.W., Licciardi, J.M., and Teller, J.T., 2001. Freshwater forcing of abrupt climate change during the last glaciation. *Science,* 293(5528):283–287. **https://doi.org/10.1126/science.1062517**

Clark, P.U., McCabe, A.M., Mix, A.C., and Weaver, A.J., 2004. Rapid rise of sea level 19,000 years ago and its global implications. *Science,* 304(5674):1141–1144. **https://doi.org/10.1126/science.1094449**

Clement, A.C., Cane, M.A., and Seager, R., 2001. An orbitally driven tropical source for abrupt climate change. *Journal of Climate,* 14(11):2369–2375. **https://doi.org/10.1175/1520-0442(2001)014<2369:AODTSF>2.0.CO;2**

Dang, H., Jian, Z., Kissel, C., and Bassinot, F., 2015. Precessional changes in the western equatorial Pacific hydroclimate: a 240 kyr marine record from the Halmahera Sea, East Indonesia. *Geochemistry, Geophysics, Geosystems,* 16(1):148–164. **https://doi.org/10.1002/2014GC005550**

Dannenmann, S., Linsley, B.K., Oppo, D.W., Rosenthal, Y., and Beaufort, L., 2003. East Asian monsoon forcing of suborbital variability in the Sulu Sea during marine isotope Stage 3: link to Northern Hemisphere climate. *Geochemistry, Geophysics, Geosystems,* 4(1):1–13. **https://doi.org/10.1029/2002GC000390**

de Garidel-Thoron, T., Rosenthal, Y., Bassinot, F., and Beaufort, L., 2005. Stable sea surface temperatures in the Western Pacific Warm Pool over the past 1.75 million years. *Nature,* 433(7023):294–298. **https://doi.org/10.1038/nature03189**

Denton, G.H., Anderson, R.F., Toggweiler, J.R., Edwards, R.L., Shaefer, J.M., and Putnam, A.E., 2010. The last glacial termination. *Science,* 328(5986):1652–1656. **https://doi.org/10.1126/science.1184119**

DiNezio, P., Clement, A., and Vecchi, G., 2010. Reconciling differing views of tropical Pacific climate change. *Eos, Transactions of the American Geo-*

physical Union, 91(16):141–142. **https://doi.org/10.1029/2010EO160001**

DiNezio, P.N., Clement, A.C., Vecchi, G.A., Soden, B.J., Kirtman, B.P., and Lee, S.-K., 2009. Climate response of the equatorial Pacific to global warming. *Journal of Climate,* 22(18):4873–4892. **https://doi.org/10.1175/2009JCLI2982.1**

Dowsett, H.J., Robinson, M.M., and Foley, K.M., 2009. Pliocene three-dimensional global ocean temperature reconstruction. *Climate of the Past,* 5(4):769–783. **https://doi.org/10.5194/cp-5-769-2009**

England, M.H., McGregor, S., Spence, P., Meehl, G.A., Timmermann, A., Cai, W., Sen Gupta, A., McPhaden, M.J., Purich, A., and Santoso, A., 2014. Recent intensification of wind-driven circulation in the Pacific and the ongoing warming hiatus. *Nature Climate Change,* 4(3):222–227. **https://doi.org/10.1038/nclimate2106**

Farrell, J.W., Raffi, I., Janecek, T.R., Murray, D.W., Levitan, M., Dadey, K.A., Emeis, K.-C., Lyle, M., Flores, J.-A., and Hovan, S., 1995. Late Neogene sedimentation patterns in the eastern equatorial Pacific Ocean. *In* Pisias, N.G., Mayer, L.A., Janecek, T.R., Palmer-Julson, A., and van Andel, T.H. (Eds.), *Proceedings of the Ocean Drilling Program, Scientific Results,* 138: College Station, TX (Ocean Drilling Program), 717–756. **https://doi.org/10.2973/odp.proc.sr.138.143.1995**

Fedorov, A.V., Brierley, C.M., and Emanuel, K., 2010. Tropical cyclones and permanent El Niño in the early Pliocene epoch. *Nature,* 463(7284):1066–1070. **https://doi.org/10.1038/nature08831**

Fedorov, A.V., Brierley, C.M., Lawrence, K.T., Liu, Z., Dekens, P.S., and Ravelo, A.C., 2013. Patterns and mechanisms of early Pliocene warmth. *Nature,* 496(7443):43–49. **https://doi.org/10.1038/nature12003**

Ffield, A., Vranes, K., Gordon, A.L., Susanto, R.D., and Garzoli, S.L., 2000. Temperature variability within Makassar Strait. *Geophysical Research Letters,* 27(2):237–240. **https://doi.org/10.1029/1999GL002377**

Fieux, M., Andrié, C., Delecluse, P., Ilahude, A.G., Kartavtseff, A., Mantisi, F., Molcard, R., and Swallow, J.C., 1994. Measurements within the Pacific–Indian Oceans throughflow region. *Deep Sea Research, Part I: Oceanographic Research Papers,* 41(7):1091–1130. **https://doi.org/10.1016/0967-0637(94)90020-5**

Fine, R.A., Lukas, R., Bingham, F.M., Warner, M.J., and Gammon, R.H., 1994. The western equatorial Pacific: a water mass crossroads. *Journal of Geophysical Research: Oceans,* 99(C12):25063–25080. **https://doi.org/10.1029/94JC02277**

Flower, B.P., and Kennett, J.P., 1994. The middle Miocene climatic transition: East Antarctic ice sheet development, deep ocean circulation and global carbon cycling. *Palaeogeography, Palaeoclimatology, Palaeoecology,* 108(3–4):537–555. **https://doi.org/10.1016/0031-0182(94)90251-8**

Ford, H.L., Ravelo, A.C., and Polissar, P.J., 2015. Reduced El Niño–Southern Oscillation during the Last Glacial Maximum. *Science,* 347(6219):255–258. **https://doi.org/10.1126/science.1258437**

Forster, P., Ramaswamy, V., Artaxo, P., Berntsen, T., Betts, R., Fahey, D.W., Haywood, et al., 2007. Changes in atmospheric constituents and in radiative forcing. *In* Solomon, S., Qin, D., Manning, M., Chen, Z., Marquis, M., Averyt, K.B., Tignor, M., and Miller, H.L. (Eds.), *Climate Change 2007: The Physical Science Basis: Contribution of Working Group I to the Fourth Assessment Report of the Intergovernmental Panel on Climate Change:* Cambridge, United Kingdom (Cambridge University Press), 129–234. **https://www.ipcc.ch/pdf/assessment-report/ar4/wg1/ar4-wg1-chapter2.pdf**

Gentilli, J. (Ed.), 1971. *World Survey of Climatology* (Volume 13): *Climates of Australia and New Zealand:* Amsterdam (Elsevier).

Gibbons, F.T., Oppo, D.W., Mohtadi, M., Rosenthal Y., Cheng, J., Liu, Z., and Linsley, B.K., 2014. Deglacial $\delta^{18}O$ and hydrologic variability in the tropical Pacific and Indian Oceans. *Earth and Planetary Science Letters,* 387:240–251. **https://doi.org/10.1016/j.epsl.2013.11.032**

Gordon, A.L., 2005. Oceanography of the Indonesian seas and their throughflow. *Oceanography,* 18(4):14–27. **https://doi.org/10.5670/oceanog.2005.01**

Gordon, A.L., and Fine, R.A., 1996. Pathways of water between the Pacific and Indian Oceans in the Indonesian seas. *Nature,* 379(6561):146–149. **https://doi.org/10.1038/379146a0**

Gordon, A.L., and Susanto, R.D., 1999. Makassar Strait transport: initial estimate based on Arlindo results. *Marine Technology Society Journal,* 32(4):34–45.

Gordon, A.L., Susanto, R.D., and Vranes, K., 2003. Cool Indonesian throughflow as a consequence of restricted surface layer flow. *Nature,* 425(6960):824–828. **https://doi.org/10.1038/nature02038**

Gradstein, F.M., 1992. Legs 122 and 123, northwestern Australian margin—a stratigraphic and paleogeographic summary. *In* Gradstein, F.M., Ludden, J.N., et al., *Proceedings of the Ocean Drilling Program, Scientific Results,* 123: College Station, TX (Ocean Drilling Program), 801–816. **https://doi.org/10.2973/odp.proc.sr.123.110.1992**

Greenop, R., Foster, G.L., Wilson, P.A., and Lear, C.H., 2014. Middle Miocene climate instability associated with high-amplitude CO_2 variability. *Paleoceanography,* 29(9):845–853. **https://doi.org/10.1002/2014PA002653**

Gupta, A.K., and Thomas, E., 1999. Latest Miocene–Pleistocene productivity and deep-sea ventilation in the northwestern Indian Ocean (Deep Sea Drilling Project Site 219). *Paleoceanography,* 14(1): 62–73. **https://doi.org/10.1029/1998PA900006**

Hall, R., 2012. Late Jurassic–Cenozoic reconstructions of the Indonesian region and the Indian Ocean. *Tectonophysics,* 570–571:1–41. **https://doi.org/10.1016/j.tecto.2012.04.021**

Halpert, M.S., and Ropelewski, C.F., 1992. Surface temperature patterns associated with the Southern Oscillation. *Journal of Climate,* 5(6):577–593. **https://doi.org/10.1175/1520-0442(1992)005<0577:STPAWT>2.0.CO;2**

Hansen, J., Sato, M., Kharecha, P., Beerling, D., Berner, R., Masson-Delmotte, V., Pagani, M., Raymo, M., Royer, D.L., and Zachos, J.C., 2008. Target atmospheric CO_2: where should humanity aim? *The Open Atmospheric Science Journal,* 2(1):217–231. **https://doi.org/10.2174/1874282300802010217**

Hautala, S.L., Reid, J.L., and Bray, N., 1996. The distribution and mixing of Pacific water masses in the Indonesian Seas. *Journal of Geophysical Research: Oceans,* 101(C5):12375–12389. **https://doi.org/10.1029/96JC00037**

Hegarty, K.A., and Weissel, J.K., 1988. Complexities in the developments of the Caroline plate region, western equatorial Pacific. *In* Nairn, A.E.M., Stehli, F.G., and Uyeda, S. (Eds.), *The Ocean Basins and Margins:* Boston (Springer), 277–301. **https://doi.org/10.1007/978-1-4615-8041-6_6**

Hesse, P.P., and McTainsh, G.H., 2003. Australian dust deposits: modern processes and the Quaternary record. *Quaternary Science Reviews,* 22(18–19):2007–2035. **https://doi.org/10.1016/S0277-3791(03)00164-1**

Hilgen, F.J., Lourens, L.J., and Van Dam, J.A., 2012. The Neogene period. With contributions by A.G. Beu, A.F. Boyes, R.A. Cooper, W. Krijgsman, J.G. Ogg, W.E. Piller, and D.S. Wilson. *In* Gradstein, F.M., Ogg, J.G., Schmitz, M.D., and Ogg, G.M. (Eds.), *The Geologic Time Scale:* Oxford, United Kingdom (Elsevier), 923–978. **https://doi.org/10.1016/B978-0-444-59425-9.00029-9**

Hines, S.K.V., Southon, J.R., and Adkins, J.F., 2015. A high-resolution record of Southern Ocean intermediate water radiocarbon over the past 30,000 years. *Earth and Planetary Science Letters,* 432:46–58. **https://doi.org/10.1016/j.epsl.2015.09.038**

Holbourn, A., Kuhnt, W., Kawamura, H., Jian, Z., Grootes, P., Erlenkeuser, H., and Xu, J., 2005. Orbitally paced paleoproductivity variations in the Timor Sea and Indonesian Throughflow variability during the last 460 kyr. *Paleoceanography,* 20(3):PA3002. **https://doi.org/10.1029/2004PA001094**

Holbourn, A., Kuhnt, W., Regenberg, M., Schulz, M., Mix, A., and Andersen, N., 2010. Does Antarctic glaciation force migration of the tropical rain belt? *Geology,* 38(9):783–786. **https://doi.org/10.1130/G31043.1**

Holbourn, A., Kuhnt, W., Simo, J.A., and Li, Q., 2004. Middle Miocene isotope stratigraphy and paleoceanographic evolution of the northwest and southwest Australian margins (Wombat Plateau and Great Australian Bight). *Palaeogeography, Palaeoclimatology, Palaeoecology,* 208(1–2):1–22. **https://doi.org/10.1016/j.palaeo.2004.02.003**

Johnson, G.C., and McPhaden, M.J., 1999. Interior pycnocline flow from the subtropical to the equatorial Pacific Ocean. *Journal of Physical Oceanog-*

raphy, 29(12):3073–3098. **https://doi.org/10.1175/1520-0485(1999)029<3073:IPFFTS>2.0.CO;2**

Jørgensen, B.B., 1977. The sulfur cycle of a coastal marine sediment (Limfjorden, Denmark). *Limnology and Oceanography,* 22(5):814–832. **https://doi.org/10.4319/lo.1977.22.5.0814**

Karas, C., Nürnberg, D., Gupta, A.K., Tiedemann, R., Mohan, K., and Bickert, T., 2009. Mid-Pliocene climate change amplified by a switch in Indonesian subsurface throughflow. *Nature Geoscience,* 2(6):434–438. **https://doi.org/10.1038/ngeo520**

Karas, C., Nürnberg, D., Tiedemann, R., and Garbe-Schönberg, D., 2011. Pliocene Indonesian Throughflow and Leeuwin Current dynamics: implications for Indian Ocean polar heat flux. Paleoceanography, 26(2):PA2217. **https://doi.org/10.1029/2010PA001949**

Karlin, R., and Levi, S., 1983. Diagenesis of magnetic minerals in recent hemipelagic sediments. *Nature,* 303(5915):327–330. **https://doi.org/10.1038/303327a0**

Keep, M., Harrowfield, M., and Crowe, W., 2007. The Neogene tectonic history of the North West Shelf, Australia. *Exploration Geophysics,* 38(3):151–174. **https://doi.org/10.1071/EG07022**

Kim, J.-H., Torres, M.E., Haley, B.A., Ryu, J.-S., Park, M.-H., Hong, W.-L., and Choi, J., 2016. Marine silicate weathering in the anoxic sediment of the Ulleung Basin: evidence and consequences. *Geochemistry, Geophysics, Geosystems,* 17(8):3437–3453. **https://doi.org/10.1002/2016GC006356**

Kissel, C., Laj, C., Kienast, M., Bolliet, T., Holbourn, A., Hill, P., Kuhnt, W., and Braconnot, P., 2010. Monsoon variability and deep oceanic circulation in the western equatorial Pacific over the last climatic cycle: insights from sedimentary magnetic properties and sortable silt. *Paleoceanography,* 25(3):PA3215. **http://dx.doi.org/10.1029/2010PA001980**

Koutavas, A., deMendocal, P.B., Olive, G.C., and Lynch-Stieglitz, J., 2006. Mid-Holocene El Niño–Southern Oscillation (ENSO) attenuation revealed by individual foraminifera in eastern tropical Pacific sediments. *Geology,* 34(12):993–996. **https://doi.org/10.1130/G22810A.1**

Koutavas, A., Lynch-Steiglitz, J., Marchitto, T.M., Jr., and Sachs, J.P., 2002. El Niño-like pattern in Ice Age tropical Pacific sea surface temperature. *Science,* 297(5579):226–230. **https://doi.org/10.1126/science.1072376**

Kroenke, L.W., Berger, W.H., Janecek, T.R., et al., 1991. *Proceedings of the Ocean Drilling Program, Initial Reports,* 130: College Station, TX (Ocean Drilling Program). **https://doi.org/10.2973/odp.proc.ir.130.1991**

Kuhnt, W., Holbourn, A., Hall, R., Zuvela, M., and Käse, R., 2004. Neogene history of the Indonesian Throughflow. *In* Clift, P., Wang, P., Kuhnt, W., and Hayes, D. (Eds.), *Continent-Ocean Interactions within East Asian Marginal Seas.* Geophysical Monograph, 149:299–320. **https://doi.org/10.1029/149GM16**

Kuhnt, W., Holbourn, A., Xu, J., Opdyke, B., De Deckker, P., Röhl, U., and Mudelsee, M., 2015. Southern Hemisphere control on Australian monsoon variability during the late deglaciation and Holocene. *Nature Communications,* 6:5916. **https://doi.org/10.1038/ncomms6916**

Kuroda, Y., 2000. Variability of currents off the northern coast of New Guinea. *Journal of Oceanography,* 56(1):103–116. **https://doi.org/10.1023/A:1011122810354**

Kürschner, W.M., Kvacek, Z., and Dilcher, D.L., 2008. The impact of Miocene atmospheric carbon dioxide fluctuations on climate and the evolution of terrestrial ecosystems. *Proceedings of the National Academy of Sciences of the United States of America,* 105(2):449–453. **https://doi.org/10.1073/pnas.0708588105**

Kürschner, W.M., van der Burgh, J., Visscher, H., and Dilcher, D.L., 1996. Oak leaves as biosensors of late Neogene and early Pleistocene paleoatmospheric CO_2 concentrations. *Marine Micropaleontology,* 27(1–4):299–312. **https://doi.org/10.1016/0377-8398(95)00067-4**

LaRiviere, J.P., Ravelo, A.C., Crimmins, A., Dekens, P.S., Ford, H.L., Lyle, M., and Wara, M.W., 2012. Late Miocene decoupling of oceanic warmth and atmospheric carbon dioxide forcing. *Nature,* 486(7401):97–100. **https://doi.org/10.1038/nature11200**

Lea, D.W., 2004. The 100,000-yr cycle in tropical SST, greenhouse forcing, and climate sensitivity. *Journal of Climatology,* 17(11):2170–2179. **https://doi.org/10.1175/1520-0442(2004)017<2170:TYCITS>2.0.CO;2**

Lee, S.-Y., Chiang, J.C.H., Matsumoto, K., and Tokos, K.S., 2011. Southern Ocean wind response to North Atlantic cooling and the rise in atmospheric CO_2: modeling perspective and paleoceanographic implications. *Paleoceanography,* 26(1):PA1214. **https://doi.org/10.1029/2010PA002004**

Linsley, B.K., Rosenthal, Y., and Oppo, D.W., 2010. Holocene evolution of the Indonesian Throughflow and Western Pacific Warm Pool. *Nature Geoscience,* 3(8):578–583. **https://doi.org/10.1038/ngeo920**

Lyons, T.W., Walter, L.M., Gellatly, A.M., Martini, A.M., and Blake, R.E., 2004. Sites of anomalous organic remineralization in the carbonate sediments of South Florida, USA: the sulfur cycle and carbonate-associated sulfate. *In* Amend, J.P., Edwards, K.J., and Lyons, T.W. (Eds.), *Sulfur Biogeochemistry: Past and Present.* Special Paper - Geological Society of America, 379:161–176. **https://doi.org/10.1130/0-8137-2379-5.161**

MacAyeal, D., 1993. Binge/purge oscillations of the Laurentide ice sheet as a cause of the North Atlantic's Heinrich events. *Paleoceanography,* 8(6):775–784. **https://doi.org/10.1029/93PA02200**

Maher, K., DePaolo, D.J., and Lin, J.C.-F., 2004. Rates of silicate dissolution in deep-sea sediment: in situ measurement using $^{234}U/^{238}U$ of pore fluids. *Geochimica et Cosmochimica Acta,* 68(22):4629–4648. **https://doi.org/10.1016/j.gca.2004.04.024**

McManus, J.F., Oppo, D.W., and Cullen, J.L., 1999. A 0.5-million-year record of millennial-scale climate variability in the North Atlantic. *Science,* 283(5404):971–975. **https://doi.org/10.1126/science.283.5404.971**

Medina-Elizalde, M., and Lea, D.W., 2005. The mid-Pleistocene transition in the tropical Pacific. *Science,* 310(5750):1009–1012. **https://doi.org/10.1126/science.1115933**

Medina-Elizalde, M., and Lea, D.W., 2010. Late Pliocene equatorial Pacific. *Paleoceanography,* 25(2):PA2208. **https://doi.org/10.1029/2009PA001780**

Michalopoulos, P., and Aller, R.C., 1995. Rapid clay mineral formation in Amazon delta sediments: reverse weathering and oceanic elemental cycles. *Science,* 270(5236):614–617. **https://doi.org/10.1126/science.270.5236.614**

Milliman, J.D., Farnsworth, K.L., and Albertin, C.S., 1999. Flux and fate of fluvial sediments leaving large islands in the East Indies. *Journal of Sea Research,* 41(1–2):97–107. **https://doi.org/10.1016/S1385-1101(98)00040-9**

Mosbrugger, V., Utescher, T., and Dilcher, D.L., 2005. Cenozoic continental climatic evolution of central Europe. *Proceedings of the National Academy of Sciences of the United States of America,* 102(42):14964–14969. **https://doi.org/10.1073/pnas.0505267102**

Nathan, S.A., and Leckie, R.M., 2009. Early history of the Western Pacific Warm Pool during the middle to late Miocene (~13.2–5.8 Ma): role of sea-level change and implications for equatorial circulation. *Palaeogeography, Palaeoclimatology, Palaeoecology,* 274(3–4):140–159. **http://dx.doi.org/10.1016/j.palaeo.2009.01.007**

Neale, R., and Slingo, J., 2003. The maritime continent and its role in the global climate: a GCM study. *Journal of Climate,* 16(5):834–848. **https://doi.org/10.1175/1520-0442(2003)016<0834:TMCAIR>2.0.CO;2**

Oppo, D.W., Linsley, B.K., Rosenthal, Y., Dannenmann, S., and Beaufort, L., 2003. Orbital and suborbital climate variability in the Sulu Sea, western tropical Pacific. *Geochemistry, Geophysics, Geosystems,* 4(1):1–20. **https://doi.org/10.1029/2001GC000260**

Oppo, D.W., and Rosenthal, Y., 2010. The great Indo-Pacific communicator. *Science,* 328(5985):1492–1494. **https://doi.org/10.1126/science.1187273**

Pagani, M., Liu, Z., LaRiviere, J., and Ravelo, A.C., 2010. High Earth-system climate sensitivity determined from Pliocene carbon dioxide concentrations. *Nature Geoscience,* 3:27–30. **https://doi.org/10.1038/ngeo724**

Pälike, H., Lyle, M.W., Nishi, H., Raffi, I., Ridgwell, A., Gamage, K., Klaus, A., et al., 2012. A Cenozoic record of the equatorial Pacific carbonate compensation depth. *Nature,* 488(7413):609–614. **https://doi.org/10.1038/nature11360**

Rahmstorf, S., 2002. Ocean circulation and climate during the past 120,000 years. *Nature,* 419(6903):207–214. **https://doi.org/10.1038/nature01090**

Rasmusson, E.M., and Arkin, P.A., 1993. A global view of large-scale precipitation variability. *Journal of Climate,* 6(8):1495–1522. **https://doi.org/10.1175/1520-0442(1993)006<1495:AGVOLS>2.0.CO;2**

Ravelo, A.C., Lawrence, K.T., Fedorov, A., and Ford, H.L., 2014. Comment on "A 12-million-year temperature history of the tropical Pacific Ocean." *Science,* 346(6216):1467. **https://doi.org/10.1126/science.1257618**

Retallack, G.J., 2009. Refining a pedogenic-carbonate CO_2 paleobarometer to quantify a middle Miocene greenhouse spike. *Palaeogeography, Palaeoclimatology, Palaeoecology,* 281(1–2):57–65. **https://doi.org/10.1016/j.palaeo.2009.07.011**

Ropelewski, C.F., and Halpert, M.S., 1987. Global and regional scale precipitation patterns associated with the El Niño/Southern Oscillation. *Monthly Weather Review,* 115(8):1606–1626. **https://doi.org/10.1175/1520-0493(1987)115<1606:GARSPP>2.0.CO;2**

Rosenthal, Y., Holbourn, A., and Kulhanek, D.K., 2016. *Expedition 363 Scientific Prospectus: Western Pacific Warm Pool.* International Ocean Discovery Program. **https://doi.org/10.14379/iodp.sp.363.2016**

Rowan, C.J., Roberts, A.P., and Broadbent, T., 2009. Reductive diagenesis, magnetite dissolution, greigite growth and paleomagnetic smoothing in marine sediments: a new view. *Earth and Planetary Science Letters,* 277(1–2):223–235. **https://doi.org/10.1016/j.epsl.2008.10.016**

Ryan, W.B.F., Carbotte, S.M., Coplan, J.O., O'Hara, S., Melkonian, A., Arko, R., Weissel, R.A., Ferrini, V., Goodwillie, A., Nitsche, F., Bonczkowski, J., and Zemsky, R., 2009. Global multi-resolution topography synthesis. *Geochemistry, Geophysics, Geosystems,* 10(3):Q03014. **https://doi.org/10.1029/2008GC002332**

Schmittner, A., Saenko, O.A., and Weaver, A.J., 2003. Coupling of the hemispheres in observations and simulations of glacial climate change. *Quaternary Science Reviews,* 22(5–7):659–671. **https://doi.org/10.1016/S0277-3791(02)00184-1**

Schrag, D.P., and DePaolo, D.J., 1993. Determination of $\delta^{18}O$ of seawater in the deep ocean during the Last Glacial Maximum. *Paleoceanography,* 8(1):1–6. **https://doi.org/10.1029/92PA02796**

Schrag, D.P., Hampt, G., and Murray, D.W., 1996. Pore fluid constraints on the temperature and oxygen isotopic composition of the glacial ocean. *Science,* 272(5270):1930–1932. **https://doi.org/10.1126/science.272.5270.1930**

Seki, O., Foster, G.L., Schmidt., D.N., Mackensen, A., Kawamura, K., and Pancost, R.D., 2010. Alkenone and boron-based Pliocene pCO_2 records. *Earth and Planetary Science Letters,* 292(1–2):201–211. **https://doi.org/10.1016/j.epsl.2010.01.037**

Shipboard Scientific Party, 1971. Site 62. *In* Winterer, E.L., et al., *Initial Reports of the Deep Sea Drilling Project*, 7: Washington, DC (U.S. Government Printing Office), 49–322. **https://doi.org/10.2973/dsdp.proc.7.104.1971**

Stagg, H.M.J., and Exon, N.F., 1981. Geology of the Scott Plateau and Rowley Terrace, off northwestern Australia. *Bureau of Mineral Resources, Geology and Geophysics Bulletin,* 213. **http://www.ga.gov.au/corporate_data/62/Bull_213.pdf**

Steinberg, C.R., Choukroun, S.M., Slivkoff, M.M., Mahoney, M.V., and Brinkman, R.M., 2006. Currents in the Bismarck Sea and Kimbe Bay, Papua New Guinea. *TNC Pacific Island Countries Report,* 6/06. **http://www.conservationgateway.org/Files/Pages/currents-bismarck-sea-and.aspx**

Steph, S., Tiedemann, R., Prange, M., Groeneveld, J., Schulz, M., Timmermann, A., Nürnberg, D., Rühlemann, C., Saukel, C., and Haug, G.H., 2010. Early Pliocene increase in thermohaline overturning: a precondition for the development of the modern equatorial Pacific cold tongue. *Paleoceanography,* 25(2):PA2202. **https://doi.org/10.1029/2008PA001645**

Stott, L., Cannariato, K., Thunell, R., Haug, G.H., Koutavas, A., and Lund, S., 2004. Decline of surface temperature and salinity in the western tropical Pacific Ocean in the Holocene epoch. *Nature,* 431(7004):56–59. **https://doi.org/10.1038/nature02903**

Stott, L., Poulsen, C., Lund, S., and Thunell, R., 2002. Super ENSO and global climate oscillations at millennial time scales. *Science,* 297(5579):222–226. **https://doi.org/10.1126/science.1071627**

Susanto, R.D., and Gordon, A.L., 2005. Velocity and transport of the Makassar Strait throughflow. *Journal of Geophysical Research: Oceans,* 110(C1):C01005. **https://doi.org/10.1029/2004JC002425**

Symonds, P.A., Collins, C.D.N., and Bradshaw, J., 1994. Deep structure of the Browse Basin: implications for basin development and petroleum exploration. *In* Purcell, P.G., and Purcell, R.R. (Eds.), *The Sedimentary Basins of Western Australia: Proceedings of the West Australian Basins Symposium:* Perth, Australia (Petroleum Exploration Society of Australia), 315–331.

Tachikawa, K., Cartapanis, O., Vidal, L., Beaufort, L., Barlyaeva, T., and Bard, E., 2011. The precession phase of hydrological variability in the Western Pacific Warm Pool during the past 400 ka. *Quaternary Science Reviews,* 30(25–26):3716–3727. **https://doi.org/10.1016/j.quascirev.2011.09.016**

Tachikawa, K., Timmermann, A., Vidal, L., Sonzogni, C., and Timm, O.E., 2013. Southern Hemisphere orbital forcing and its effects on CO_2 and tropical Pacific climate. *Climate of the Past Discussions,* 9(2):1869–1900. **https://doi.org/10.5194/cpd-9-1869-2013**

Taylor, B., 1979. Bismarck Sea: evolution of a back-arc basin. *Geology,* 7(4):171–174. **https://doi.org/10.1130/0091-7613(1979)7<171:BSEOAB>2.0.CO;2**

Wallmann, K., Aloisi, G., Haeckel, M., Tishchenko, P., Pavlova, G., Greinert, J., Kutterolf, S., and Eisenhauer, A., 2008. Silicate weathering in anoxic marine sediments. *Geochimica et Cosmochimica Acta,* 72(12):2895–2918. **https://doi.org/10.1016/j.gca.2008.03.026**

Wang, H., and Mehta, V.M., 2008. Decadal variability of the Indo-Pacific Warm Pool and its association with atmospheric and oceanic variability in the NCEP–NCAR and SODA reanalyses. *Journal of Climate,* 21(21):5545–5565. **https://doi.org/10.1175/2008JCLI2049.1**

Wara, M.W., Ravelo, A.C., and Delaney, M.L., 2005. Permanent El Niño-like conditions during the Pliocene warm period. *Science,* 309(5735):758–761. **https://doi.org/10.1126/science.1112596**

Wilkens, R.H., Westerhold, T., Drury, A.J., Lyle, M., Gorgas, T., and Tian, J., 2017. Revisiting the Ceara Rise, equatorial Atlantic Ocean: isotope stratigraphy of ODP Leg 154. *Climate of the Past,* 13:779–793. **https://doi.org/10.5194/cp-13-779-2017**

Woodard, S.C., Rosenthal, Y., Miller, K.G., Wright, J.D., Chiu, B.K., and Lawrence, K.T., 2014. Antarctic role in Northern Hemisphere glaciation. *Science,* 346(6211):847–851. **https://doi.org/10.1126/science.1255586**

Xu, J., Holbourn, A., Kuhnt, W., Jian, Z., and Kawamura, H., 2008. Changes in the thermocline structure of the Indonesian outflow during Terminations I and II. *Earth and Planetary Science Letters,* 273(1–2):152–162. **https://doi.org/10.1016/j.epsl.2008.06.029**

Zachos, J., Pagani, M., Sloan, L., Thomas, E., and Billups, K., 2001. Trends, rhythms, and aberrations in global climate 65 Ma to present. *Science,* 292(5517):686–693. **https://doi.org/10.1126/science.1059412**

Zhang, Y.G., Pagani, M., and Liu, Z., 2014. A 12-million-year temperature history of the tropical Pacific Ocean. *Science,* 344(6179):84–87. **https://doi.org/10.1126/science.1246172**

Zhang, Y.G., Pagani, M., Liu, Z., Bohaty, S.M., and DeConto, R., 2013. A 40-million-year history of atmospheric CO_2. *Philosophical Transactions of the Royal Society, A: Mathematical, Physical & Engineering Sciences,* 371(2001):1–20. **https://doi.org/10.1098/rsta.2013.0096**

Zuraida, R., Holbourn, A., Nürnberg, D., Kuhnt, W., Dürkop, A., and Erichsen, A., 2009. Evidence for Indonesian Throughflow slowdown during Heinrich Events 3–5. *Paleoceanography,* 24(2):PA2205. **https://doi.org/10.1029/2008PA001653**